TECHNISCHE UNIVERSITÄT MÜNCHEN

Friedrich-Schiedel Institut für Neurowissenschaften

Sensory information processing in the mouse cortex: From brain circuits to single synapses

Xiaowei Chen

Vollständiger Abdruck der von der Fakultät für Medizin der Technischen Universität München zur Erlangung des akademischen Grades eines

Doctor of Philosophy (Ph.D.)

genehmigten Dissertation.

Vorsitzende: Priv.-Doz. Dr. Jana E. Hartmann

Prüfer der Dissertation:

1. Univ.-Prof. Dr. Arthur Konnerth

2. apl. Prof. Dr. Helmuth K. H. Adelsberger

Die Dissertation wurde am 21.09.2011 bei der Fakultät für Medizin der Technischen Universität München eingereicht und durch die Fakultät für Medizin am 19.10.2011 angenommen.

Table of Contents

Introduction

How do human beings and animals make sense of the world? The central way is that a sensory system, consisting of peripheral sensory receptors, neural pathways, and sensory parts of central nervous system, is involved in sensing, processing and coding the sensory stimuli from the environment. There are a multitude of senses in mammals, such as vision, hearing, somatic sensation, and olfaction and so on, which have been shown to require different pathways from the periphery to the brain.

In the mammalian brain, the cerebral cortex, located in the outer layer of cerebrum, contains specific areas being considered as higher terminals that receive and process sensory information. These specific cortical areas are called sensory areas. In general, different sensory modalities, including vision, audition, and touch, are served by different cortices—visual cortex, auditory cortex, and somatosensory cortex respectively. For instance, in the whisker sensory information system, a well-established system for studying sensory neurophysiology in rodents, the barrel cortex (the somatosensory cortex) receives sensory information from whisker follicles through afferent pathways converging onto thalamus (see Fig. 1, light blue, and Fig. 2) [1,2]. In addition to the cerebral cortex, the cerebellar cortex, a separate structure attached to the posterior part of the brain in mice and rats, also receives rich sensory inputs and probably integrates these inputs for the fine tuning of motor control or for providing information for motor learning [3,4]. This can be also clearly seen with the example of whisker sensory system, in which sensory information reaches to the cerebellar cortex through a trigeminal nuclei—pontine nuclei pathway (see Fig. 1, deep blue, and Fig. 2) [5-7].

One fundamental challenge for understanding the basic principles of sensory information processing in the mammalian brain is to dissect neural circuits required for information signal flow. Investigation of this issue requires systematic characterization of the participating cell types, their connections, and their activity during sensory processing [8]. In addition, how the neurons in the sensory system organize synaptic inputs, especially at the input-receiving side—dendrites, is another basic question that has fascinated sensory neurophysiologists for decades.

These two issues have been staying with me throughout the whole period of my study. To attempt to work them out, I mainly focused on the investigation of two sensory systems, the cerebellar cortex and the primary sensory cortex in the living mouse brain, by using multiple experimental methods, including *in vivo* electrophysiology, two-photon calcium imaging, local pharmacological manipulations, and behavioural tests. With the help of other members in the lab, several lines findings from these systems were obtained. Based on these findings and some previously-established anatomical and physiological knowledge, we have achieved a number of full pictures for better understanding the basic principles sensory processing in the mammalian brain. In addition, we have made some improvements and developments of techniques in electrophysiology, two-photon calcium imaging, and acute pharmacological treatment. These allowed us and other researchers to perform functional studies in neural circuitry of the living mouse brain within the range of macro- to micro-scale.

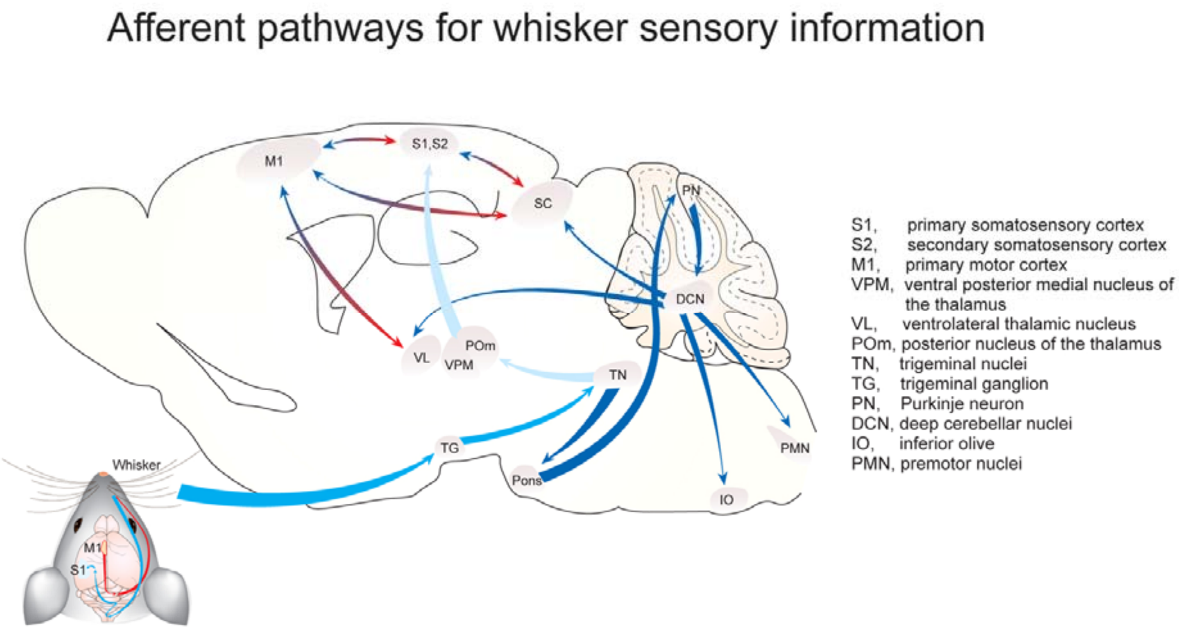

Figure 1. Afferent pathways for whisker sensory information to the cerebral cortex and to the cerebellar cortex in rodents.

Light blue arrows show the pathway to the cerebral cortex, somatosensory cortex, and deep blue arrows show the one to the cerebellar cortex. In addition, red arrows show the projections to motor system (modified from references [5-7]).

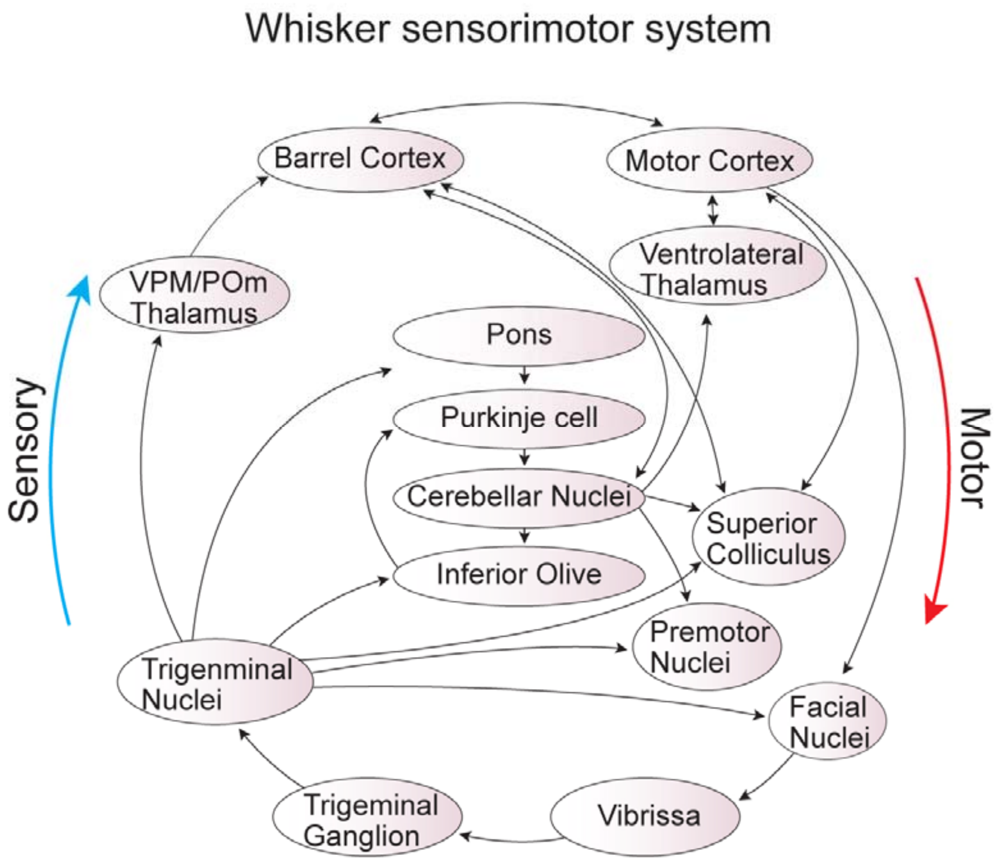

Figure 2. Whisker sensorimotor system in rodents.

Blue arrows show the sensory pathway, and red arrows show the projections to motor system (modified from references [5-7]).

In the following sections, I will describe in details the projects on these two issues by working on different sensory areas: 1) Dissection of cerebellar cortical circuits underlying whisker sensory information processing. Prior to this part, as a practice stage for my study, I also performed a series of experiments to understand one functional circuit in the cerebellum, namely the olivo-cerebellar circuit, and the role of this circuit in motor behaviour. Although I did not directly study the sensory processing in this part, I benefited a lot from this stage for the following projects: first, this was a transition phase for me to enter *in vivo* neurophysiological research field, since at earlier stage of my neuroscience study I mainly worked on *in vitro* preparations; second, I learned *in vivo* two-photon imaging-based electrophysiological and calcium measurements, which served as the major techniques for the studies; finally, I established a concept how neural signal flow in the brain circuits. Therefore, I will begin with this project as the first part: "Disruption of the olivo-cerebellar circuit by Purkinje neuron-specific ablation of BK channels"[9], followed by the second project

"Basket cell-mediated regulation of sensory-evoked signalling in the cerebellar cortical circuitry *in vivo*".

2) Understanding of the organization of sensory inputs at both dendrite level and spine level. This was carried out in two sensory cortical areas, the primary visual cortex [10] and the primary auditory cortex [11], respectively. For the dendrite part, we studied visual response by a moving grating in the primary visual cortex. In the end, we obtained a map of dendritic organization of visual inputs to cortical neurons, and described partially the rules of how dendritic tree integrates visual information in cortical neurons [10]. In this part, my contribution was to establish the whole-cell patch-clamp recording technique and local pharmacological manipulation in anesthetized mice, and trained others to use these techniques for further observations [12]. About 30% of he experimental data shown in the published paper [10] were obtained with my contribution. This part will be presented separately in two sections: 1) for biological finding, the title will be "Dendritic organization of sensory input to cortical neurons *in vivo*" [10]; 2) for technical details, the title will be "In vivo two-photon imaging of sensory-evoked dendritic calcium signals in cortical neurons" [12].

Subsequently, my major focus for the organization of sensory inputs was to establish functional imaging of single spines *in vivo*, and to understand how sensory information is processed at single synapse level. For this part, we used the primary auditory cortex as an experimental system, and for the first time we explored the sound tuning properties of single synapses. This will be the project titled "Functional mapping of single spines in cortical neurons *in vivo*".

References

1 Brecht, M. Barrel cortex and whisker-mediated behaviors. *Curr Opin Neurobiol* **17**, 408-416 (2007).

2 Petersen, C. C. The functional organization of the barrel cortex. *Neuron* **56**, 339-355 (2007).

3 Apps, R. & Garwicz, M. Anatomical and physiological foundations of cerebellar information processing. *Nat Rev Neurosci* **6**, 297-311 (2005).

4 Ito, M. *The cerebellum and neural control*. (Raven Press, 1984).

5 Diamond, M. E., von Heimendahl, M., Knutsen, P. M., Kleinfeld, D. & Ahissar, E. 'Where' and 'what' in the whisker sensorimotor system. *Nat Rev Neurosci* **9**, 601-612 (2008).

6 Kleinfeld, D., Berg, R. W. & O'Connor, S. M. Anatomical loops and their electrical dynamics in relation to whisking by rat. *Somatosens Mot Res* **16**, 69-88 (1999).

7 Yoshihara, Y. Visualizing selective neural pathways with WGA transgene: combination of neuroanatomy with gene technology. *Neurosci Res* **44**, 133-140 (2002).

8 Luo, L., Callaway, E. M. & Svoboda, K. Genetic dissection of neural circuits. *Neuron* **57**, 634-660 (2008).

9 Chen, X. *et al.* Disruption of the olivo-cerebellar circuit by Purkinje neuron-specific ablation of BK channels. *Proc Natl Acad Sci U S A* **107**, 12323-12328 (2010).

10 Jia, H., Rochefort, N. L., Chen, X. & Konnerth, A. Dendritic organization of sensory input to cortical neurons in vivo. *Nature* **464**, 1307-1312 (2010).

11 Chen, X., Leischner, U., Rochefort, N. L., Nelken, I. & Konnerth, A. Functional mapping of single spines in cortical neurons in vivo. *Nature* (2011).

12 Jia, H., Rochefort, N. L., Chen, X. & Konnerth, A. In vivo two-photon imaging of sensory-evoked dendritic calcium signals in cortical neurons. *Nat Protoc* **6**, 28-35 (2011).

Project I

Disruption of the olivo-cerebellar circuit by Purkinje neuron-specific ablation of BK channels

(Published in **PNAS**, 2010, 107: 12323-8)

Disruption of the olivo-cerebellar circuit by Purkinje neuron-specific ablation of BK channels

Xiaowei Chen[a,1], Yury Kovalchuk[a,1], Helmuth Adelsberger[a], Horst A. Henning[a], Matthias Sausbier[b], Georg Wietzorrek[c], Peter Ruth[b], Yosef Yarom[d], and Arthur Konnerth[a,2]

[a]Center for Integrated Protein Science and Institute of Neuroscience, Technical University Munich, 80802 Munich, Germany; [b]Department of Pharmacology and Toxicology, University of Tübingen, D-72076 Tübingen, Germany; [c]Molecular and Clinical Pharmacology, Innsbruck Medical University, 6020 Innsbruck, Austria; and [d]Department of Neurobiology, Life Science Institute and the Interdisciplinary Center for Neural Computation, Hebrew University, Jerusalem 91904, Israel

Edited* by Rodolfo R. Llinas, New York University Medical Center, New York, NY, and approved April 22, 2010 (received for review February 11, 2010)

The large-conductance voltage- and calcium-activated potassium (BK) channels are ubiquitously expressed in the brain and play an important role in the regulation of neuronal excitation. Previous work has shown that the total deletion of these channels causes an impaired motor behavior, consistent with a cerebellar dysfunction. Cellular analyses showed that a decrease in spike firing rate occurred in at least two types of cerebellar neurons, namely in Purkinje neurons (PNs) and in Golgi cells. To determine the relative role of PNs, we developed a cell-selective mouse mutant, which lacked functional BK channels exclusively in PNs. The behavioral analysis of these mice revealed clear symptoms of ataxia, indicating that the BK channels of PNs are of major importance for normal motor coordination. By using combined two-photon imaging and patch-clamp recordings in these mutant mice, we observed a unique type of synaptic dysfunction in vivo, namely a severe silencing of the climbing fiber–evoked complex spike activity. By performing targeted pharmacological manipulations combined with simultaneous patch-clamp recordings in PNs, we obtained direct evidence that this silencing of climbing fiber activity is due to a malfunction of the tripartite olivo-cerebellar feedback loop, consisting of the inhibitory synaptic connection of PNs to the deep cerebellar nuclei (DCN), followed by a projection of inhibitory DCN afferents to the inferior olive, the origin of climbing fibers. Taken together, our results establish an essential role of BK channels of PNs for both cerebellar motor coordination and feedback regulation in the olivo-cerebellar loop.

cerebellar ataxia | climbing fiber | complex spike | two-photon imaging

The large-conductance voltage- and Ca^{2+}-activated K^{+} (BK) channels, which modulate action potential firing by regulating the fast afterhyperpolarization (1), are highly expressed in cerebellar Purkinje neurons (PNs) (2, 3). Several in vitro studies demonstrated that BK channels in the somata and dendrites of PNs are activated by action potentials and, in turn, regulate the firing rate and firing pattern of these neurons (4–10). Furthermore, mice lacking BK channels exhibit clear symptoms of cerebellar ataxia (2), indicating a critical role of BK channels in motor control. On the cellular level, this total deletion of BK channels results in a marked reduction in action potential activity of PNs, which was suggested to be mediated by depolarization-induced inactivation of Na^{+} channels (2). It should be noted, however, that not only PNs but also other cerebellar neurons, like Golgi cells, express BK channels and exhibit a change in firing properties in total BK channels–deficient mice (11). Therefore, it is difficult to evaluate the relative contribution of the modified PNs to the motor deficits of mice lacking BK channels.

The reduced activity of inhibitory PNs and the resultant hyperexcitability of their targets, the deep cerebellar nuclei (DCN), are considered to be important features of cerebellar ataxia (12, 13), but their impact on downstream brain circuits is largely unknown. It has been suggested that the olivo-cerebellar circuit, one of the major neuronal circuits for motor control in the brain, provides timing signals for motor coordination (14–16). This circuit is a loop of interconnected structures where the cerebellar cortex innervates the inferior olivary nucleus (IO) via the DCN, and the olivary neurons via the climbing fibers are fed back into the cerebellar cortex. Whereas the olivary neurons exert an excitatory action on the PN at the cerebellar cortex, both the PN and DCN terminals exert an inhibitory action on their target cells (17–19). Thus, it is likely that this long-range feedback loop will be affected by the alteration in PN's activity observed in the BK$^{-/-}$ mouse. For these reasons, the aims of the present study were to assess the specific role of BK channels of PNs for motor coordination and downstream circuit function in vivo.

Results and Discussion

BK Channels of Purkinje Neurons Are Essential for Motor Coordination. To explore the specific contribution of BK channels of PNs for motor behavior, we generated a mouse line lacking BK channels exclusively in PNs, which we refer to as PN-BK$^{-/-}$ (for details see *SI Materials and Methods*). The BK channel α-subunit in PNs was specifically ablated in mice by intercrossed constitutive heterozygous BK L1/+ mice (SV129 background) with transgenic mice expressing the Cre recombinase under the control of the Purkinje protein 2 gene (20). The resulting genotype was analyzed by PCR amplification and confirmed by immunohistochemistry as described previously (Fig. S1) (2, 20). Next we examined motor behavior in total BK$^{-/-}$ mice and in PN-BK$^{-/-}$ mice and compared it with that of WT mice. Consistent with a previous study (2), we observed a pronounced deficiency in motor coordination in total BK$^{-/-}$ mice by footprint analysis ($n = 4$ WT and 4 total BK$^{-/-}$ mice; $P < 0.05$) and by the increased number of slips of the hind limbs during either ladder runway ($n = 7$ WT and 4 total BK$^{-/-}$ mice; $P < 0.05$) or balance beam tests ($n = 6$ WT and 5 total BK$^{-/-}$ mice; in balance beam tests, total BK$^{-/-}$ mice were unable to move forward on the beam) (Fig. 1 *A* and *B*). In the same behavioral tests, PN-BK$^{-/-}$ mice also exhibited clear deficits in their walking behavior (total numbers of animals were 12 WT mice and 11 PN-BK$^{-/-}$ mice; $P < 0.05$ for each test) (Fig. 1 *C* and *D*). Remarkably, the behavioral deficits in PN-BK$^{-/-}$ mice were similar to those seen in the total BK$^{-/-}$ mice, albeit the severity of the symptoms was slightly reduced. These observations provide unambiguous support for the specific involvement of PN's BK channels in cerebellar motor control.

On the cellular level, previous experiments from brain slice recordings demonstrated a pronounced reduction in simple spike (SS) activity of PNs in BK$^{-/-}$ mice (2). Remarkably, many PNs of BK$^{-/-}$ mice had strongly depolarized resting membrane potentials, some exhibiting even a total depolarization blockade

---

Author contributions: Y.Y. and A.K. designed research; X.C., Y.K., H.A., H.A.H., M.S., G.W., P.R., and Y.Y. performed research; A.K. contributed new reagents/analytic tools; X.C., H.A., H.A.H., M.S., P.R., and A.K. analyzed data; and X.C., Y.Y., and A.K. wrote the paper.

The authors declare no conflict of interest.

*This Direct Submission article had a prearranged editor.

[1]X.C. and Y.K. contributed equally to this work.

[2]To whom correspondence should be addressed. E-mail: arthur.konnerth@lrz.tu-muenchen.de.

This article contains supporting information online at www.pnas.org/lookup/suppl/doi:10.1073/pnas.1001745107/-/DCSupplemental.

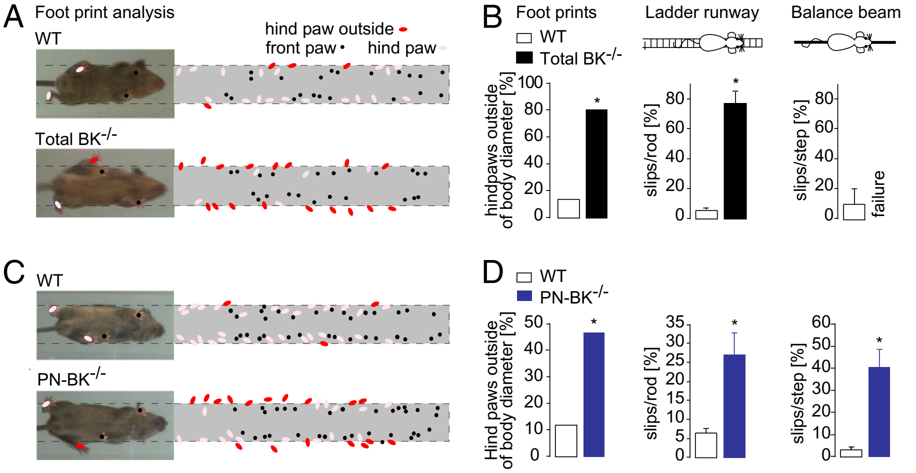

Fig. 1. Impairments of motor coordination in both total BK$^{-/-}$ and PN-BK$^{-/-}$ mice. (*A*) Footprint patterns in WT and total BK$^{-/-}$ mice. *Left:* Mice walking on a glass plate. Their body diameters are indicated by dotted lines. *Right:* Summary of the superimposed paw positions of four WT and four total BK$^{-/-}$ mice. (*B*) Bar chart comparison of walking behavior in WT and total BK$^{-/-}$ mice. *Left:* Summary of *A* showing the percentage of hindpaw positions outside of the body diameter. *Center:* Percentage of hindpaw slips relative to the total number of steps on a ladder (n = 7 WT and 4 total BK$^{-/-}$ mice). *Right:* Percentage of hindpaw slips during running on a balance beam (n = 6 WT and 5 total BK$^{-/-}$ mice). (*C*) Footprint patterns in WT and PN-BK$^{-/-}$ mice. *Right:* Summary of the paw positions of 7 WT and PN-BK$^{-/-}$ mice. (*D*) Histograms indicate the percentage of hindpaw positions outside of the body diameter (*Left:* summary of the number of red dots in *C*), the percentage of hindpaw slips relative to the total number of steps on a ladder runway (*Center*) (n = 12 WT and 11 PN-BK$^{-/-}$ mice), and the percentage of hindpaw slips during running on a balance beam (*Right*) (n = 9 WT and 9 PN-BK$^{-/-}$ mice). Failure means in this case that the animals are not able to move forward on the beam but fall down. *P < 0.05. Error bars show SEM.

(2, 11). These observations indicated that the cause for the reduction in SS activity is a partial inactivation of Na$^+$ channels, because of this excessive depolarization. To determine the SS firing rate in PN-BK$^{-/-}$ mice in vivo, we performed cell-attached patch-clamp recordings in fluorescently labeled PNs using the two-photon imaging-based "shadow patch" approach (21) under isoflurane anesthesia (Fig. S2*A*). The spontaneous activity in vivo consisted of two types of responses: the characteristic SSs, which reflect an interplay between afferent synaptic activity (22, 23) and intrinsic properties of PNs (24, 25); and the complex spikes (CSs) (26), which are generated by the activity of the climbing fibers (Fig. S2*B*). As in the previous studies (2), we observed a substantial decrease in SS frequency in PN-BK$^{-/-}$ mice, albeit to a lesser degree (Fig. S2 *C* and *D*). The mean frequency of SS for all cells was 1.2-fold higher in WT cells (67.0 ± 10.3 Hz; n = 34 cells and 10 mice) than in PN-BK$^{-/-}$ mice (55.6 ± 1.0 Hz; n = 57 cells and 10 mice; $P < 0.05$; Table S1), and approximately 2.7-fold higher than in total BK$^{-/-}$ mice (24.7 ± 3.5 Hz; n = 30 cells and 5 mice; $P < 0.01$). We conclude that PN-BK$^{-/-}$ mice are ataxic and display a reduction in SS activity. The results are in general agreement with the original suggestion that a "depolarization block" may underlie the reduced SS firing frequency (2). Together, our observations strongly support the role of PN's BK channels in motor coordination. However, comparison of the changes in total BK$^{-/-}$ mice with those in PN-BK$^{-/-}$ mice shows that the latter exhibit a lesser degree of severity. This implies that the motor impairment in total BK$^{-/-}$ mice is probably caused by the deletion of BK channels in both PNs and other cell types (e.g., Golgi cells) (11).

Severe Silencing of Climbing Fiber–Evoked CS in PN-BK$^{-/-}$ Mice in Vivo. The striking finding was a significant reduction up to complete elimination of CS activity in a large fraction of PNs (Fig. 2). Under our recording conditions, the climbing fiber–mediated CS activity could be unambiguously distinguished from the SS activity: first by the waveform of the electrical responses recorded in the cell-attached configuration (Fig. S2*B*, *Insets*), and second by the well-established fact that CSs, but not SSs, are associated with global dendritic Ca^{2+} transients (27) (Fig. 2*A*). For comparison of the changes in frequency of CS activity in the two genotypes, PNs were assigned to three frequency classes that were categorized as "normal" (>0.6 Hz), "quiet" (0.05–0.6 Hz) or "silent" (0–0.05 Hz) (Fig. 2 *A*–*C*). Unexpectedly, we found that the CS activity in PN-BK$^{-/-}$ mice was severely reduced, with a dramatic increase of silent PNs from virtually none in WT to 46% in PN-BK$^{-/-}$ mice and an increase of the quiet PNs from 5% to 23%. Silent, quiet, and normal PNs were randomly distributed within all regions of the cerebellar vermis. In line with these observations, the proportion of normal PNs dropped from 95% in WT to 31% in PN-BK$^{-/-}$ mice (n = 34 WT cells and 57 PN-BK$^{-/-}$ cells) (Fig. 2*C*). The significant decrease in CS activity was also seen in average firing rates for the quiet and normal categories, which were reduced from 0.45 ± 0.08 Hz in WT (n = 2 quiet cells out of a total of 34 cells) to 0.15 ± 0.03 Hz in PN-BK$^{-/-}$ mice (n = 13/57 quiet cells; $P < 0.05$) and from 1.45 ± 0.06 Hz in WT (n = 32 of 34 normal cells) to 1.07 ± 0.08 Hz in PN-BK$^{-/-}$ mice (n = 18 of 57 normal cells; $P < 0.01$; Table S1).

What are the mechanisms that might underlie the impaired CS activity? We first considered the possibility of breakdown of climbing fiber–PN synapses. Such a hypothetical breakdown may result from excessive release of endocannabinoids (28) in PN-BK$^{-/-}$ mice, due to depolarization of BK-deficient PNs (2). To test this possibility, we performed whole-cell recordings of climbing fiber–evoked responses in PNs of cerebellar slices using conventional stimulation procedures (29) (Fig. 2*D*). In agreement with a previous work indicating a rather modest role of BK channels in shaping the CS waveform (30), we noticed in PNs of PN-BK$^{-/-}$ mice a slight increase in the number of spikelets as compared with WT mice (mean number of spikelets = 3.3 ± 0.1 for WT cells and 4.1 ± 0.1 for PN-BK$^{-/-}$ cells; n = 5 cells for each genotype; $P < 0.001$) (Fig. S3 *A* and *B*). We also found that the climbing fiber–evoked dendritic Ca^{2+} transients had a larger amplitude and a slower time course in PN-BK$^{-/-}$ (Fig. S3 *C* and *D*). This increase in dendritic Ca^{2+} signal is consistent with a previous study reporting an increase in Ca^{2+} entry per action potential in the presence of a pharmacological blocker of BK channels (4). It is important to note that CSs could be elicited with the same high degree of reliability in both genotypes (5 of 5 cells in WT and 10 of 10 cells in PN-BK$^{-/-}$ mice) (Fig. 2*E*). We also tested the possibility that the synaptic failures in PN-BK$^{-/-}$ mice may occur only at higher frequencies of climbing fiber activity, as encountered under in vivo conditions. However, even prolonged climbing fiber stimulation at 1 Hz had no deleterious effect on CS activity in PN-BK$^{-/-}$ mice (Fig. S4). Together, these results indicate that the basic properties of climbing fiber–PN synapses were unaltered by the removal of BK channels in PN-BK$^{-/-}$ mice.

Disruption of the Olivo-Cerebellar Circuit in PN-BK$^{-/-}$ Mice. We next investigated whether the reduction in the frequency of CS activity could be due to malfunction of the olivo-cerebellar circuit. First we examined the integrity of the olivo-cerebellar connection by applying harmaline, a tremorgenic drug known to exert a rather specific action on the olivary nucleus (31) (Fig. 3*A*). The lack of harmaline action on CS activity through a direct effect on PNs was confirmed in control experiments, in which local application of harmaline to the recorded PNs did not significantly

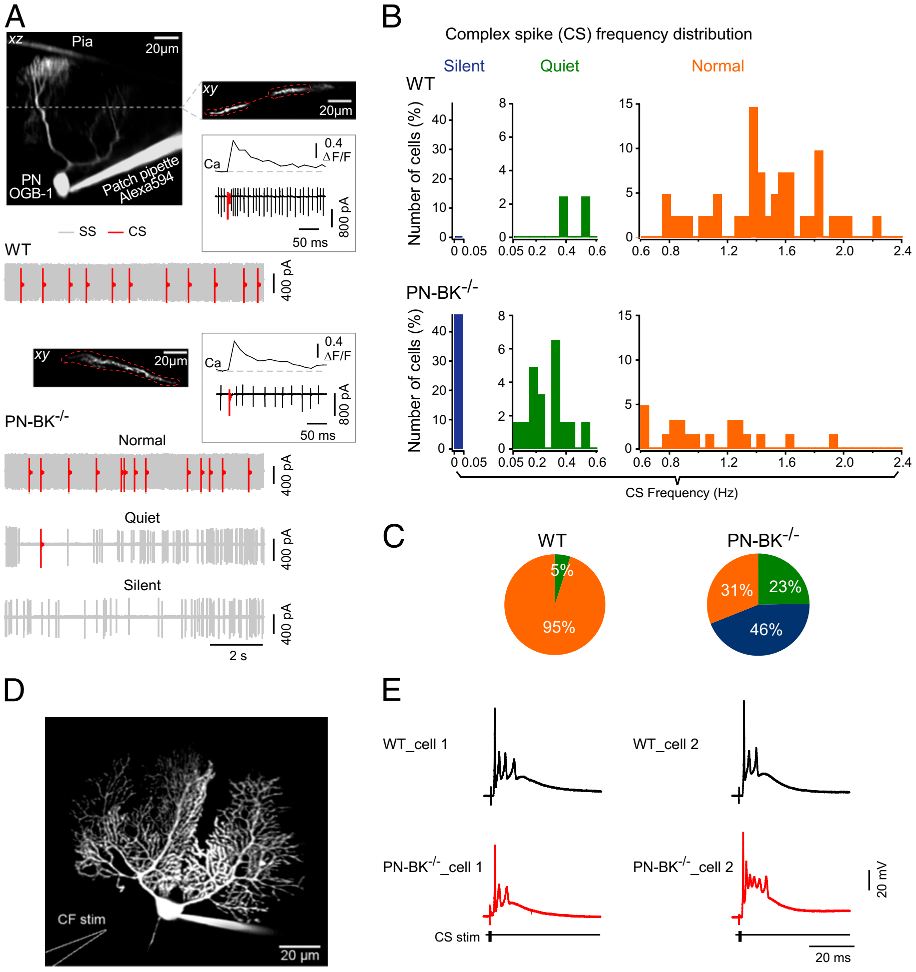

Fig. 2. Silencing of CS activity in PN-BK$^{-/-}$ mice. (*A*) Cell-attached recording and Ca^{2+} imaging of CS activity. Projection images: an electroporated PN filled with Oregon Green BAPTA-1 (OGB-1) from a WT (upper two images) or PN-BK$^{-/-}$ (lower image) mouse. The *xy* image (*Upper Right*) is an optical section through the dendritic tree of the PN at the level marked by the dotted line in the *xz* image (*Upper Left*). Regions of interest are delineated by dotted red lines. *Insets:* Examples of individual CSs and the corresponding Ca^{2+} transients from a WT (*Upper*) or PN-BK$^{-/-}$ (*Lower*) cell. Electrical traces: one example of PN activity in a WT cell and three examples in PN-BK$^{-/-}$ cells. The latter represents the three classes of CS activity: silent (0–0.05 Hz), quiet (0.05–0.6 Hz), and normal (0.6–2.4 Hz). The SS and CS are labeled in gray and red, respectively. The continuous gray background reflects high frequency of SS activity. (*B*) Frequency distribution in the three classes of cells. (*C*) Pie charts summarize the relative proportion of PNs with silent, quiet, or normal climbing fiber activity (n = 34 WT cells and 57 PN-BK$^{-/-}$ cells; 10 mice for each genotype). (*D*) Image of a whole-cell patch-clamped PN and the location of the climbing fiber stimulation pipette (CF stim) in a cerebellar slice preparation. (*E*) Representative traces from two cells of each genotype, showing the characteristic CS waveforms elicited by stimulating the climbing fibers. Note the similarity of the responses (n = 5 WT and 10 PN-BK$^{-/-}$ cells).

change the frequency of CSs ($n = 4$ cells; $P > 0.05$) (Fig. S5). In the experiment illustrated in Fig. 3*B*, four neighboring PNs of a PN-BK$^{-/-}$ mouse were identified by electroporating them with a fluorescent marker dye. After that, the spiking activity was monitored by sequentially performing cell-attached recordings from each of these PNs. Under control conditions we found that PN2 was silent, that PN1 and PN3 were quiet, and that PN4 was normal (Fig. 3*C*, *Left*). Next, we injected harmaline i.p. Twenty minutes after harmaline injection we performed another round of cell-attached recordings from each of the labeled PN. We found that in all PNs, irrespective of their control status, the CS activity was rescued (Fig. 3*C*). In fact, across the population, the firing frequency of CS in PN-BK$^{-/-}$ mice after harmaline treatment was indistinguishable from that recorded in WT mice (mean CS frequency, 4.0 ± 0.2 Hz for WT and 4.1 ± 0.3 Hz for PN-BK$^{-/-}$; $P > 0.05$; Table S1) (Fig. 3*D*). Next, we examined harmaline-induced tremor (31) in both genotypes. Because this assay requires a normal function of the connection between the IO and the PNs, it serves as a powerful test for the olivo-cerebellar circuit in behaving mice. We found that, as for the harmaline-mediated induction of CS activity in PNs, the tremor behavior was also induced to similar levels in WT and PN-BK$^{-/-}$ mice ($n = 7$ mice for each genotype; $P > 0.05$) (Fig. 3 *E* and *F*). Thus, our results show that the deletion of BK channels in PNs leads to a massive reduction in the activity of IO neurons, which most likely results from malfunction of the olivo-cerebellar circuit.

To test the role of PN-mediated inhibitory synaptic transmission in the DCN for CS silencing, we designed an in vivo experiment in which we performed cell-attached recordings from PNs while applying GABA$_A$ receptor antagonist (gabazine) or agonist (muscimol) locally to the DCN (Fig. 4 *A* and *B*). The accuracy and the specificity of the drug applications were carefully assessed by coinjecting an inert fluorescent marker dye (Alexa594). The control experiments included the post hoc anatomical verification of the application site (Fig. 4*C*) and the electrophysiological monitoring of the DCN-characteristic neuronal activity through the dye application pipette (Figs. S6 and S7) (see *SI Materials and Methods* for further details). Consistent with the reduced efficacy of the inhibitory synapse between the PN and the DCN neurons in BK$^{-/-}$ mice (2), we observed an increase in firing frequency of DCN neurons in PN-BK$^{-/-}$ mice in vivo. The mean firing frequencies of DCN neurons were 10.5 ± 2.3 Hz in WT mice ($n = 16$ cells) and 14.7 ± 1.9 Hz in PN-BK$^{-/-}$ mice ($n = 14$ cells; $P < 0.05$) (Fig. S7). We next applied gabazine to the DCN in WT mice. We found that gabazine application reversibly blocked CS activity (Fig. 4*D*). Additionally, in the other seven PNs tested, gabazine applied to the DCN markedly decreased the CS activity (mean frequency, 1.6 ± 0.1 Hz for control and 0.4 ± 0.2 Hz for gabazine; $n = 8$ cells; $P < 0.001$; Fig. 4*G*, *Left* and Table S1). This result is reminiscent of earlier findings showing that various manipulations, including local disinhibition in the PN layer, lesions of the DCN, or block of inhibition in the IO, produce an increased frequency of CS activity (32, 33). Together, these results provide strong evidence in support of the hypothesis that PN-mediated inhibition forms one part of the olivo-cerebellar feedback circuit and that climbing fiber activity can be tightly controlled by the inhibitory action from PNs to the DCN. In contrast to gabazine, the GABA$_A$ receptor agonist muscimol had no detectable effect in WT mice (mean frequency, 1.6 ± 0.1 Hz for control and 1.6 ± 0.2 Hz for muscimol; $n = 11$ cells; $P > 0.05$; Fig. 4*G*, *Right* and Table S1), indicating that under our experimental conditions DCN neurons are nearly

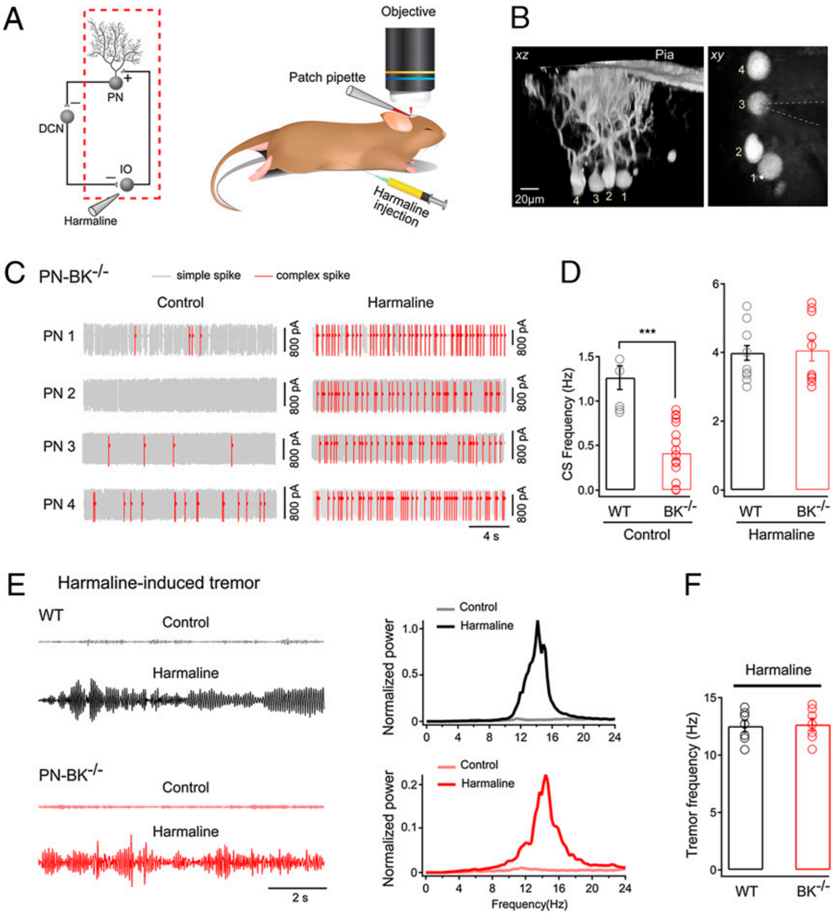

Fig. 3. Rescue of CS activity in PN-BK$^{-/-}$ mice by harmaline. (*A*) Schematic presentation of the olivo-cerebellar circuit (*Left*) and the segment under examination (red dotted square) when harmaline was i.p. injected (*Right*). (*B*) *xz* and *xy* projection images of four electroporated PNs in a PN-BK$^{-/-}$ mouse. The pipette for cell-attached recording is indicated by dotted lines. (*C*) Representative traces recorded before and after harmaline injections from the four PN-BK$^{-/-}$ cells depicted in *B*. Note that the massive increase in CS activity was observed in all PNs in response to harmaline (20 mg/kg). (*D*) Summary of the mean CS frequency from both genotypes in the absence (*Left*) or presence (*Right*) of harmaline (Control: $n = 7$ cells in WT and 18 cells in PN-BK$^{-/-}$; Harmaline: $n = 13$ cells in WT and 10 cells in PN-BK$^{-/-}$; four WT and four PN-BK$^{-/-}$ mice). In the presence of harmaline, the CS frequency in PN-BK$^{-/-}$ mice was similar to that found in WT mice. (*E*) Harmaline-induced tremor in awake, freely moving WT (black) and PN-BK$^{-/-}$ (red) mice. *Left:* Representative tremor-induced force changes recorded by a pressure sensor before and after harmaline injection. *Right:* Normalized power spectra of the force measurements. The major, single peak around 10–15 Hz represents the frequency of harmaline-induced tremor. (*F*) Comparison of the tremor frequency shows no significant difference between WT (12.5 ± 0.5 Hz; $n = 7$) and PN-BK$^{-/-}$ (12.7 ± 0.5 Hz; $n = 7$) mice. $^{***}P < 0.001$. Error bars show SEM.

maximally inhibited by PN's activity. A critical test of our hypothesis resides in the ability to restore normal CS activity by reestablishing the inhibitory action of PNs on DCN neurons. To that end we applied muscimol to the DCN in PN-BK$^{-/-}$ mice. Fig. 4*F* illustrates such an experiment, in which we recorded a "silent" PN. Application of muscimol reversibly restored a part of the CS activity. A similar rescue, or increase in CS activity, was reliably detected in all PNs tested ($n = 19$; Fig. 4*H* and Table S1). It should be noted that injecting muscimol to the DCN in PN-BK$^{-/-}$ mice is insufficient to entirely restore CS frequency, particularly in silent and quiet cells. The incomplete restoration of the CS activity may be partially due to long-term adaptive changes (e.g., some compensatory mechanisms) in the olivo-cerebellar circuit of PN-BK$^{-/-}$ mice. Alternatively, the focal application of muscimol to a fraction of DCN neurons may be insufficient for a complete restoration of the CS activity. Nevertheless, the rapid and reversible action of muscimol provides direct evidence that the olivo-cerebellar circuit function is dynamically regulated by the level of inhibition within the DCN.

In conclusion, in this study we obtained two major results. First, despite the widespread distribution of BK channels in the brain and particularly in several types of cerebellar neurons (3), we find that the BK channels of PNs are of outstanding importance for the control of motor coordination. In their absence, mice exhibit an ataxic behavior that is reminiscent of that observed in the total BK knockout mice. Second, and most importantly, we demonstrate the functional disruption of the long-range olivo-cerebellar feedback loop in this mouse model of ataxia. Because the deletion of BK channels was restricted to PNs, the malfunction must be the consequence of the altered electrical properties of PNs. Indeed, we found that in PN-BK$^{-/-}$ mice the SS activity was significantly reduced. This relatively mild effect on the SS firing stands in contrast to the robust reduction in CS activity. Moreover, the clear restoration of CS activity by emulating the inhibitory effect of PNs on DCN neurons indicates that the reduced PN-mediated inhibition in the DCN is one of the major sources of the reduced CS activity. It has been reported (2) that in BK$^{-/-}$ mice the efficacy of the inhibitory synapse between the PN and the DCN neurons is markedly reduced, particularly at frequencies higher than 10 Hz. The effective filtering of synaptic transmission at higher frequencies together with the reduced SS activity would serve to strongly attenuate the amount of GABA released from the PN terminals into the DCN. It should be mentioned that a fraction of PNs had a normal CS frequency in PN-BK$^{-/-}$ mice (31%). This indicates that in a subset of olivary neurons the activity was normal, perhaps owing to a reduced efficacy of DCN-mediated inhibition in these neurons. In addition, a minor contribution is expected to arise from the residual expression of BK channels in a small number of PNs (approximately 2–5%), as found previously when using the L7 promotor for the PN-specific deletion of proteins (20, 34). Finally, a hypothetical compensatory mechanism might also contribute to the normal CF activity in a subset of PNs.

Our results provide clear evidence that the anatomical organization of the olivo-cerebellar circuit (17–19), which comprises the cerebellar cortex, the DCN, and the IO, indeed operates as a closed loop. This suggestion is in agreement with recent results of Marshal and Lang (32), demonstrating that experimentally increasing PN firing increases the firing rate and synchrony level of CS. The functional significance of the olivo-cerebellar loop for normal motricity is indicated by the severity of the motor deficits found in our study. The ramification of these findings extends beyond the functional significance of BK channels. It, in fact, identifies a potentially important pathophysiological mechanism for several other forms of cerebellar ataxia. Different types of cerebellar ataxia are characterized by distinct molecular defects that converge into a reduced probability of action potential firing

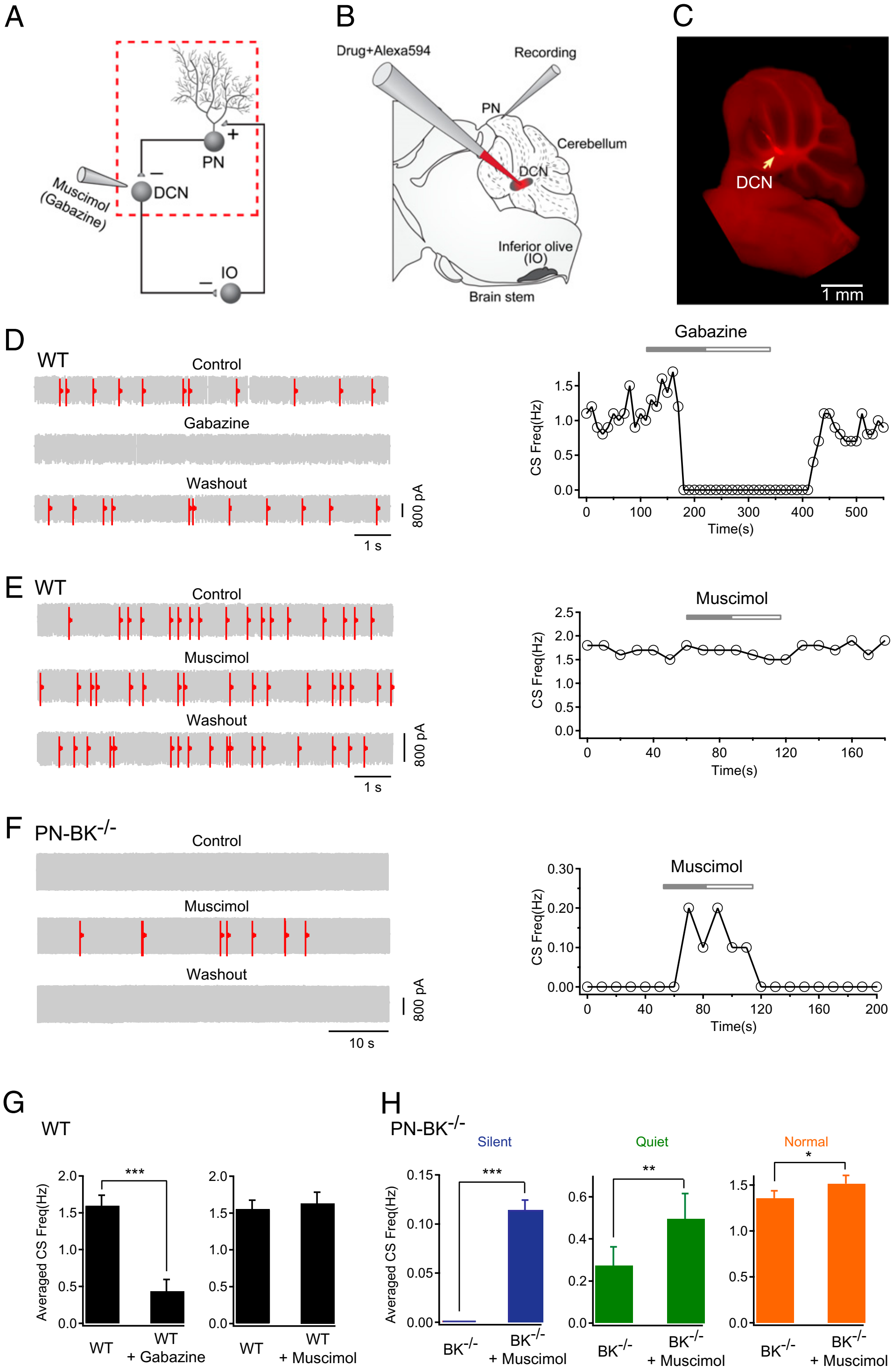

Fig. 4. Rescue of CS activity in PN-BK$^{-/-}$ mice by increasing inhibition in the DCN. (*A*) Schematic presentation of the olivo-cerebellar circuit (*Left*) and the segment under examination (red dotted square) when gabazine or muscimol was locally applied to the DCN. (*B*) Experimental configuration for cell-attached recordings from PNs and local drug applications to the DCN. The glass pipette for drug application filled with Alexa594 was lowered from cortex into the DCN. (*C*) Fluorescence image showing the site of local drug application within the DCN (arrow). (*D*) Representative electrical traces and time-course of the effect of gabazine on CS activity in a WT cell. Gabazine (200 μM) applied into DCN dramatically reduced the frequency of CS. (*E*) Representative traces and time course showing the absence of effect of muscimol (300 μM) on the CS frequency in a WT mouse. (*F*) The CS activity was restored in a silent PN-BK$^{-/-}$ cell during application of muscimol into DCN. (*G*) Summary of *D* and *E* ($n = 8$ cells for gabazine experiments, $n = 11$ cells for muscimol experiments; paired *t* tests). (*H*) Summary of the effect of muscimol on three classes of CS activity in PN-BK$^{-/-}$ mice: silent ($n = 7$ cells), quiet ($n = 7$ cells), and normal ($n = 5$ cells) (paired *t* tests). $^{*}P < 0.05$; $^{**}P < 0.01$; $^{***}P < 0.001$. Error bars show SEM.

in PNs. For example, mice lacking sodium channels Na$_v$1.6 (35) or Na$_v$1.1 (36) channels exhibit ataxia that is associated with an altered depolarizing drive and reduced action potential firing of PNs. In the episodic ataxia type 2 (37) and in the ataxic *tottering* mice (38), a P/Q calcium channel mutation not only leads to a reduced depolarizing drive and a reduced probability of BK channel activation but also to an irregular spike firing and a reduced synaptic transfer to the DCN. Mutation in potassium channels K$_v$3.3 also causes ataxia and results in a defective repolarization of action potentials accompanied by reduced firing rates in PNs (39, 40). Thus, the reduced spike firing at the PN output and the consequently reduced inhibition in the DCN represent a common cellular defect in ataxia. This defect fits with the observation that some forms of ataxia are associated with a selective increase in neuronal firing rates in the DCN (Fig. S7) (13). The present results suggest that in these forms of ataxia, the relatively increased activity of the DCN would lead to an excessive inhibition of the IO. Because this mechanism is independent of the specific etiology, the resultant silencing of CS activity is a likely common motif of these forms of ataxia and may be an important factor in this impairment of cerebellar function.

Materials and Methods

Animals. Adult mice (1–4 months old) were used in all of the experiments. All experimental procedures were performed in accordance with institutional animal welfare guidelines and were approved by the state government of Bavaria, Germany. Details of generation of PN-specific BK$^{-/-}$ mice are given in *SI Materials and Methods*.

Immunohistochemistry of Cerebellar Cortex. The procedure of immunohistochemistry was described previously (3). Additional details are given in *SI Materials and Methods*.

Motor Behavior Tests. Walking behavior tests include footprint pattern test, ladder walking test, and elevated bar balancing test. Additional details are provided in *SI Materials and Methods*.

In Vivo Electrophysiological Recordings. Surgery and in vivo electrophysiological recordings were performed as described previously (41, 42). The recordings were carried out under isoflurane anesthesia. SS and CS from extracellular recordings were sorted according to their amplitudes, shapes, and time courses using Igor Pro (Wavemetrics). Additional details are provided in *SI Materials and Methods*.

In Vitro Electrophysiological Recordings. Parasagittal cerebellar slice preparations and somatic whole-cell recordings were performed as described elsewhere (43). Climbing fiber input was stimulated by placing a patch pipette filled with Ringer solution in the granule layer (0.2 ms, 20–90-V square pulses). The location of the stimulation pipette and the stimulation intensity were adjusted until an all-or-none response was evoked.

Tremor Behavior Measurement. Harmaline-induced tremor was measured using a custom-made sensing device, which is a 13 × 10 × 14-cm plastic box with a pressure sensor (Piezo Electric Pulse Transducer; AD Instruments) underneath the center of the box. The sensor was connected to a PowerLab data acquisition system (AD Instruments), and the signal was filtered by a band pass of 0–24 Hz. Motion activity was recorded digitally and analyzed using Chart 5.0 software (AD Instruments). Each mouse was tested in the box for 10 min before and at least 30 min after i.p. injection of harmaline (20 mg/kg).

Intra-DCN Drug Application. A patch pipette filled with Alexa594 (50 μM) plus muscimol (300 μM) (Sigma) or Alexa594 plus gabazine (200 μM) was lowered from cortex (coordinates: −2.5 mm to Bregma and ±0.36 mm lateral to midline) into the DCN at an angle of 40° (Fig. 4*B*). The resistance of pipette (4–6 MΩ) and extracellular neuronal activity were monitored using an EPC9/2 amplifier with Pulse software (HEKA) during the process of pipette insertion. The location of the DCN was determined by the stereotaxic coordinates (*SI Materials and Methods*) and verified post hoc histologically (Fig. 4*C* and Fig. S6). Drugs and Alexa594 were coapplied locally by pressure injection using a Picospritzer puffer system (Picospritzer III; General Valve) connected to the injection pipette via polyethylene tubing. After completion of experiments, mice were deeply anesthetized by increasing the concentration of isoflurane above 3%, and the injection sites were marked by locally applying Alexa594. Brain slices (400 μm) were then prepared and examined using a fluorescence microscope (Fig. 4*C*).

ACKNOWLEDGMENTS. We thank Jia Lou for excellent technical assistance. This work was supported by the Deutsche Forschungsgemeinschaft (IRTG 1373, SFB 870), the European Research Area (ERA)-Net Program, and the Schiedel Foundation. A.K. is a Carl-von-Linde Senior Fellow of the Institute for Advanced Study of the Technical University Munich.

1. Faber ES, Sah P (2003) Calcium-activated potassium channels: multiple contributions to neuronal function. *Neuroscientist* 9:181–194.
2. Sausbier M, et al. (2004) Cerebellar ataxia and Purkinje cell dysfunction caused by Ca^{2+}-activated K$^+$ channel deficiency. *Proc Natl Acad Sci USA* 101:9474–9478.
3. Sausbier U, et al. (2006) Ca^{2+} -activated K$^+$ channels of the BK-type in the mouse brain. *Histochem Cell Biol* 125:725–741.
4. Womack MD, Hoang C, Khodakhah K (2009) Large conductance calcium-activated potassium channels affect both spontaneous firing and intracellular calcium concentration in cerebellar Purkinje neurons. *Neuroscience* 162:989–1000.
5. Womack MD, Khodakhah K (2003) Somatic and dendritic small-conductance calcium-activated potassium channels regulate the output of cerebellar Purkinje neurons. *J Neurosci* 23:2600–2607.
6. Womack MD, Khodakhah K (2002) Characterization of large conductance Ca^{2+}-activated K$^+$ channels in cerebellar Purkinje neurons. *Eur J Neurosci* 16:1214–1222.
7. Edgerton JR, Reinhart PH (2003) Distinct contributions of small and large conductance Ca^{2+}-activated K$^+$ channels to rat Purkinje neuron function. *J Physiol* 548:53–69.
8. Gruol DL, Jacquin T, Yool AJ (1991) Single-channel K$^+$ currents recorded from the somatic and dendritic regions of cerebellar Purkinje neurons in culture. *J Neurosci* 11: 1002–1015.
9. Knaus HG, et al. (1996) Distribution of high-conductance Ca(2+)-activated K+ channels in rat brain: Targeting to axons and nerve terminals. *J Neurosci* 16:955–963.
10. Haghdoost-Yazdi H, Janahmadi M, Behzadi G (2008) Iberiotoxin-sensitive large conductance Ca^{2+} -dependent K$^+$ (BK) channels regulate the spike configuration in the burst firing of cerebellar Purkinje neurons. *Brain Res* 1212:1–8.
11. Cheron G, et al. (2009) BK channels control cerebellar Purkinje and Golgi cell rhythmicity in vivo. *PLoS ONE* 4:e7991.
12. Orr HT (2004) Into the depths of ataxia. *J Clin Invest* 113:505–507.
13. Shakkottai VG, et al. (2004) Enhanced neuronal excitability in the absence of neurodegeneration induces cerebellar ataxia. *J Clin Invest* 113:582–590.
14. Llinás RR (2009) Inferior olive oscillation as the temporal basis for motricity and oscillatory reset as the basis for motor error correction. *Neuroscience* 162:797–804.
15. Jacobson GA, Rokni D, Yarom Y (2008) A model of the olivo-cerebellar system as a temporal pattern generator. *Trends Neurosci* 31:617–625.
16. Welsh JP, Lang EJ, Suglhara I, Llinás R (1995) Dynamic organization of motor control within the olivocerebellar system. *Nature* 374:453–457.
17. De Zeeuw CI, Berrebi AS (1995) Postsynaptic targets of Purkinje cell terminals in the cerebellar and vestibular nuclei of the rat. *Eur J Neurosci* 7:2322–2333.
18. De Zeeuw CI, Wylie DR, DiGiorgi PL, Simpson JI (1994) Projections of individual Purkinje cells of identified zones in the flocculus to the vestibular and cerebellar nuclei in the rabbit. *J Comp Neurol* 349:428–447.
19. Fredette BJ, Mugnaini E (1991) The GABAergic cerebello-olivary projection in the rat. *Anat Embryol (Berl)* 184:225–243.
20. Barski JJ, Dethleffsen K, Meyer M (2000) Cre recombinase expression in cerebellar Purkinje cells. *Genesis* 28:93–98.
21. Kitamura K, Judkewitz B, Kano M, Denk W, Häusser M (2008) Targeted patch-clamp recordings and single-cell electroporation of unlabeled neurons in vivo. *Nat Methods* 5:61–67.
22. Miall RC, Keating JG, Malkmus M, Thach WT (1998) Simple spike activity predicts occurrence of complex spikes in cerebellar Purkinje cells. *Nat Neurosci* 1:13–15.
23. Murphy JT, Sabah NH (1970) Spontaneous firing of cerebellar Purkinje cells in decerebrate and barbiturate anesthetized cats. *Brain Res* 17:515–519.
24. Häusser M, Clark BA (1997) Tonic synaptic inhibition modulates neuronal output pattern and spatiotemporal synaptic integration. *Neuron* 19:665–678.
25. Loewenstein Y, et al. (2005) Bistability of cerebellar Purkinje cells modulated by sensory stimulation. *Nat Neurosci* 8:202–211.
26. Eccles JC, Llinás R, Sasaki K (1966) The excitatory synaptic action of climbing fibres on the purinje cells of the cerebellum. *J Physiol* 182:268–296.
27. Miyakawa H, Lev-Ram V, Lasser-Ross N, Ross WN (1992) Calcium transients evoked by climbing fiber and parallel fiber synaptic inputs in guinea pig cerebellar Purkinje neurons. *J Neurophysiol* 68:1178–1189.
28. Maejima T, Hashimoto K, Yoshida T, Aiba A, Kano M (2001) Presynaptic inhibition caused by retrograde signal from metabotropic glutamate to cannabinoid receptors. *Neuron* 31:463–475.
29. Konnerth A, Llano I, Armstrong CM (1990) Synaptic currents in cerebellar Purkinje cells. *Proc Natl Acad Sci USA* 87:2662–2665.
30. Zagha E, Lang EJ, Rudy B (2008) Kv3.3 channels at the Purkinje cell soma are necessary for generation of the classical complex spike waveform. *J Neurosci* 28:1291–1300.
31. Llinás R, Volkind RA (1973) The olivo-cerebellar system: Functional properties as revealed by harmaline-induced tremor. *Exp Brain Res* 18:69–87.
32. Marshall SP, Lang EJ (2009) Local changes in the excitability of the cerebellar cortex produce spatially restricted changes in complex spike synchrony. *J Neurosci* 29:14352–14362.
33. Lang EJ, Sugihara I, Llinás R (1996) GABAergic modulation of complex spike activity by the cerebellar nucleoolivary pathway in rat. *J Neurophysiol* 76:255–275.
34. Barski JJ, et al. (2003) Calbindin in cerebellar Purkinje cells is a critical determinant of the precision of motor coordination. *J Neurosci* 23:3469–3477.
35. Levin SI, et al. (2006) Impaired motor function in mice with cell-specific knockout of sodium channel Scn8a (NaV1.6) in cerebellar purkinje neurons and granule cells. *J Neurophysiol* 96:785–793.
36. Kalume F, Yu FH, Westenbroek RE, Scheuer T, Catterall WA (2007) Reduced sodium current in Purkinje neurons from Nav1.1 mutant mice: implications for ataxia in severe myoclonic epilepsy in infancy. *J Neurosci* 27:11065–11074.
37. Walter JT, Alviña K, Womack MD, Chevez C, Khodakhah K (2006) Decreases in the precision of Purkinje cell pacemaking cause cerebellar dysfunction and ataxia. *Nat Neurosci* 9:389–397.
38. Hoebeek FE, et al. (2005) Increased noise level of purkinje cell activities minimizes impact of their modulation during sensorimotor control. *Neuron* 45:953–965.
39. Waters MF, et al. (2006) Mutations in voltage-gated potassium channel KCNC3 cause degenerative and developmental central nervous system phenotypes. *Nat Genet* 38: 447–451.
40. McMahon A, et al. (2004) Allele-dependent changes of olivocerebellar circuit properties in the absence of the voltage-gated potassium channels Kv3.1 and Kv3.3. *Eur J Neurosci* 19:3317–3327.
41. Rochefort NL, et al. (2009) Sparsification of neuronal activity in the visual cortex at eye-opening. *Proc Natl Acad Sci USA* 106:15049–15054.
42. Stosiek C, Garaschuk O, Holthoff K, Konnerth A (2003) In vivo two-photon calcium imaging of neuronal networks. *Proc Natl Acad Sci USA* 100:7319–7324.
43. Takechi H, Eilers J, Konnerth A (1998) A new class of synaptic response involving calcium release in dendritic spines. *Nature* 396:757–760.

Supporting Information

Chen et al. 10.1073/pnas.1001745107

SI Materials and Methods

Generation of Purkinje Neuron–Specific BK$^{-/-}$ Mice. For establishing a mouse line with a tissue-specific deletion of BK channel α-subunit in Purkinje neurons (PN-BK$^{-/-}$), constitutive heterozygous BK L1/+ mice (SV129 background) were intercrossed with transgenic mice expressing the Cre recombinase under the control of the Purkinje protein 2 (PNP2) gene, which is thought to be specifically expressed in PNs and in retinal bipolar neurons (1). The generation of this PNP2-Cre mouse line was described in detail by Barski et al. (1). Progenies both carrying one BK L1 allele and being transgenic for PNP2-Cre were then crossed with mice carrying two *loxP*-flanked L2 alleles (BK L2/L2; SV129 background) of the BK gene *KCNMA1* (2) to obtain PNP2-Cre transgenic BK L2/L1 (PN-BK$^{-/-}$) and PNP2-Cre transgenic BK L2/+ (PN-BK-Control) mice. The correct genotype was analyzed by PCR amplification as described previously (Fig. S1) (1, 2).

Mice were bred and maintained at the animal facility of the Institute of Pharmacy, Department Pharmacology and Toxicology, University of Tübingen, Germany. Either litter- or age-matched mice (at an age of 3 to 4 months) were randomly assigned to the experimental procedures with respect to the German legislation on animal protection. All experimental procedures were performed in accordance with institutional animal welfare guidelines and were approved by the state government of Bavaria, Germany.

Immunohistochemistry and Silver Staining. Mice were killed in a CO_2 chamber and perfused with 50 mM PBS (ice-cold), followed by 4% PFA in PBS (ice-cold) for 4 min. Brains were removed, incubated in ascending concentrations of sucrose (5% 1 h/10% 12 h/20% 24 h) and snap frozen at −80 °C in isopentane. Immunohistochemistry was conducted as described previously (3). Briefly, free-floating coronal cryostat sections (40 μm) were permeabilized in three changes (20 min each) of Tris-buffered saline (TBS; 100 mM Tris/HCl and 150 mM NaCl, pH = 7.4) with 0.2% Triton X-100 (TBS-T). Endogenous peroxidases were blocked in 25% methanol and 0.6% H_2O_2 in TBS for 20 min. Samples were washed once in TBS and twice in TBS-T. Protein blocking was conducted with 2% BSA and 2% normal goat serum in TBS-T for 1 h. Samples were incubated with mouse monoclonal anti-BKα$_{(690\text{-}715)}$ antibody (1:1,000; NeuroMab Clone L6/60) in TBS-T/1% BSA overnight at 4 °C, washed thrice with TBS-T (20 min each), and incubated with HRP-tagged goat anti-mouse antibody (1:300; DAKO P0447) for 2 h. After three washes with TBS, slices were developed using the standard diaminobenzidine method. Sections were mounted on gelatin-coated slices in 60% ethanol, dried on a hot plate (60 °C) for 15 min, dehydrated in 96% and 100% ethanol, cleared in xylene, and sealed in Entellan. Imaging was performed using a Zeiss Axioplan II microscope equipped with an AxioCam digital color camera (Fig. S1).

Silver staining was performed using a modified Sevier-Munger procedure. Free-floating cryostat sections were postfixed in 4% formalin in water (15 min) and washed thrice in deionized water. Sections were incubated in 20% silver nitrate for 15 min at 60 °C, rinsed once in deionized water, and developed in ammoniacal silver solution (10%) containing sodium bicarbonate and formalin. Samples were rinsed in distilled water, and excess silver was removed in 5% sodium thiosulfate for 10 min. Mounting, dehydration, and sealing were conducted as described above.

Behavioral Tests. ***Footprint pattern.*** Paw positions were recorded while mice were walking on a glass plate with a video camera position underneath the plate (4).

Ladder walking test. The horizontal ladder walking test was similar to the one designed for testing rats described previously (5). The ladder runway was composed of 38 rods with a diameter of 2 mm positioned at intervals of 2 cm. Each test consisted of at least two runs on the ladder. Slips of the fore- and hindlimbs were counted.

Elevated bar balancing test. The setup consisted of a 50 × 1-cm bar that connected two platforms located 50 cm above the ground. The animals were placed perpendicularly onto the bar and had to move toward one end until they reached a platform. This procedure was repeated to observe at least 20 walking steps. Both fore- and hindlimb slips from the bar were counted.

The trials were filmed at a rate of 30 frames per second using a digital video camera and analyzed frame by frame off-line. Statistical analysis was performed by using the Mann-Whitney *U* test (ladder walking, elevated bar) or χ^2 test (footprint pattern).

In Vivo Electrophysiological Recordings. Adult mice (1–4 months old) were used in all of the experiments. Surgery was performed in accordance with institutional animal welfare guidelines as described previously (6, 7). Briefly, the mice were placed onto a warming plate (38 °C) and anesthetized by inhalation of 1.5% isoflurane (Curamed) in pure O_2. The depth of anesthesia was assessed by monitoring the tail-pinch reflex and the respiration rate. After locally applying an anesthetic agent (xylocaine), the skin and muscles were removed under a dissecting microscope. A custom-made recording chamber was then glued to the skull with cyanoacrylic glue (UHU). A rectangular craniotomy (2.5 mm × 4.0 mm) was made using a high-speed drill with a small-tip steel burr (0.5 mm in diameter) to expose the cerebellar vermis (coordinates: Bregma −5.5 to −7.5 mm, ±1 mm lateral to the midline) (8). The craniotomy was then filled with 1.5% low-melting-point agarose (Sigma) to minimize brain pulsations. After surgery, the mouse was transferred into the recording setup and continuously supplied, through a face mask, with 0.8–1.2% isoflurane in pure O_2. The recording chamber was perfused with warm (36.5 °C) normal Ringer's solution containing (in millimolars) 125 NaCl, 4.5 KCl, 26 $NaHCO_3$, 1.25 NaH_2PO_4, 2 $CaCl_2$, 1 $MgCl_2$, and 20 glucose, pH 7.4, when bubbled with 95% O_2 and 5% CO_2. During surgical and recording procedures, the rectal temperature of mouse was maintained at 36.5–37.5 °C with a warming plate.

Somatic cell-attached patch-clamp recordings were obtained with an EPC9/2 amplifier (HEKA Elektronik) under two-photon imaging. Two-photon imaging was performed with a custom-built video-rate two-photon microscope based on a resonance scanner (9) and a mode-locked femto-second pulse laser, operating at 710–920 nm wavelength (MaiTai; Spectra Physics). The scanner was mounted on an upright microscope (BX61WI; Olympus) equipped with a ×40/0.80-W water-immersion objective (Nikon). A patch pipette filled with normal Ringer's solution containing 50 μM Alexa594 (Invitrogen) had a tip resistance of 4–6 MΩ. The details of the shadow-patching process for PNs were described previously (10). After recording, some cells were fluorescently labeled by using targeted single-cell electroporation (10). The identity of PNs was confirmed by the reconstructed projection images of dye-filled cells. 3D reconstructions were performed using either ImageJ (http://rsbweb.nih.gov/ij/) or Amira (http://www.amiravis.com/). In some experiments, cell-attached recordings to monitor climbing fiber activity using both electrical and dendritic Ca^{2+} measurements were performed in PNs that were prelabeled with Oregon Green BAPTA-1 via electroporation (10). For local drug application to PNs, a glass pipette filled with Alexa594 and the corresponding drug was placed near (20–50 μm) the dendrites of a PN under two-photon imaging guidance. The drug and Alexa594 were coreleased by gentle pressure application (Picospritzer III; General Valve).

Electrophysiological data were filtered at 10 kHz and sampled at 20–50 kHz using Pulse software (HEKA). Simple and complex spikes (SS and CS) from extracellular recordings were sorted according to their amplitudes, shapes, and time courses using Igor Pro (Wavemetrics) in conjunction with the Neuromatic software package (version 2.00) and a custom-written macro. A 1-s or a 10-s time window was used for detecting events and for computing the frequency of SS or CS, respectively. Statistical analysis was performed with SPSS 10.0 for Windows (SPSS).

1. Barski JJ, Dethleffsen K, Meyer M (2000) Cre recombinase expression in cerebellar Purkinje cells. *Genesis* 28:93–98.
2. Sausbier M, et al. (2004) Cerebellar ataxia and Purkinje cell dysfunction caused by Ca^{2+}-activated K^+ channel deficiency. *Proc Natl Acad Sci USA* 101:9474–9478.
3. Sausbier U, et al. (2006) Ca^{2+} -activated K^+ channels of the BK-type in the mouse brain. *Histochem Cell Biol* 125:725–741.
4. Hartmann J, et al. (2008) TRPC3 channels are required for synaptic transmission and motor coordination. *Neuron* 59:392–398.
5. Metz GA, Whishaw IQ (2002) Cortical and subcortical lesions impair skilled walking in the ladder rung walking test: A new task to evaluate fore- and hindlimb stepping, placing, and co-ordination. *J Neurosci Methods* 115:169–179.
6. Rochefort NL, et al. (2009) Sparsification of neuronal activity in the visual cortex at eye-opening. *Proc Natl Acad Sci USA* 106:15049–15054.
7. Stosiek C, Garaschuk O, Holthoff K, Konnerth A (2003) In vivo two-photon calcium imaging of neuronal networks. *Proc Natl Acad Sci USA* 100:7319–7324.
8. Franklin K, Paxinos G (2001) *The Mouse Brain in Stereotaxic Coordinates* (Academic Press Inc., San Diego).
9. Leybaert L, de Meyer A, Mabilde C, Sanderson MJ (2005) A simple and practical method to acquire geometrically correct images with resonant scanning-based line scanning in a custom-built video-rate laser scanning microscope. *J Microsc* 219:133–140.
10. Kitamura K, Judkewitz B, Kano M, Denk W, Häusser M (2008) Targeted patch-clamp recordings and single-cell electroporation of unlabeled neurons in vivo. *Nat Methods* 5:61–67.

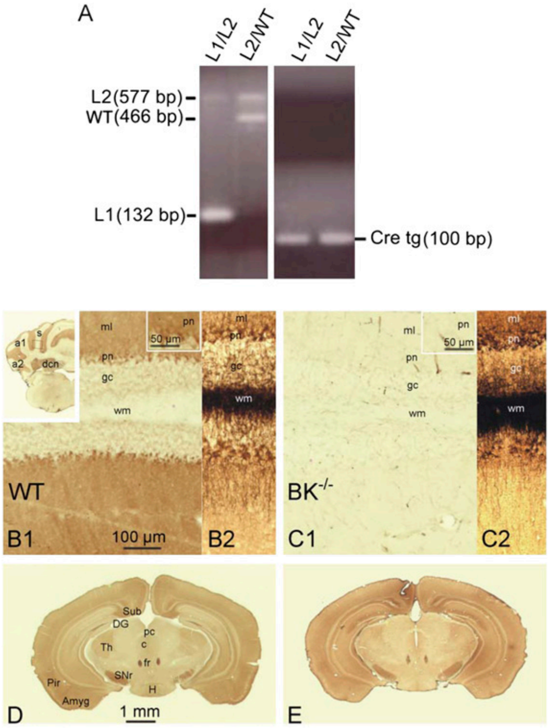

Fig. S1. Genotyping of Purkinje neuron–specific $BK^{-/-}$ mice ($PN\text{-}BK^{-/-}$) and immunohistochemistry. (*A*) PCR was used to genotype $PN\text{-}BK^{-/-}$ (PCP2-Cre tg BK L1/L2) and control (PCP2-Cre tg BK L2/WT) mice. (*B1, C1*) Immunostaining for BK channels in the cerebellar cortex of WT (*B1*) and $PN\text{-}BK^{-/-}$ (*C1*) mice. In WT, strong staining was observed in the PN layer (pn) containing the cell bodies of PNs and the molecular layer (ml) containing their dendrites. In line with previous reports (1, 2), the staining in the granule cell layer (gc) was weak. In $PN\text{-}BK^{-/-}$, staining in the pn and ml was strongly reduced. *Left Inset:* rectangle depicts region shown in *B* and *C*. a1/a2, ansiform lobule crus1/2; S, simple lobule; dcn, deep cerebellar nuclei; wm, white matter. *Right Insets:* PNs are readily seen in WT mice (*B1*) but not in $PN\text{-}BK^{-/-}$ mice (*C1*). (*B2, C2*) Silver staining shows that PNs can be observed in both WT (*B2*) and $PN\text{-}BK^{-/-}$ mice (*C2*). (*D* and *E*) Immunostaining for BK channels in the whole brain. In both WT (*D*) and $PN\text{-}BK^{-/-}$ (*E*) mice, strong BK channel expression was seen in different regions. Amyg, amygdala; Pir, piriform cortex; Th, thalamus; DG, dentate gyrus; Sub, subiculum; SNr, substantia nigra, pars compacta; H, hypothalamus; c: central gray matter (periaqueductal gray); fr, fasciculus retroflexus; pc, posterior commissure.

1. Barski JJ, Dethleffsen K, Meyer M (2000) Cre recombinase expression in cerebellar Purkinje cells. *Genesis* 28:93–98.
2. Sausbier M, et al. (2004) Cerebellar ataxia and Purkinje cell dysfunction caused by Ca^{2+}-activated K^+ channel deficiency. *Proc Natl Acad Sci USA* 101:9474–9478.

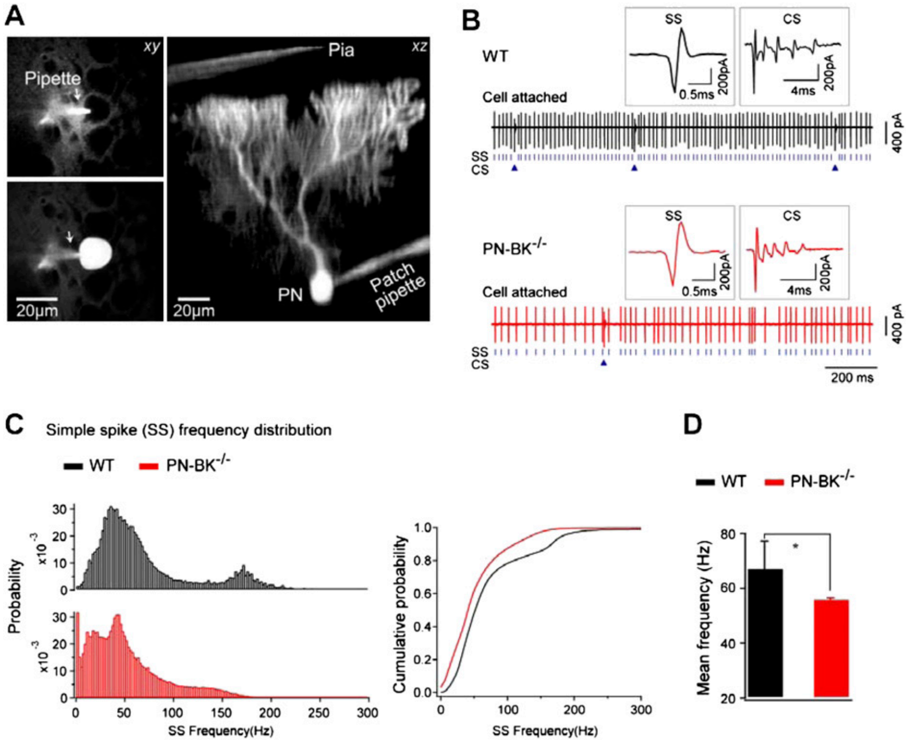

Fig. S2. Reduction in simple spike firing in PNs of PN-BK$^{-/-}$. (*A*) Visual identification of PN using in vivo two-photon imaging. A pipette filled with Alexa594 (50 μM) (arrow) was attached to the soma of a PN before (*Upper Left*) and after (*Lower Left*) electroporation. *Right: xz* projection showing the reconstruction of an electroporated PN. (*B*) Representative cell-attached recording from a WT (*Upper*, black) or PN-BK$^{-/-}$ (*Lower*, red) PN. *Insets:* SS and CS waveforms from both genotypes. (*C*) *Left:* Distribution of SS instantaneous frequency in WT (black) and PN-BK$^{-/-}$ (red) mice (bin = 2 Hz). *Right:* Cumulative distribution calculated from *Left* showing left-shift of SS frequency in PN-BK$^{-/-}$. (*D*) Comparison of mean frequency of SS in WT (black) and PN-BK$^{-/-}$ (red). The mean frequency was calculated from 2-min recording for each cell. ($n = 34$ WT cells and 57 PN-BK$^{-/-}$ cells in 10 mice for each genotype.) $*P < 0.05$. Error bars show SEM.

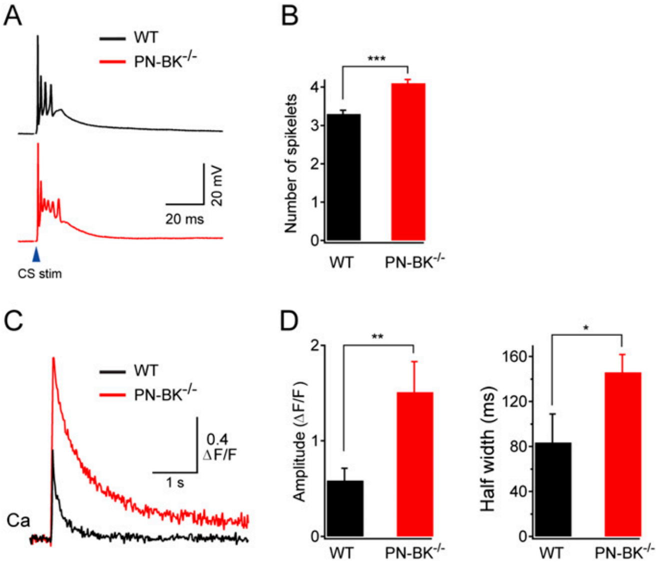

Fig. S3. Changes of complex spike waveform and complex spike-associated dendritic Ca^{2+} transient in PNs of PN-BK$^{-/-}$ in slice preparation. (*A*) Representative complex spikes from WT (*Upper*, black) and PN-BK$^{-/-}$ (*Lower*, red) mice. (*B*) Comparison of spikelets number of CS between WT (black) and PN-BK$^{-/-}$ (red) (30 CSs; 6 CSs from each cell; $n = 5$ cells for each genotype.) $***P < 0.001$. Error bars show SEM. (*C*) Averaged climbing fiber–evoked Ca^{2+} transients from WT (black) and PN-BK$^{-/-}$ (red). Each trace was averaged from five events (each event from each cell; $n = 5$ cells for each genotype). (*D*) Comparison of the amplitude (*Left*) and half width (*Right*) of Ca^{2+} transient in WT (black) and PN-BK$^{-/-}$ (red) (20 Ca^{2+} transients, 4 Ca^{2+} transients from each cell; $n = 5$ cells for each genotype). $**P < 0.01$; $*P < 0.05$. Error bars show SEM.

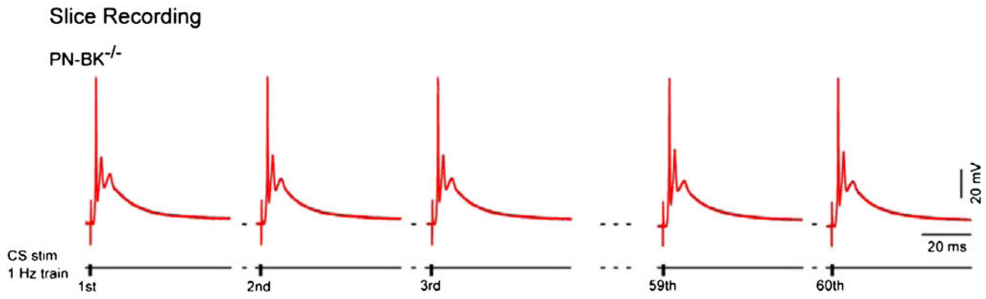

Fig. S4. Stable complex spike waveform during repetitive stimulation in PNs of PN-BK$^{-/-}$ mice. Current-clamp recordings were performed in cerebellar slice preparations. Complex spikes were elicited by a stimulation electrode placed in the granule layer. Sixty consecutive complex spikes were recorded in response to 1 Hz stimulation. Note that no detectable difference was found between the first and the 60th CS. Similar results were obtained in six PNs.

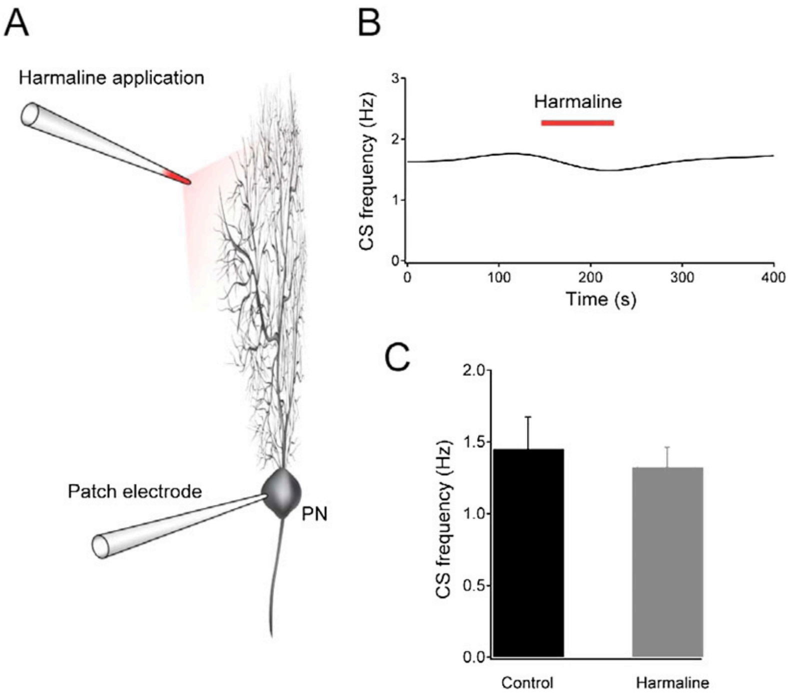

Fig. S5. No significant effect of harmaline on CS frequency by local application to the recorded PN in vivo. (*A*) Schematic presentation showing the experimental design. The glass pipette for drug application was filled with both Alexa594 and harmaline. The patch electrode is shown for cell-attached recording. Before performing cell-attached recording and placing the drug pipette, the cell was labeled with Alexa594 by electroporation. (*B*) Example of the time course showing no effect of harmaline on CS frequency in one cell. (*C*) Summary of data in *B*, showing the average CS frequency before and during harmaline application (n = 4 PNs). Error bars show SEM.

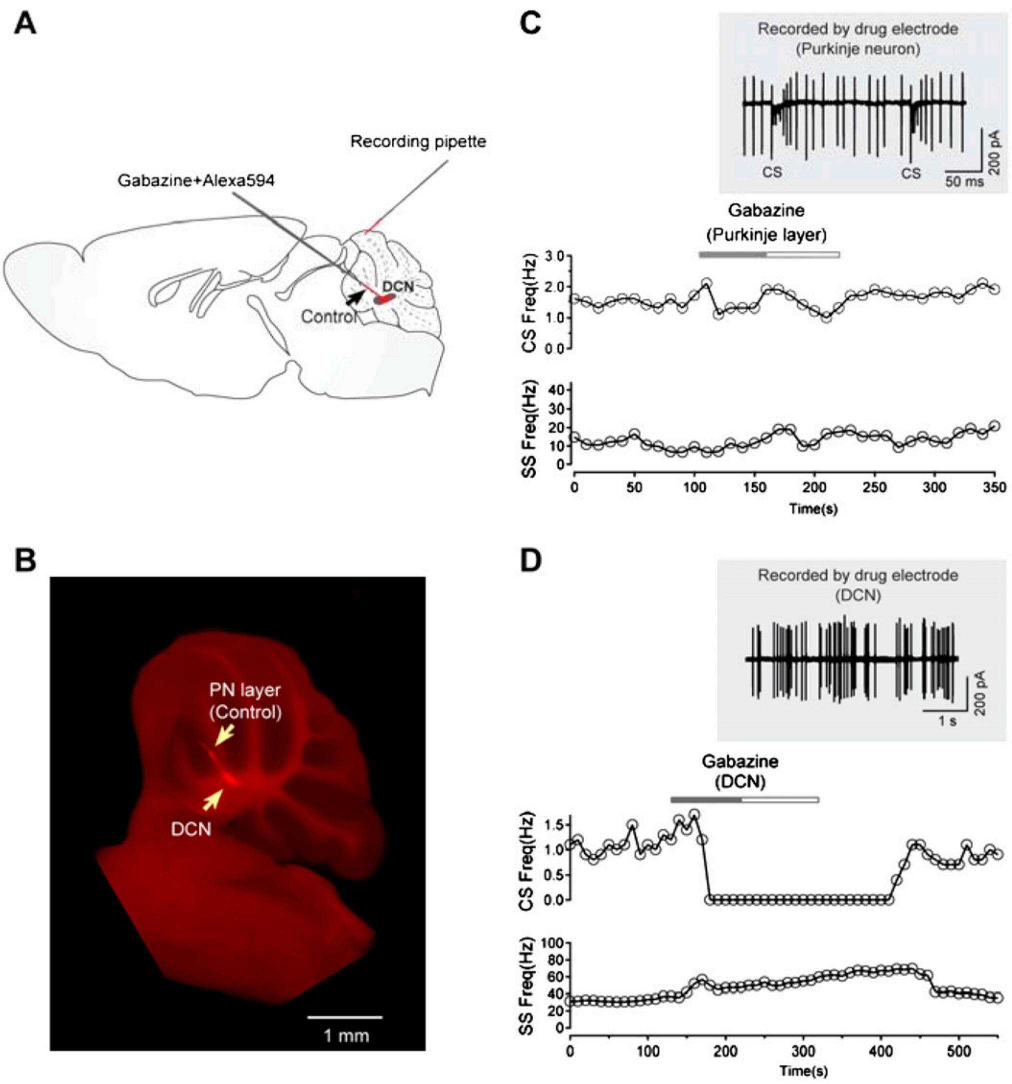

Fig. S6. Control for the site-specific action of gabazine application to the deep cerebellar nuclei (DCN). (*A*) Experimental configuration for cell-attached recordings from PNs and local drug application (gabazine, 200 μM) to the DCN and to a control location (arrow) near the DCN. (*B*) Fluorescence image of an acute slice preparation with the tract of the gabazine and Alexa594-containing pipette. The slice was obtained immediately after the end of the in vivo recordings (see *SI Materials and Methods*). The arrows indicate the approximate sites of gabazine application: first, the cerebellar PN layer, approximately 500 μm away from the DCN (*C*) and, second, the DCN (*D*). Note that the position of the recording patch-pipette (not shown) was in a different plane of focus, approximately 2.5 mm away from the DCN. (*C*) Local application of gabazine at the site of PN layer (marked in *B*) had no detectable effect on CS and SS activities recorded by the recording pipette (location indicated in *A*). Before gabazine injection, the location of PN layer was identified by the drug pipette-based recording of the characteristic CS activity from one PN (*Inset*). (*D*) Local application of gabazine to the DCN blocked the CS and increased the SS activity. Before gabazine application, the spontaneous activity of a DCN neuron was monitored by the drug pipette in the loose cell-attached configuration (*Inset*). These results verify the specificity of the gabazine application to the DCN.

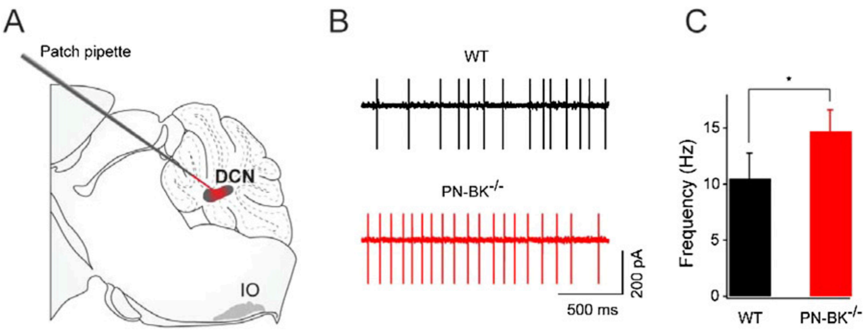

Fig. S7. Increased activity in deep cerebellar nuclei (DCN) neurons PN-BK$^{-/-}$ mice in vivo. (*A*) Experimental configuration for extracellular recordings in DCN neurons in vivo. (*B*) Examples of extracellular activity from DCN neurons in WT (*Upper*, black) and PN-BK$^{-/-}$ (*Lower*, red). The spikes are truncated in amplitude. (*C*) Comparison of mean frequency of DCN neuron activity in both genotypes (n = 16 WT cells and 14 PN-BK$^{-/-}$ cells). *$P < 0.05$. Error bars show SEM.

Table S1. Summary of mean frequencies of CS and SS in WT and PN-BK$^{-/-}$ and effects of various pharmacological interventions

Treatment	Spike type	Subtype	Mean frequency (Hz)			
			PN-BK$^{-/-}$		WT	
None	SS	—		55.6 ± 1.0* (n = 57)		67.0 ± 10.3 (n = 34)
	CS	Normal		1.07 ± 0.08* (n = 18)		1.45 ± 0.06 (n = 32)
		Quiet		0.15 ± 0.03 (n = 13)		0.45 ± 0.08 (n = 2)
		Silent		0 (n = 26)		Not detected
Gabazine	CS	Not determined		Not tested	Before	1.60 ± 0.14 (n = 8)
					During	0.43 ± 0.16‡ (n = 8)
Muscimol	CS	Normal	Before	1.36 ± 0.08 (n = 5)	Before	1.55 ± 0.12 (n = 11)
			During	1.52 ± 0.09* (n = 5)		
		Quiet	Before	0.27 ± 0.09 (n = 7)		
			During	0.50 ± 0.12† (n = 7)	During	1.63 ± 0.15 (n = 11)
		Silent	Before	0 (n = 7)		
			During	0.11 ± 0.01‡ (n = 7)		
Harmaline	CS	Not determined	Before	0.41 ± 0.08 (n = 18)	Before	1.26 ± 0.13 (n = 7)
			During	4.07 ± 0.31‡ (n = 10)	During	3.98 ± 0.21† (n = 13)

*$P < 0.05$; $^{\dagger}P < 0.01$; $^{\ddagger}P < 0.001$ vs. WT or before drug application.

Project II

Basket cell-mediated regulation of sensory-evoked signalling in the cerebellar cortical circuitry *in vivo*

(Prepared for submission)

Abstract

The cerebellar cortex is critically involved in the processing of sensorimotor information. Sensory stimulation-evoked activity arises to the cerebellar cortex through the climbing fiber pathway as well as though the mossy fiber-parallel fiber pathway. Paradoxically, there is evidence that the activity of the excitatory mossy fiber-parallel fiber system transiently decreases the firing of Purkinje neurons, the sole output of the cerebellar cortex. The circuit mechanisms underlying this sensory-evoked reduction of the cerebellar cortical output signal is not entirely understood. Here we explored how whisker stimulation affected firing in different cell types of the mouse cerebellar cortex *in vivo* by using two-photon imaging-guided patch clamp recordings in combination with local pharmacological manipulations. We first found that in Purkinje neurons, the whisker stimulation-evoked reduction in simple spike activity was prevented by the local application of the $GABA_A$ receptor antagonist gabazine, suggesting a possible role of the two inhibitory interneurons of the cerebellar cortex, the basket and/or the stellate cells. Interestingly, whole-cell and cell-attached recordings demonstrated that whisker stimulation produced a strong increase of the firing rate in basket, but not in stellate cells. This increase in firing was blocked by the local application of CNQX, an antagonist of AMPA receptors. In stellate cells, a mild increase in firing rate was observed only following local gabazine application. Taken together, we find that basket cell-mediated feedforward inhibition shapes sensory evoked-activity of all cell types in the cerebellar cortex *in vivo*. Our results identify basket cell-mediated feedforward inhibition as a key mechanism underlying sensory-evoked reduction of the cerebellar cortical output signals.

Background

Cerebellar control of motor coordination relies heavily on the integration of the signals arising from a wide variety of sensory inputs [1]. Despite the relative simplicity of the microcircuitry of the cerebellar cortex, the sensory-evoked signal flow *in vivo* and the resulting activity in Purkinje neurons, the sole output stage of this circuit, are not fully understood. Purkinje neurons generate two types of signals: the characteristic complex spikes, resulting from the activity of afferent climbing fibers [2] and simple spikes, reflecting an interplay between afferent synaptic activity of the mossy fiber-parallel fiber pathway [3] and intrinsically driven mechanisms [4,5]. Both complex spike and simple spike signals can be modulated by sensory stimulation. It has been intensively reported that sensory stimuli are capable of evoking complex spike responses and increasing complex spike synchrony in neighboring Purkinje neurons [5-9]. However, sensory-evoked simple spike responses are largely variable: some Purkinje neurons exhibit an increase in simple spike firing, while others show a decrease or a combination of both or even no obvious response in anaesthetized animals [5,6,10,11]. More recently, such large variation of simple spike responses was also observed in awake mice [9]. These results suggest a possibility that multiple mechanisms may underlie the sensory-evoked signal flow in the granule cell-parallel fiber-Purkinje neuron pathway, thereby resulting in variable simple spikes responses in Purkinje neurons.

Sensory stimulation produces high-frequency action potential firing in both mossy fiber boutons and granule cells [12,13]. This activity is expected to lead to an activation of parallel fiber-Purkinje neuron synapses [2], which provides an explanation for the increase in simple spike response. However, at least two types of mechanisms have been proposed to be responsible for the decrease in simple spike response: 1) a temporary break of simple spikes or/and a downstate of firing caused by complex spikes during sensory stimulation, as supported by several reports [5,9,14-16]; and 2) feedforward inhibition from molecular layer interneurons, as predicted by computational modeling [17] and also suggested by experimental data [9,17,18]. Although such molecular layer inhibition has attracted recent attention as a mechanism, the possible sources of the inhibition remain unknown since two different types of interneurons, basket cells and stellate cells, are located in cerebellar molecular layer [2,4,19,20].

Sensory integration in the cerebellar cortex is often studied by using perioral cutaneous or whisker stimulation, which is reliably represented in Crus I and Crus IIa of the cerebellar hemisphere [5,6,12,13]. In the present study, we measured the responses to whisker stimulation in three types of cells, Purkinje neurons, basket cells and stellate cells, in the folium Crus IIa of the mouse cerebellum. By using *in vivo* two-photon imaging guided cell-attached and whole-cell patch clamp recordings, we find both complex spike and simple spike responses in the Purkinje neurons. By locally targeted pharmacological manipulations, we show that synaptic inhibition is one of the major mechanisms underlying the sensory-evoked decrease in simple spikes. Finally, we find that whisker stimulation remarkably produces responses in the basket cells but not in the stellate cells, indicating the basket cells as a possible source of feedforward inhibition onto the Purkinje neurons during sensory processing.

Materials and methods

Animal preparation.

C57BL/6 mice (30-60 postnatal days) were used in all the experiments. Surgery was performed in accordance with institutional animal welfare guidelines as described previously with slight modifications [21-23]. Briefly, the mice were placed onto a warming plate (37.5-38°C) and anesthetized with the full dosage of a mixture of fentanyl (0.05 mg/kg), midazolam (5.0 mg/kg) and medetomidin (0.5 mg/kg), an anesthesia protocol widely used for the study of sensory processing [24-28]. After applying a local anesthetic (xylocaine), the skin and muscles were removed under a dissecting microscope. A custom-made recording chamber was then glued to the skull with cyanoacrylic glue (UHU, Buhl-Baden, Germany). A small craniotomy (diameter: ~2 mm) was made using a high-speed drill with a small tip steel burr (0.5 mm in diameter) to expose the folium Crus IIa [29]. The craniotomy was then filled with 1.5% low-melting point agarose (Sigma, St. Louis, MO, USA) to minimize brain pulsations. After surgery, the mouse was transferred into the recording set-up and anesthesia was maintained by re-injection of the lower maintenance dosage of anesthetic (0.016 mg/kg fentanyl, 1.6 mg/kg midazolam, and 0.16 mg/kg medetomidin) every hour. Under these conditions, the respiration rate was as high as 200 breaths per minute (BPM), a level quite close to that observed during the awake state in mice (250-350 BPM) [30,31], indicating the light level of anesthesia in our studies. This level of anesthesia was also confirmed by the presence of robust tail-pinch or paw reflexes. The recording chamber was perfused with warmed (36.5-37.5°C) normal Ringer's solution containing (in mM): 125 NaCl, 4.5 KCl, 26 $NaHCO_3$, 1.25 NaH_2PO_4, 2 $CaCl_2$, 1 $MgCl_2$, 20 glucose, pH 7.4, when bubbled with 95% O_2 and 5% CO_2. During surgical and recording procedures, the rectal temperature of mouse was maintained at 36.5-37.5 °C with a warming plate.

In vivo electrophysiological recordings.

Somatic cell-attached and whole-cell patch clamp recordings were obtained with an EPC10 amplifier (USB Quadro Amplifier, HEKA Elektronik, Lambrecht/Pfalz, Germany) under two-photon imaging guidance. Two-photon imaging was performed with a custom-built video-rate two-photon microscope based on a resonant scanner [32] and a mode-locked femtosecond pulse laser, operating at 710-920 nm wavelength (MaiTai, Spectra Physics, Mountain View, CA). The scanner was mounted on an upright microscope (BX61WI, Olympus, Tokyo, Japan) equipped with a 40×/0.80 W water-immersion objective (Nikon, Japan). The patch pipette solution contained normal Ringer's solution with 50 µM Alexa594 (Invitrogen) for cell-attached recordings, or 148 mM potassium gluconate, 10 mM HEPES, 10 mM NaCl, 0.5 mM $MgCl_2$, 4 mM MgATP, 0.4 mM Na_2GTP, and 50 µM Alexa594, pH 7.3, for whole-cell recordings. The initial pipette resistance was 4-6 MΩ. For patch clamp recordings *in vivo* we used the shadow-patching approach [23,33]. For two-photon imaging, the average power delivered to the brain was in the range of 30-70 mW, and the excitation wavelength was 800 nm. The identification of neurons after cell-attached recordings was performed by labeling them with the fluorescent dye Alexa594 using electroporation [23,33,34]. 3D reconstructions of these neurons were performed using the software package ImageJ (http://rsbweb.nih.gov/ij/). In some recordings of cerebellar interneurons, the pipette solution also contained 0.2% biocytin for post-hoc morphological verification. In brief, the cerebellar slices were made after *in vivo* recording and then fixed in 4% paraformaldehyde. Biocytin was labeled by streptavidin conjugated with a fluorescent dye Alexa488 (1:500). The images of fluorescently labeled neurons were checked and taken using a confocal-laser scanning microscope (Olympus BX61WI, Japan).

Local drug application and sensory stimulation.

For targeted drug application, a patch pipette filled with a mixture of the pharmacological agent and Alexa594 (50 µM) was placed near (50-100 µm) to the recorded cell under two-photon imaging guidance. The resistance of pipette (4-6 MΩ) was continuously monitored before, during and after drug application. The drug and Alexa594 were co-released by gentle pressure application (Picospritzer III, General Valve). For whisker stimulation, air-puffs (30 p.s.i.) were delivered through a plastic pipette (tip diameter: 0.5 mm) that was placed 5 mm in front of the ipsilateral whiskers and connected to a pressure device (Picospritzer III, General Valve).

Data acquisition and analysis.

Electrophysiological data were filtered at 10 kHz and sampled at 20-50 kHz using Pulse software (HEKA, Lambrecht, Germany). Simple and complex spikes (SS and CS) were sorted according to their amplitudes, shapes and time courses using Igor Pro (Wavemetrics) in conjunction with the Neuromatic software package and custom-written macros. Statistical analyses were performed using paired or unpaired Student's t-tests, as appropriate, with SPSS (SPSS Inc, Chicago, USA) ($p < 0.05$ was considered significantly).

Results

Sensory stimulation deceases simple spike activity in Purkinje neurons

We first monitored the spontaneous and sensory-evoked responses in Purkinje neurons using *in vivo* two-photon imaging-based electrophysiological measurements in anesthetized mice [23,33,35]. Sensory stimulation was achieved by delivering brief air puffs to the ipsilateral vibrissae. Two states of membrane potential have been found previously in Purkinje neurons: a depolarized state with continuous simple spike firing (referred to as upstate) and a hyperpolarized state with the absence of simple spikes (referred to as downstate) [5,36-38]. In our experimental condition, whole-cell patch clamp recordings revealed that only a small number of Purkinje neurons in the folium Crus IIa spontaneously exhibited these two stable states (14%; n = 4/28 cells), while the majority of neurons exhibited a persistent upstate, to which we refer to as tonically firing neurons (86%; n = 24/28 neurons) (Fig. 1). To examine the effect of sensory stimulation on simple spike activity without being affected by the spontaneous state transitions, we analyzed the sensory responses only in the tonically firing Purkinje neurons.

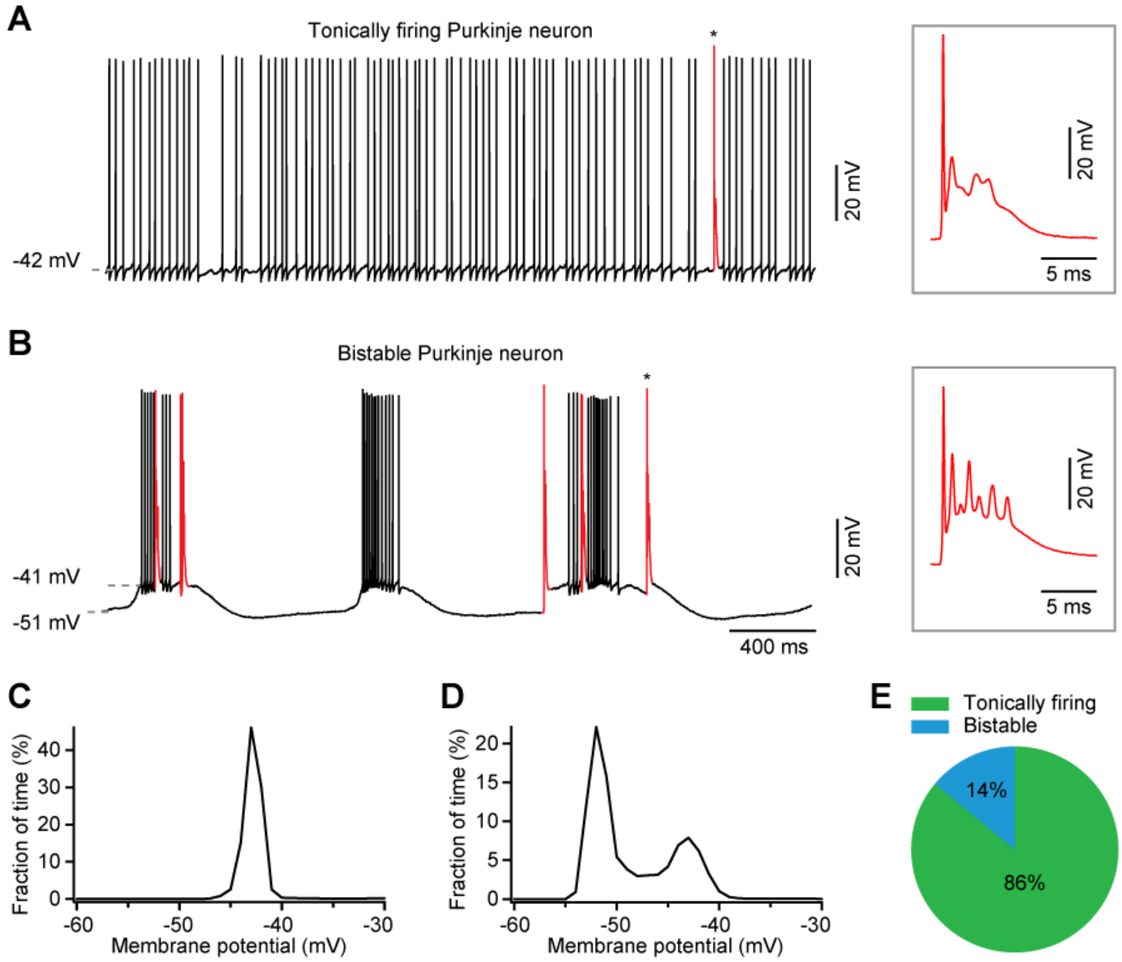

Figure 1. Spontaneous activity of Purkinje neurons in anesthetized mice. ***A***, Example of whole-cell recording of tonically firing Purkinje neurons. ***B***, Example of bistable Purkinje neurons. Insets, examples of complex spike in an expanded time scale, as indicated by as asterisk in the right panels. Red, complex spike; black, simple spike. ***C***, The distribution of the membrane potential corresponding to the neuron in panel A, calculated from 100 s period of recordings (bin width = 1 mV). ***D***, The distribution of membrane potential corresponding to the neuron in panel B, calculated from a 100-s period of recording. ***E***, Pie chart summarizes the relative proportion of tonically firing and bistable Purkinje neurons (n = 28 cells).

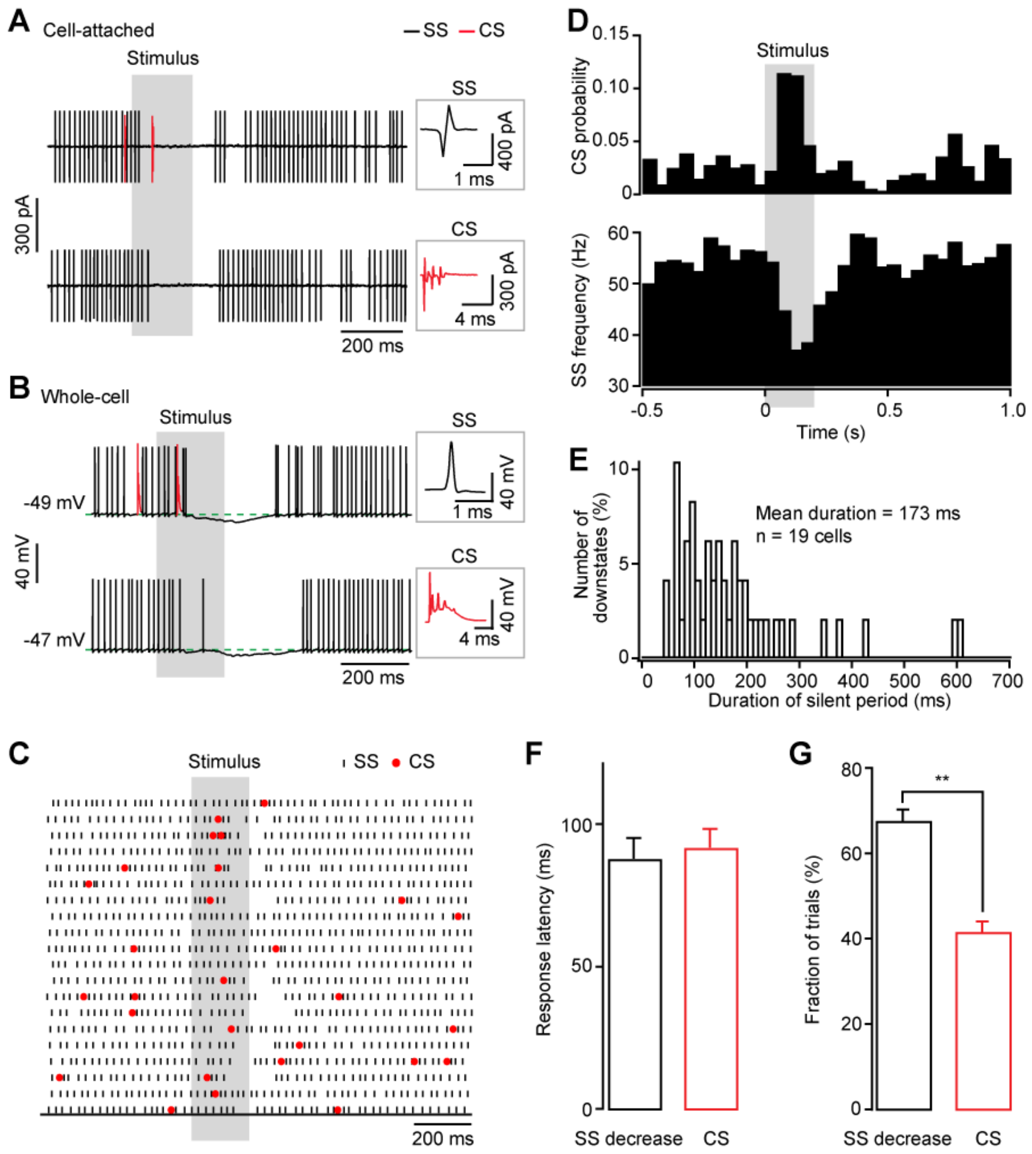

Figure 2. Whisker stimulation-evoked decrease in simple spikes in Purkinje neurons. ***A*** and ***B***, Cell-attached recording (two consecutive trials) (A) and subsequent whole-cell recording (two consecutive trials) (B) from a cerebellar Purkinje neuron showing typical decrease in simple spike activity evoked by whisker stimulation. Insets show examples of simple spike (SS) and complex spike (CS) in an expanded time scale. Red, complex spike; black, simple spike. The amplitude of spikes in cell-attached recording is truncated for clarity. In this and all other figures, the vertical grey stripe indicates the period of whisker stimulation. ***C***, Raster plot of whisker-evoked responses (20 consecutive trials) from cell-attached recording in a Purkinje neuron. ***D***, Averaged peristimulus time histogram of CS response probability (upper panel) and SS frequency (lower panel) computed from 10 consecutive trials of individual cells (*n* = 13 cell-attached recordings, 6 whole-cell recordings). The CS response probability was calculated by the number of events occurring in the time window (bin width) divided by the total number of events. ***E***, Distribution of the duration of sensory-evoked SS decrease (*n* = 19). ***F***, Latency of evoked SS decrease (left) and CS (right) from the onset of stimulus (*n*

= 19). ***G***, Comparison of the fraction of responsive trials for SS decrease and CS (*n* = 19). Error bars show SEM. **, $p < 0.01$.

As previously reported in different species [5-9], we found that both in cell-attached and whole-cell patch clamp configurations, sensory stimuli evoked complex spikes in 42 ± 2 % of the trials in Purkinje neurons (*n* = 13 using cell-attached recordings and 6 using whole-cell recordings) (Fig. 2). The latency of the evoked complex spikes from the onset of the stimulus was 93 ± 6 ms (*n* = 19 cells), comparable to that observed in previous studies [5,6]. In addition to the whisker stimulation-induced increase in response probability of complex spikes, we also found a pronounced transient decrease in simple spike activity in even a larger number of trials (68 ± 2 %) (Fig. 2*A*-*E*) in these tested cells, as recently found by using extracellular recordings in both anesthetized and awake mice [9]. The onset of whisker stimulation-induced decrease periods had a mean latency (89 ± 7 ms, *n* = 19 cells) and was, thus, very similar to that of the stimulus-evoked complex spikes (Fig. 2*F*), while the duration of the decrease periods (173 ± 18 ms, *n* = 19 cells) markedly exceeded the stimulus duration (Fig. 2*D*, *E*). Unexpectedly and intriguingly, across the population, only a small proportion of the evoked decrease periods (12 ± 3 %) appeared to be directly triggered by the whisker stimulation-evoked complex spikes. In most of our recordings, complex spikes did not directly precede the decrease periods, while in many other instances decrease periods were evoked even in the absence of complex spike activity (Fig. 2*C*). Moreover, the fraction of stimulus-evoked decrease periods significantly exceeded that of stimulus-evoked complex spikes (Fig. 2*G*). Taken together, consistent with the recent data obtained using extracellular recordings [9], our observations suggest that other mechanisms independent of complex spikes may underlie or at least contribute to the whisker stimulation-evoked decrease in simple spike activity. In addition, in the folium Crus IIa as tested, we also found 7 Purkinje neurons exhibiting no response to whisker stimulation, 2 neurons only a complex spike response, and 1 neuron a complex spike response and a slight increase in simple spikes. As the main focus in this study is to understand the mechanisms of sensory-evoked decrease in simple spikes, these types of recordings were not included in our analysis.

The anesthesia level has been generally accepted to affect sensory-evoked responses of neurons [39]. Because of this, we compared the whisker-evoked responses in Purkinje neurons in the conditions of deep and light anesthesia. The different levels of anesthesia were achieved by injecting different dosages of anesthetics and confirmed by the respiration rate and the tail-pinch reflex. In four Purkinje neurons recorded from four mice respectively, we found that whisker-evoked complex spike responses were observed during both deep and light anesthesia. However, whisker-evoked decrease in simple spikes was only found during light anesthesia but not during deep anesthesia (Fig. 3), suggesting a dependence of simple spike response on anesthesia depth in our condition. This result is consistent with the previous finding that whisker responses in Purkinje neurons were more often observed and also were longer lasting in awake mice than those in anesthetized mice [9]. As the sensory-evoked decrease in simple spikes were found in both awake [9] and anesthetized states, the experimental conditions we provided here is suitable for the study of this type of simple spike response over a long period for stable recordings *in vivo*. Therefore, throughout our study, to study the sensory-evoked simple spike responses, the anesthesia was kept at very light level, as confirmed by the high respiration rate (> 200 BPM) and the appearance of tail-pinch reflex, a state close to that of awake animal (see also Materials and Methods) [30,31].

Feedforward inhibition mediates sensory-evoked decrease in simple spikes in Purkinje neurons

In view of the powerful control of the activity of Purkinje neurons by local inhibitory interneurons [4,20,40], we considered the possibility that GABAergic synaptic inhibition might be involved in the process of whisker stimulation-evoked decrease in simple spikes. To test this hypothesis, we focally applied a $GABA_A$ receptor antagonist gabazine (200 µM) to the recorded Purkinje neurons. To visualize the Purkinje neurons when local drug was applied, before cell-attached recordings the neurons were first labeled with the fluorescent dye Alexa594 using electroporation [23,33] (Fig. 4*A*). Gabazine application invariably increased the frequency and regularity of spontaneous simple spike activity (Fig. 4*B-D*), as previously observed in cerebellar slices [4]. Strikingly, in these conditions, the whisker stimulation-evoked decrease was converted into a massive increase in simple spike firing frequency in 69 ± 5 % of the trials in all cells tested (10 consecutive trials/cell, *n* = 9 cells) (Fig. 4*B-D*). In these successful trials, the stimulus-evoked frequency increase ranged from 30% up to 500% (mean increase 213% ± 30%; *n* = 9 cells) (the instantaneous frequency during stimulation reached up to 400 Hz, as the example shown in Fig. 4*B* insets) and was found both in cell-attached (*n* = 9 cells; Fig. 4*B*) and in whole-cell (*n* = 4 cells; Fig. 5*A*, *B*) recordings.

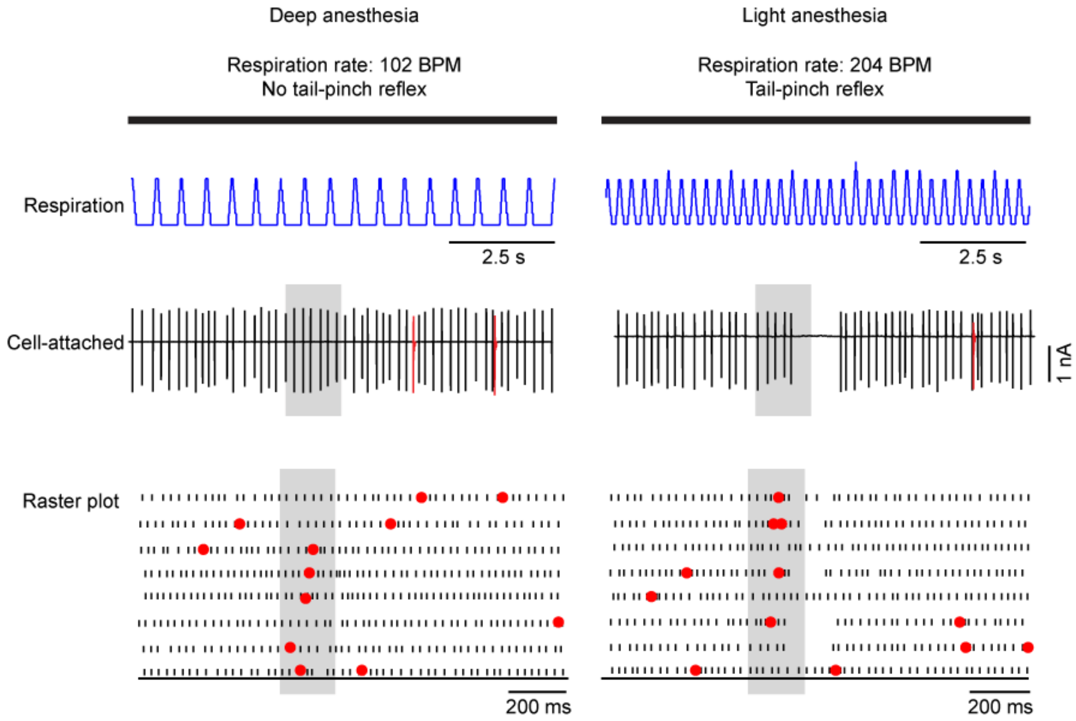

Figure 3. Dependence of whisker-evoked decrease in simple spike activity on anesthesia depth. Left panel**,** during deep anesthesia requiring the full dosage of anesthetics, as that used during dissection (see Methods and Materials), whisker stimulation failed to evoke any decrease in simple spike activity in a Purkinje neuron. Right panel**,** with light anesthesia observed under the maintenance dosage of anesthetics, whisker stimulation evoked decrease in simple spike activity in the same Purkinje neuron. Note that whisker-evoked complex spike responses were present during both deep and light anesthesia. Similar results were observed in 4 Purkinje neurons (*n* = 4 mice). Upper: traces of respiratory activity. Middle: cell-attached recordings from Purkinje cells. Lower: raster plots of simple spike (black) and complex spike (red) (8 consecutive trials).

Consistent with a primary role of GABAergic inhibition, in all of our whole-cell recordings (*n* = 6 cells), the decrease in simple spikes was accompanied by a transient hyperpolarizing deflection of the membrane potential (hyperpolarization: 6.1 ± 0.4 mV) (Fig. 2*B* and 5*A*), which is indicative of inhibitory synaptic potentials, while step-like hyperpolarizing deflection as found during state transitions [5] was triggered only by spontaneously occurring complex spikes under our conditions (Fig. 1*B*). This hyperpolarization of the membrane potential is similar as that found in slice recordings, in which a train of action potentials in an interneuron could evoke inhibitory synaptic potentials in a synaptically connected Purkinje neuron [4].

Furthermore, by hyperpolarizing the membrane potential to levels that prevented spontaneous simple spikes, we found that whisker stimulation was still able to induce simple spike firing with a clear depolarization (Fig. 5*B*, upper two traces; *n* = 4 cells). These spikes disappeared with further hyperpolarization, revealing the underlying excitatory postsynaptic potentials (EPSPs) (Fig. 5*B*, lower two traces). Because complex spikes persisted at this hyperpolarized level, we conclude that EPSPs during whisker stimulation are mediated by the activity of afferent parallel fibers. Indeed, the mean latency between these EPSPs and the onset of whisker stimulation was 53 ± 3 ms (range = 40-69 ms, *n* = 4), in well accordance with the previously reported onset latencies of whisker stimulation-granule cell activity (mean = 40 ms) [13]. Altogether, these results provide clear evidence that sensory-evoked decrease in simple spikes is mediated by synaptic inhibition.

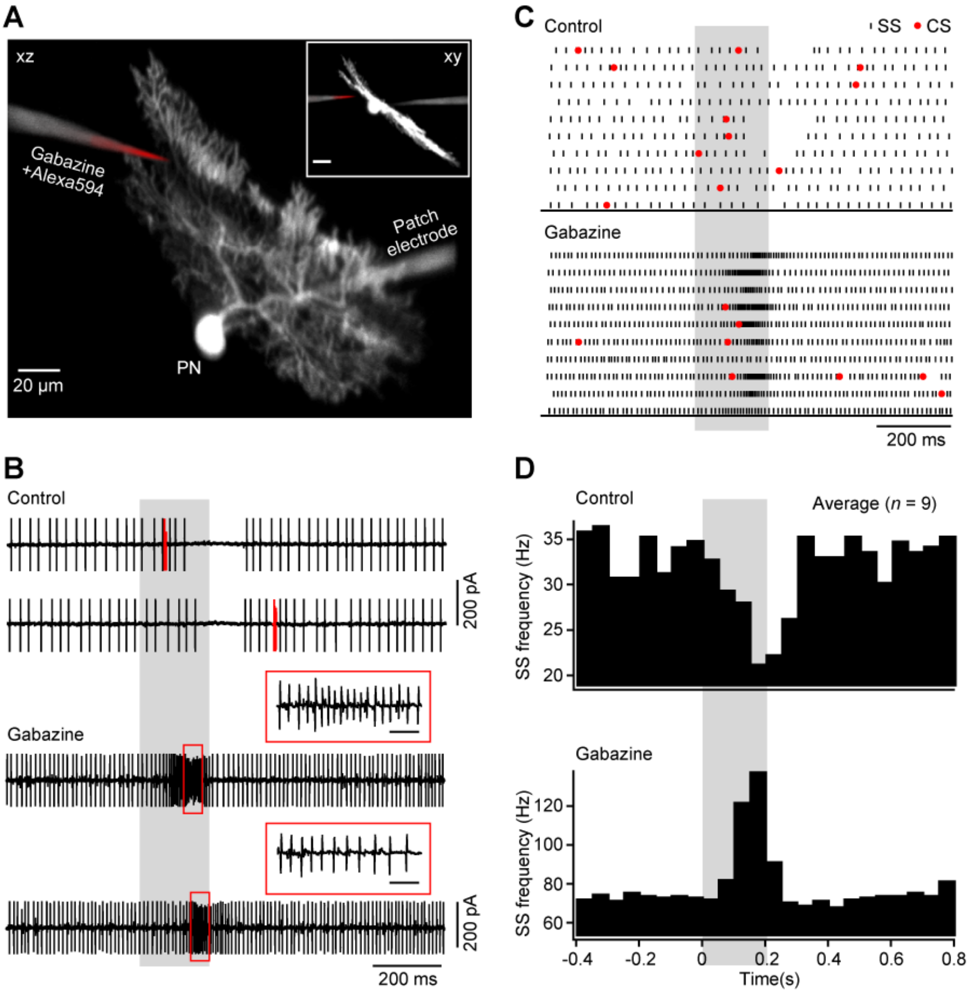

Figure 4. Synaptic inhibition mediates the sensory-evoked decrease in simple spikes in Purkinje neurons. ***A***, The xz projection image showing local drug application and patch clamp recording of an Alexa 594-labeled Purkinje neuron. The relative position of the drug pipette and the recorded cell is

shown in the *xy* projection image (inset). The tip of drug pipette filled with Alexa 594 is marked in red by pseudocolor. Scale bar: 20 µm. PN, Purkinje neuron. ***B***, Cell-attached recording showing whisker stimulation-evoked responses before (upper, two consecutive trials with spikes truncated in amplitude) and during gabazine (200 µM) application (lower, two consecutive trials with spikes truncated in amplitude) in a Purkinje neuron. Note that high-frequency simple spike firing, but not decrease, was evoked by sensory stimulation in the presence of gabazine. Insets, sensory-evoked simple spike firing in an expanded time scale (Scale bar, 10 ms). The maximum instantaneous spike frequency was 412 Hz. ***C***, Raster plot of evoked response in the absence and presence of gabazine (10 consecutive trials for each condition). Note that complex spike response was observed during stimulation in both conditions. ***D***, Averaged peristimulus histogram of simple spike (SS) frequency from 10 consecutive trials for each cell in the absence (upper) and presence of gabazine (lower) (n = 9 cells).

The inhibitory postsynaptic response in Purkinje neurons was also observed *in vivo* by electrical stimulation in molecular layer in our study (Fig. 5*C*). The whisker stimulation-evoked decrease periods had durations ranging mostly between 50 to 300 ms (mean duration = 173 ms) (Fig. 2*E*), a duration which is comparable to that of the inhibitory postsynaptic potentials (IPSPs) both *in vivo* (duration = 142 ± 32 ms with single pulse; Fig. 5*C*) and *in vitro* [41-43] by a single pulse stimulation. Another factor that could contribute to the very long decrease periods might involve transitions to the downstate triggered by molecular layer interneurons, as found in slice recordings [42,43].

Sensory stimulation evokes responses in basket cells but not in stellate cells

While it is well established that synaptic inhibition of Purkinje neurons is mediated by basket cells and stellate cells, both located in cerebellar molecular layer [2,4,19,20], the respective roles of these interneurons during sensory stimulation are unclear. We explored their possible contributions in whisker stimulation-evoked decrease in simple spike firing by performing cell-attached recordings in the same cerebellar area as used for the recordings of Purkinje neurons (the folium Crus IIa). The two types of interneurons were readily distinguished by their morphology (Fig. 6*A*, *B*), when filling them with a fluorescent dye, and by their relative position with respect to the layer of Purkinje neurons [40,44]. Briefly, the cell bodies of basket basket cells are located in the lower third of the molecular layer in the cerebellar cortex (< 50 µm from the Purkinje cell layer), while stellate cell bodies are located in the middle of the molecular layer (> 50 µm from the Purkinje cell layer). Basket cells project axons along the

Purkinje cell layer and form collaterals to the somata of Purkinje neurons, while stellate cell axons project to the dendrites. We found that whisker stimulation did not evoke any significant responses in stellate cells (n = 10) (Fig. 6*C*, *E*). By contrast, whisker stimulation reliably and effectively produced a train of spikes in basket cells, with an onset latency of 87 ± 3 ms (n = 13 cells) and an increase in mean frequency from 24 ± 3 Hz before to 81 ± 7 Hz during the stimulus (14 consecutive trials/cell; n = 13 cells) (Fig. 6*D*, *F*). This stimulus-evoked increase in output signals in basket cells probably provides the feedforward inhibition onto Purkinje neurons [4,19,20,40] and subsequently blocks the simple spikes during sensory stimulation.

Feedforward inhibition modulates the sensory-evoked responses in molecular layer interneurons

Evidence obtained from anatomical and physiological data indicates that molecular layer interneurons, in addition to projecting to Purkinje neurons, also project to interneurons [45,46]. The feed-forward inhibition onto interneurons found in slice experiments [20] might be able to modulate the sensory-evoked responses [17]. To test this possibility, we performed cell-attached recordings in stellate cells and basket cells respectively with pharmacological manipulations during whisker stimulation. As shown in Fig. 7 and 8, blocking inhibition by gabazine could increase spontaneous action potential activities in both stellate cells and basket cells. The frequency of action potentials increased from 10.8 ± 2.3 Hz to 26.1 ± 3.9 Hz in stellate cells (n = 14), and from 19.6 ± 5.6 Hz to 67.7 ± 5.5 Hz in basket cells (n = 8). This result confirms that tonic synaptic inhibition onto molecular layer interneurons exists *in vivo* and modulates their spontaneous output firing, consistent with the data from slice recordings [4].

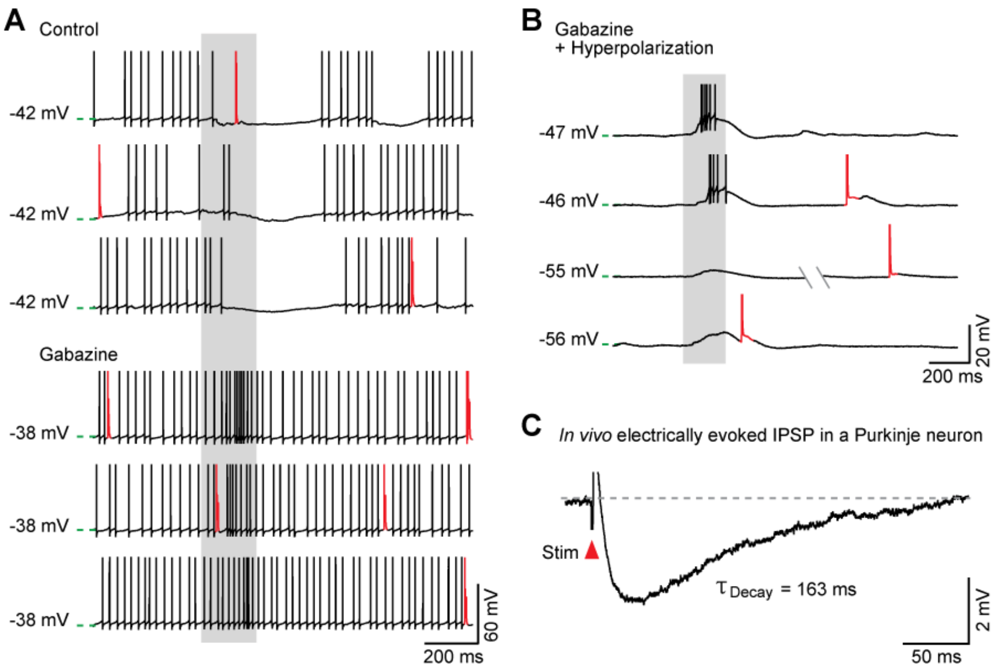

Figure 5. The contribution of synaptic inhibition in the whisker-evoked decrease in simple spikes of Purkinje neurons revealed by whole-cell patch clamp recordings. ***A***, Current-clamp recording from a Purkinje neuron showing sensory-evoked decrease in simple spike firing in control condition (upper panel, three consecutive trials) and sensory-evoked increase in simple spike firing in gabazine condition (lower panel, three consecutive trials). Red, complex spike; black, simple spike. ***B***, After preventing the spontaneous simple spike firing by negative current injection (-200 pA), sensory-evoked EPSP with a burst of spike firing was observed in the same cell as shown in panel A (upper two traces). Only EPSP was observed during stimulation if stronger negative current was injected (-400 pA) (lower two traces). In this condition, spontaneous complex spikes were still observed, marked in red. Two consecutive trials are shown for each condition, with spikes truncated in amplitude for clearer visibility of EPSPs. Similar recordings were performed in 4 Purkinje neurons. ***C***, Whole-cell recording of electrically-evoked inhibitory postsynaptic potentials (IPSPs) in Purkinje neurons *in vivo*. Representative trace of an IPSP obtained in response to electrical stimulation (1 pulse, 0.15 ms duration, 7.5 V) by an extracellular stimulation pipette that was positioned near Purkinje cell layer, about 120 µm away from the recorded neuron. The red arrowhead denotes the stimulation artefact, truncated for clarity. The value of the decay time constant τ is indicated on the figure. Similar recordings were obtained in 4 Purkinje neurons.

Intriguingly, in the presence of gabazine, whisker stimulation evoked a slight but clear increase in activity of stellate cells, which was in sharp contrast to the observation in control condition that stimulation failed to evoke any obvious response (*n* = 6 cells) (Fig. 7*A*-*C*). Moreover, in basket cells, gabazine application could enhance sensory-evoked response (Fig.

8*A*-*C*) (*n* = 5 cells). These results indicate that feedforward inhibition indeed modulates the sensory-evoked responses in both stellate cells and basket cells.

Molecular layer interneurons express both NMDA and AMPA receptors [47,48]. *In vitro* experiments have shown that AMPA receptor-mediated component is the major contributor of the evoked excitatory postsynaptic response at parallel fiber-to-interneuron synapses, while weak NMDA receptor activation appears only by strong electrical stimulation [49-51]. Therefore we next tested the contribution of AMPA receptor activation in sensory response in basket cells. As shown in Fig. 8*A*-*C*, blocking of AMPA receptors by CNQX (6-cyano-7-nitroquinoxaline-2,3-dione, the AMPA receptor antagonist) (100 μM) could effectively block sensory-evoked increase in spike response (firing frequency: 52.7 ± 7.4 Hz before stimulation, 54.5 ± 9.4 during stimulation; $P > 0.05$; *n* = 5), suggesting the major contribution of the activation of AMPA receptors. In addition, the remaining spontaneous spikes of basket cells might be due to intrinsic mechanisms, as found also in slice preparation [4]. Altogether, these results demonstrate the existence of feed-forward inhibition onto both stellate and basket cells and the activation of AMPA receptors required for the response of basket cells during sensory stimulation.

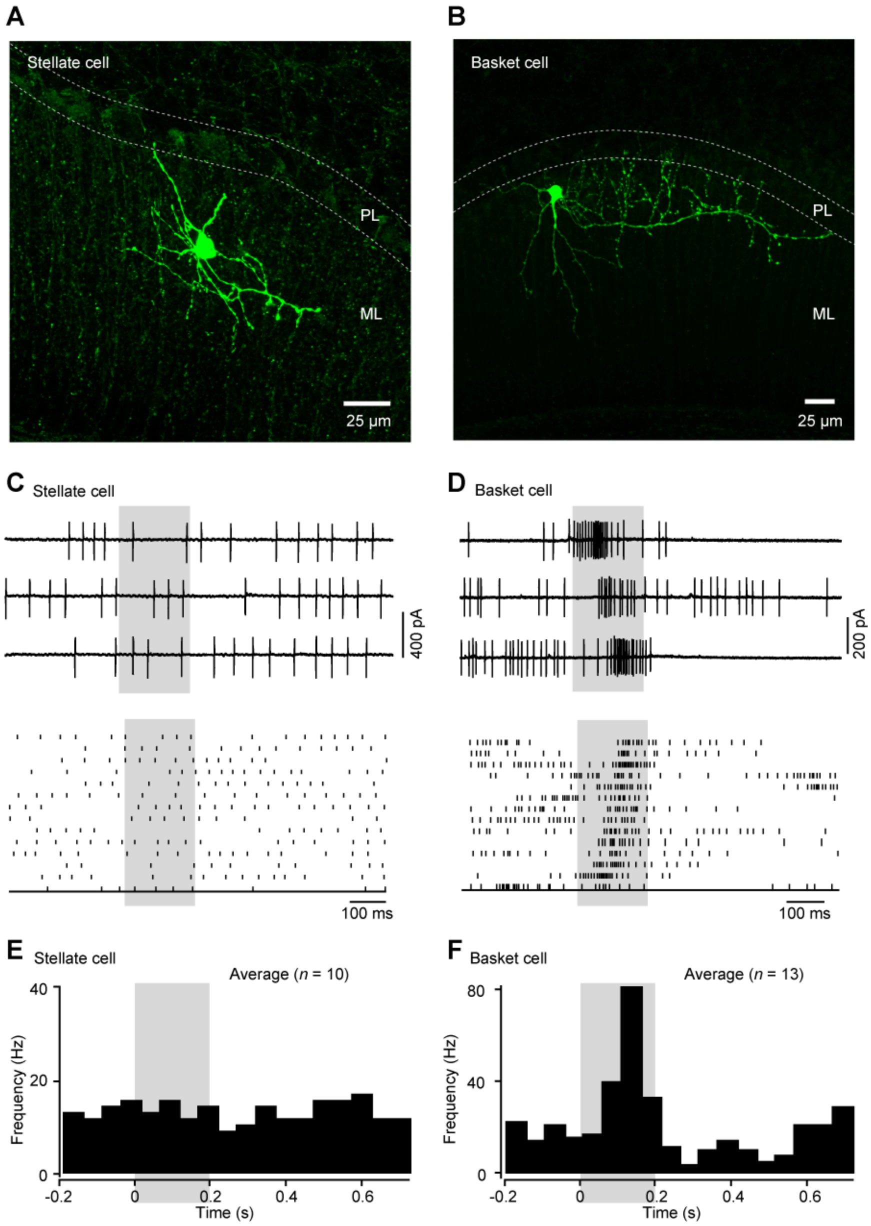

Figure 6. Whisker stimulation-evoked response in basket cells but not in stellate cells. *A* and ***B***, Morphology of a stellate cell (A) and a basket cell (B), labeled with biocytin. The images were obtained by confocal microscopy. ML, molecular layer; PL, Purkinje neuron layer. ***C***, Cell-attached recording obtained from a stellate cell. Upper, three consecutive trials; lower, raster plot of 14 consecutive trials. ***D***, Cell-attached recording obtained from a basket cell. ***E***, Averaged peristimulus histogram of spike frequency in stellate cells (14 consecutive trials for each cell; *n* = 10 cells). ***F***, Averaged peristimulus histogram of spike frequency in basket cells (14 consecutive trials for each cell; *n* = 13 cells).

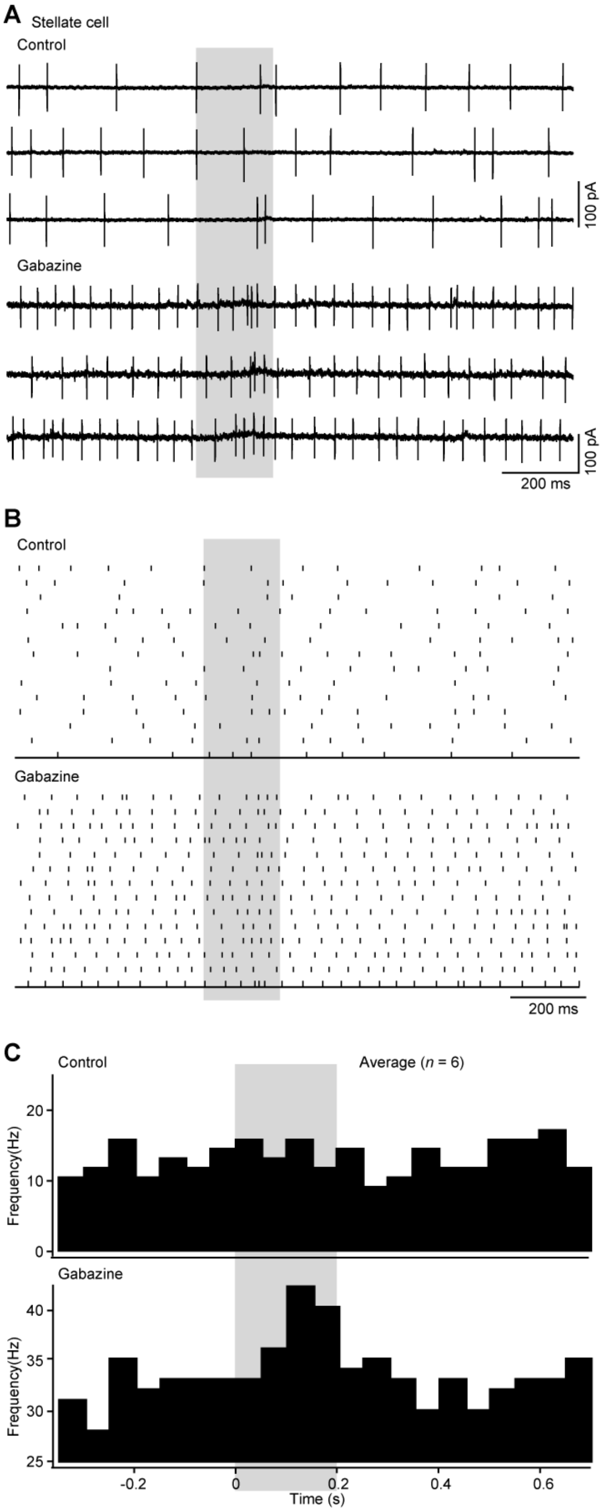

Figure 7. Whisker stimulation-evoked weak response in stellate cells after blocking inhibition. ***A***, Cell-attached recordings before (upper, three consecutive trials) and during gabazine (200 μM) application (lower, three consecutive trials). ***B***, Raster plot of spikes (14 consecutive trials for each condition). ***C***, Averaged peristimulus time histogram of spike frequency from 6 stellate cells (14 consecutive trials for each cell).

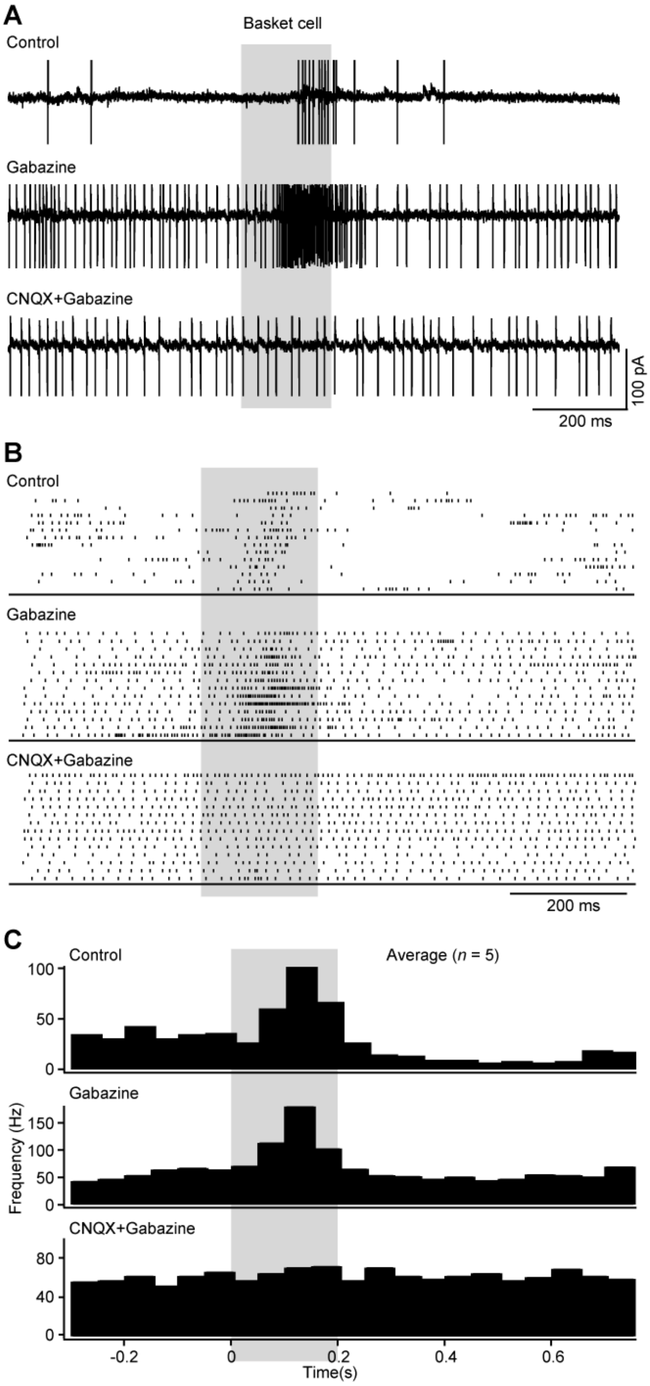

Figure 8. Whisker stimulation-evoked response in basket cells is modulated by synaptic inhibition and mainly mediated by activation of AMPA receptors. ***A***, Examples of cell-attached recordings before drug application (upper), during gabazine (200 µM) application (middle), and during gabazine (200 µM) + CNQX (100 µM) application (lower). The amplitude of spikes is truncated. ***B***, Raster plot of spikes (14 consecutive trials for each condition). ***C***, Averaged peristimulus time histogram of spike frequency for each condition (*n* = 5 cells).

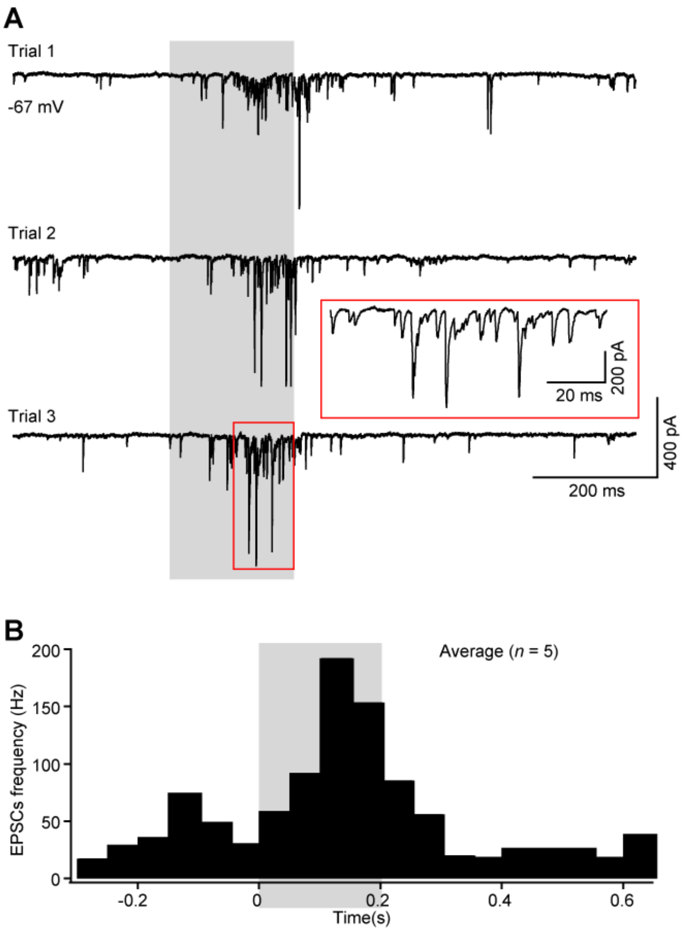

Figure 9. Whisker stimulation-evoked EPSCs in basket cells. ***A***, Voltage-clamp recording (holding potential -67 mV, a level near the reversal potential for $GABA_A$ receptor) showing sensory-evoked EPSCs in a basket cell (three consecutive trials). Inset, high-frequency EPSCs shown in an expanded scale. ***B***, Averaged peristimulus histogram of EPSC frequency (14 consecutive trials for each cell; *n* = 5).

Sensory stimulation evokes inhibitory postsynaptic currents (EPSCs) in basket cells

Sensory-evoked increase in spike firing and the blocking effect of AMPA receptor antagonist suggests the strong parallel fiber-mediated excitatory action on basket cells. To directly record these excitatory responses, we performed voltage-clamp recordings in basket cells *in vivo*. Basket cells were held at -67 mV, a level near the reversal potential for $GABA_A$ receptors in our condition. As shown clearly in Fig. 9*A* and *B*, whisker stimulation strongly induced a burst of EPSCs (latency: 86 ± 4 ms; frequency: 188 ± 16 Hz; *n* = 5), which would underlie the increase in output firing observed in basket cells during sensory stimulation.

1.1 Discussion

It has been previously found that sensory stimulation, e.g. whisker stimulation, evokes variable simple spike responses in cerebellar Purkinje neurons in both awake and anesthetized animals [5,6,9-11]. The decrease in simple spikes is one of the most common responses [5,6,9,10], which is proposed to be mediated by complex spike-evoked state transition [5] or/and by synaptic inhibition [9,18]. In this study, we utilized *in vivo* electrophysiological recordings and local pharmacological manipulations under the guidance of two-photon imaging to provide evidence that synaptic inhibition is a powerful mechanism underlying the whisker-evoked decrease in simple spikes in Purkinje neurons, in well agreement with the recent suggestion [9,18]. Furthermore, by recording molecular layer interneurons, we found that whisker stimulation produced a pronounced excitatory response in basket cells but not in stellate cells. This suggests that basket cells represent a possible source of feedforward inhibition responsible for the sensory-evoked decrease in simple spikes of their postsynaptic Purkinje neurons.

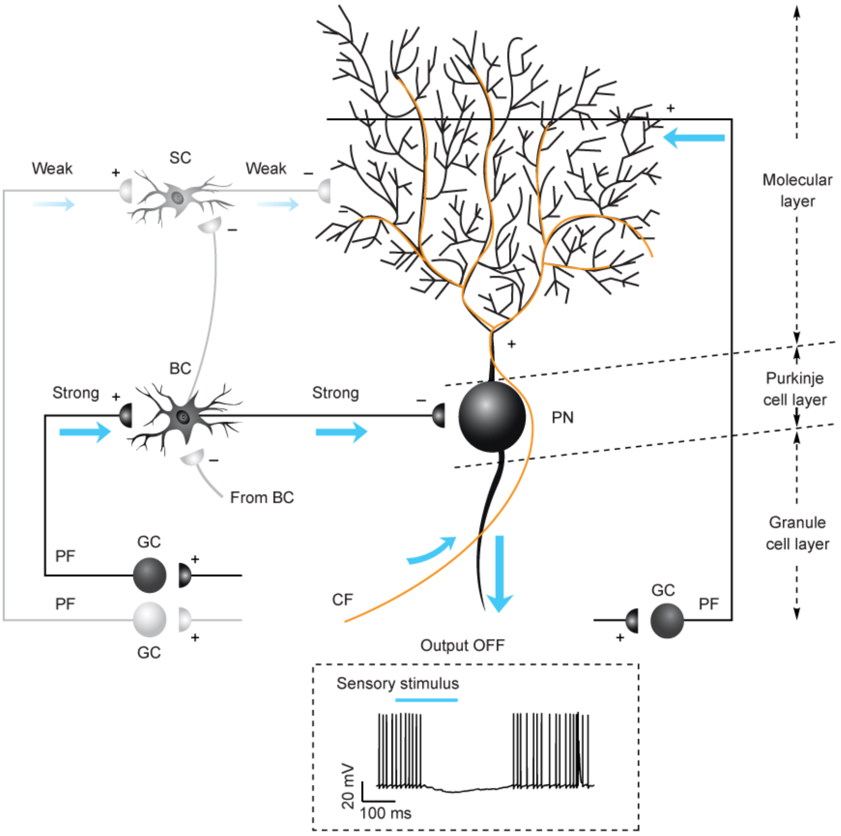

Figure 10. Model of sensory-evoked signal flow through cerebellar cortical circuitry. PF, parallel fiber; CF, climbing fiber; SC, stellate cell; BC, basket cell; PN, Purkinje neuron; GC, granule cell; Blue arrow, direction of sensory transmission; +, synaptic excitation; -, synaptic inhibition.

Feedforward inhibition provided by local interneurons is a ubiquitous phenomenon existing in many brain circuits, such as the cerebellar cortex [20], the lateral geniculate nucleus of the thalamus [52], the neocortex [53,54], the hippocampus [2], and the brain stem [55]. Feedforward inhibition is involved in multiple physiological functions, including the modulation of the temporal integration of neuronal activity [20,56,57], the control of the neuronal input-output relation [58], and the regulation of visually evoked response [52,59] and sensory cortical receptive fields [60]. In the cerebellar cortex, feedforward inhibition results from molecular layer basket cells and stellate cells, which are activated by the same inputs of parallel fibers as their target Purkinje neurons [20,61]. In addition to the feedforward inhibition onto Purkinje neurons, previous *in vitro* experiments have also found the existence of this inhibition in cerebellar interneurons [20]. Feedforward inhibition is considered to have important roles in the cerebellar function *in vivo* [19,62]. In this study, we found the contributions of feedforward inhibition in all the three types of neurons during sensory stimulation in the cerebellar cortex. In the Purkinje neurons, feedforward inhibition results in hyperpolarization of the membrane potential rather than just terminate the membrane depolarization activated by parallel fiber inputs [20,63], thereby leading to a blockage of simple spike activity during sensory processing. Interestingly, in the basket cells, feedforward inhibition only has a weak effect on the spike activity and the cells still exhibit a clear increase in spike output during sensory stimulation as the cells exhibit a relatively strong parallel fiber-mediated excitatory response. The weak effect of inhibition in interneurons has been also found in slice preparation [20]. Finally, in the stellate cells, feedforward inhibition and parallel fiber-mediated excitation seems equally weak, which would explain the fact that we failed to observe any obvious sensory response. The observation of strong parallel fiber-mediated excitation in basket cells but weak excitation in stellate cells is most likely due to the different amount of distributed parallel fiber synapses, as found by the morphological data in mouse cerebellum that basket cells (located in the depth lower than 50 µm) receive more parallel fiber synapses than stellate cells (located in the 50 µm upper layer) [64]. Taken together, basket cell-mediated feedforward inhibition is found to function in the circuitry of the cerebellar cortex to modulate parallel fiber inputs to both interneurons and Purkinje neurons during sensory stimulation, thereby endowing this well-established phenomenon with a new physiological significance that is involved in sensory processing in the cerebellum.

Our findings identify a mechanism underlying the whisker stimulation-evoked decrease in the output signals of cerebellar cortex. The emerging working model for sensory information processing in the cerebellar cortical microcircuitry is illustrated in Fig. 10. In brief, two distinct pathways send sensory information to the cerebellum: first, the climbing fibers originating in the inferior olivary nucleus in the brain stem and, second, the mossy fiber-granule cell-parallel fiber pathway originating primarily in the pontine nucleus [2]. The critical new information revealed by this study is that within the cerebellar cortical microcircuitry, the parallel fibers carrying sensory information excite both Purkinje neurons and molecular layer interneurons. During whisker stimulation, synaptic inhibitory action from basket cells, but not stellate cells, competes with the parallel fibers-mediated excitatory force in Purkinje neurons, and succeeds in turning off the neuronal output of the cerebellar cortex. It should be noted that this signal flow is induced by the movement of the whiskers. By contrast, during other behaviors, like vestibular stimulation, both basket cells and stellate cells are engaged in the inhibition of Purkinje neurons [19]. This suggests the diversity of the contributions of molecular layer interneurons in different cerebellar functions *in vivo*.

By establishing decrease in the output signals in Purkinje neurons as the critical outcome of whisker-evoked sensory processing in the cerebellar cortex, we provide a mechanism for previous observations of a long-latency increase in spiking activity in deep cerebellar nuclei, the target of the inhibitory Purkinje neurons, with response properties (latency > 100 ms, duration >100 ms) matching our observation in Purkinje neurons [41,65]. Therefore, the decrease in spike activity in Purkinje neurons and the resulting increase in a subset of deep cerebellar neurons may represent one pattern of signal flows and play a functional role in the integration of sensory information in the cerebellum. For future studies, it will be very interesting to investigate whether the manipulation that induces this type of signal flow in specific areas of cerebellum, e.g. targeted optogenetic stimulation [62] of basket cells, would modulate certain related movements.

The results from us and others [6,9,11] have found that whisker stimulation-evoked simple spike responses are quite variable in Purkinje neurons even in a small area of the cerebellar cortex. Similarly, both excitatory receptive fields and inhibitory receptive fields were reported in the tactile areas in an early study [10]. Given that we find the major contribution of basket cells in the modulation of this sensory response, this variation is probably due to the spatial distribution of basket cells in the cerebellar cortex. For example, the density of basket cells may be higher in the region, in which Purkinje neurons exhibit sensory-evoked decrease in spike activity. However, this hypothesis needs further careful investigation. In addition, in the subset of Purkinje neurons as we tested, sensory stimulation can evoke both complex spike response and high frequency of simple spikes after blocking inhibition. As the co-activation of climbing and parallel fibers is the prerequisite for long-term depression at the parallel fiber-Purkinje neuron synapses [66], these sensory-evoked coincident responses detected by individual Purkinje neurons provides a potential cellular substrate for cerebellar learning during sensory processing [2]. Despite basket cells strongly affect the output signals of Purkinje neurons via axons innervating the somata [44], it is possible that the long-term plasticity may occur at the dendritic level in this subset of Purkinje neurons.

References

1 Apps, R. & Garwicz, M. Anatomical and physiological foundations of cerebellar information processing. *Nat Rev Neurosci* 6, 297-311 (2005).

2 Buzsáki, G. Feed-forward inhibition in the hippocampal formation. *Prog Neurobiol* 22, 131-153 (1984).

3 Murphy, J. T. & Sabah, N. H. Spontaneous firing of cerebellar Purkinje cells in decerebrate and barbiturate anesthetized cats. *Brain Res* 17, 515-519 (1970).

4 Häusser, M. & Clark, B. A. Tonic synaptic inhibition modulates neuronal output pattern and spatiotemporal synaptic integration. *Neuron* 19, 665-678 (1997).

5 Loewenstein, Y. *et al.* Bistability of cerebellar Purkinje cells modulated by sensory stimulation. *Nat. Neurosci.* 8, 202-211 (2005).

6 Brown, I. E. & Bower, J. M. Congruence of mossy fiber and climbing fiber tactile projections in the lateral hemispheres of the rat cerebellum. *J. Comp. Neurol.* 429, 59-70 (2001).

7 Schultz, S. R., Kitamura, K., Post-Uiterweer, A., Krupic, J. & Häusser, M. Spatial pattern coding of sensory information by climbing fiber-evoked calcium signals in networks of neighboring cerebellar Purkinje cells. *J. Neurosci.* 29, 8005-8015 (2009).

8 Ozden, I., Sullivan, M. R., Lee, H. M. & Wang, S. S. Reliable coding emerges from coactivation of climbing fibers in microbands of cerebellar Purkinje neurons. *J Neurosci* 29, 10463-10473 (2009).

9 Bosman, L. W. *et al.* Encoding of whisker input by cerebellar Purkinje cells. *J Physiol* 588, 3757-3783 (2010).

10 Bower, J. M. & Woolston, D. C. Congruence of spatial organization of tactile projections to granule cell and Purkinje cell layers of cerebellar hemispheres of the albino rat: vertical organization of cerebellar cortex. *J Neurophysiol* 49, 745-766 (1983).

11 Holtzman, T., Rajapaksa, T., Mostofi, A. & Edgley, S. A. Different responses of rat cerebellar Purkinje cells and Golgi cells evoked by widespread convergent sensory inputs. *J Physiol* 574, 491-507 (2006).

12 Rancz, E. A. *et al.* High-fidelity transmission of sensory information by single cerebellar mossy fibre boutons. *Nature* 450, 1245-1248 (2007).

13 Chadderton, P., Margrie, T. W. & Häusser, M. Integration of quanta in cerebellar granule cells during sensory processing. *Nature* 428, 856-860 (2004).

14 Barmack, N. H. & Yakhnitsa, V. Cerebellar climbing fibers modulate simple spikes in Purkinje cells. *J Neurosci* 23, 7904-7916 (2003).

15 Demer, J. L., Echelman, D. A. & Robinson, D. A. Effects of electrical stimulation and reversible lesions of the olivocerebellar pathway on Purkinje cell activity in the flocculus of the cat. *Brain Res* 346, 22-31 (1985).

16 Cerminara, N. L. & Rawson, J. A. Evidence that climbing fibers control an intrinsic spike generator in cerebellar Purkinje cells. *J Neurosci* 24, 4510-4517 (2004).

17 Santamaria, F., Tripp, P. G. & Bower, J. M. Feedforward inhibition controls the spread of granule cell-induced Purkinje cell activity in the cerebellar cortex. *J Neurophysiol* 97, 248-263 (2007).

18 Chu, C. P., Bing, Y. H. & Qiu, D. L. Sensory stimulus evokes inhibition rather than excitation in cerebellar Purkinje cells in vivo in mice. *Neurosci Lett* 487, 182-186 (2011).

19 Barmack, N. H. & Yakhnitsa, V. Functions of interneurons in mouse cerebellum. *J. Neurosci.* 28, 1140-1152 (2008).

20 Mittmann, W., Koch, U. & Häusser, M. Feed-forward inhibition shapes the spike output of cerebellar Purkinje cells. *J. Physiol.* 563, 369-378 (2005).

21 Rochefort, N. L. *et al.* Sparsification of neuronal activity in the visual cortex at eye-opening. *Proc Natl Acad Sci U S A* 106, 15049-15054 (2009).

22 Stosiek, C., Garaschuk, O., Holthoff, K. & Konnerth, A. In vivo two-photon calcium imaging of neuronal networks. *Proc. Natl. Acad. Sci. USA* 100, 7319-7324 (2003).

23 Chen, X. *et al.* Disruption of the olivo-cerebellar circuit by Purkinje neuron-specific ablation of BK channels. *Proc Natl Acad Sci U S A* 107, 12323-12328 (2010).

24 Hofer, S. B., Mrsic-Flogel, T. D., Bonhoeffer, T. & Hübener, M. Prior experience enhances plasticity in adult visual cortex. *Nat. Neurosci.* 9, 127-132 (2006).

25 Ozden, S. & Isenmann, S. Neuroprotective properties of different anesthetics on axotomized rat retinal ganglion cells in vivo. *J. Neurotrauma.* 21, 73-82 (2004).

26 Wixson, S. K., White, W. J., Hughes, H. C., Jr., Lang, C. M. & Marshall, W. K. A comparison of pentobarbital, fentanyl-droperidol, ketamine-xylazine and ketamine-diazepam anesthesia in adult male rats. *Lab. Anim. Sci.* 37, 726-730 (1987).

27 Hoffmann, S., Schuller, G. & Firzlaff, U. Dynamic stimulation evokes spatially focused receptive fields in bat auditory cortex. *Eur J Neurosci* 31, 371-385 (2010).

28 Firzlaff, U., Schuchmann, M., Grunwald, J. E., Schuller, G. & Wiegrebe, L. Object-oriented echo perception and cortical representation in echolocating bats. *PLoS Biol* 5, e100 (2007).

29 Ozden, I., Lee, H. M., Sullivan, M. R. & Wang, S. S. Identification and clustering of event patterns from in vivo multiphoton optical recordings of neuronal ensembles. *J. Neurophysiol.* 100, 495-503 (2008).

30 Bennett, F. M. & Tenney, S. M. Comparative mechanics of mammalian respiratory system. *Respir. Physiol.* 49, 131-140 (1982).

31 Irvin, C. G. & Bates, J. H. Measuring the lung function in the mouse: the challenge of size. *Respir. Res.* 4, 4 (2003).

32 Leybaert, L., de Meyer, A., Mabilde, C. & Sanderson, M. J. A simple and practical method to acquire geometrically correct images with resonant scanning-based line scanning in a custom-built video-rate laser scanning microscope. *J. Microsc.* 219, 133-140 (2005).

33 Kitamura, K., Judkewitz, B., Kano, M., Denk, W. & Häusser, M. Targeted patch-clamp recordings and single-cell electroporation of unlabeled neurons in vivo. *Nat. Methods* 5, 61-67 (2008).

34 Judkewitz, B., Rizzi, M., Kitamura, K. & Häusser, M. Targeted single-cell electroporation of mammalian neurons in vivo. *Nat. Protoc.* 4, 862-869 (2009).

35 Jia, H., Rochefort, N. L., Chen, X. & Konnerth, A. Dendritic organization of sensory input to cortical neurons in vivo. *Nature* 464, 1307-1312 (2010).

36 Williams, S. R., Christensen, S. R., Stuart, G. J. & Häusser, M. Membrane potential bistability is controlled by the hyperpolarization-activated current I(H) in rat cerebellar Purkinje neurons in vitro. *J Physiol* 539, 469-483 (2002).

37 Yartsev, M. M., Givon-Mayo, R., Maller, M. & Donchin, O. Pausing purkinje cells in the cerebellum of the awake cat. *Front. Syst. Neurosci.* 3, 2 (2009).

38 Schonewille, M. *et al.* Purkinje cells in awake behaving animals operate at the upstate membrane potential. *Nat. Neurosci.* 9, 459-461; author reply 461 (2006).

39 Fontanini, A. & Katz, D. B. Behavioral states, network states, and sensory response variability. *J Neurophysiol* 100, 1160-1168 (2008).

40 Ito, M. *The cerebellum and neural control*. (Raven Press, 1984).

41 Callaway, J. C., Lasser-Ross, N. & Ross, W. N. IPSPs strongly inhibit climbing fiber-activated [Ca2+]i increases in the dendrites of cerebellar Purkinje neurons. *J Neurosci* 15, 2777-2787 (1995).

42 Oldfield, C. S., Marty, A. & Stell, B. M. Interneurons of the cerebellar cortex toggle Purkinje cells between up and down states. *Proc Natl Acad Sci U S A* 107, 13153-13158 (2010).

43 Jacobson, G. A., Rokni, D. & Yarom, Y. A model of the olivo-cerebellar system as a temporal pattern generator. *Trends Neurosci.* 31, 617-625 (2008).

44 Palay, S. L. & Chan-Palay, v. *Cerebellar cortex: cytology and organization*. (Springer, 1974).

45 Pouzat, C. & Hestrin, S. Developmental regulation of basket/stellate cell-->Purkinje cell synapses in the cerebellum. *J Neurosci* 17, 9104-9112 (1997).

46 Sultan, F. & Bower, J. M. Quantitative Golgi study of the rat cerebellar molecular layer interneurons using principal component analysis. *J Comp Neurol* 393, 353-373 (1998).

47 Liu, S. Q. & Cull-Candy, S. G. Synaptic activity at calcium-permeable AMPA receptors induces a switch in receptor subtype. *Nature* 405, 454-458 (2000).

48 Cull-Candy, S. G. *et al.* NMDA receptor diversity in the cerebellum: identification of subunits contributing to functional receptors. *Neuropharmacology* 37, 1369-1380 (1998).

49 Clark, B. A. & Cull-Candy, S. G. Activity-dependent recruitment of extrasynaptic NMDA receptor activation at an AMPA receptor-only synapse. *J Neurosci* 22, 4428-4436 (2002).

50 Glitsch, M. & Marty, A. Presynaptic effects of NMDA in cerebellar Purkinje cells and interneurons. *J Neurosci* 19, 511-519 (1999).

51 Carter, A. G. & Regehr, W. G. Prolonged synaptic currents and glutamate spillover at the parallel fiber to stellate cell synapse. *J Neurosci* 20, 4423-4434 (2000).

52 Blitz, D. M. & Regehr, W. G. Timing and specificity of feed-forward inhibition within the LGN. *Neuron* 45, 917-928 (2005).

53 Gupta, A., Wang, Y. & Markram, H. Organizing principles for a diversity of GABAergic interneurons and synapses in the neocortex. *Science* 287, 273-278 (2000).

54 Tierney, P. L., Thierry, A. M., Glowinski, J., Deniau, J. M. & Gioanni, Y. Dopamine modulates temporal dynamics of feedforward inhibition in rat prefrontal cortex in vivo. *Cereb Cortex* 18, 2251-2262 (2008).

55 Roberts, M. T. & Trussell, L. O. Molecular layer inhibitory interneurons provide feedforward and lateral inhibition in the dorsal cochlear nucleus. *J Neurophysiol* 104, 2462-2473 (2010).

56 Pouille, F. & Scanziani, M. Enforcement of temporal fidelity in pyramidal cells by somatic feed-forward inhibition. *Science* 293, 1159-1163 (2001).

57 Assisi, C., Stopfer, M., Laurent, G. & Bazhenov, M. Adaptive regulation of sparseness by feedforward inhibition. *Nat Neurosci* 10, 1176-1184 (2007).

58 Ferrante, M., Migliore, M. & Ascoli, G. A. Feed-forward inhibition as a buffer of the neuronal input-output relation. *Proc Natl Acad Sci U S A* 106, 18004-18009 (2009).

59 Hu, B., Li, X., Zhou, Y. & Shou, T. Effects of bicuculline on direction-sensitive relay cells in the dorsal lateral geniculate nucleus (LGNd) of cats. *Brain Res* 885, 87-93 (2000).

60 Swadlow, H. A. Thalamocortical control of feed-forward inhibition in awake somatosensory 'barrel' cortex. *Philos Trans R Soc Lond B Biol Sci* 357, 1717-1727 (2002).

61 Eccles, J. C., Ito, M. & Szentagothai, J. *The Cerebellumas a Neuronal Machine*. (Springer-Verlag, 1967).

62 Wulff, P. *et al.* Synaptic inhibition of Purkinje cells mediates consolidation of vestibulo-cerebellar motor learning. *Nat. Neurosci.* 12, 1042-1049 (2009).

63 Bao, J., Reim, K. & Sakaba, T. Target-dependent feedforward inhibition mediated by short-term synaptic plasticity in the cerebellum. *J Neurosci* 30, 8171-8179 (2010).

64 Lemkey-Johnston, N. & Larramendi, L. M. Types and distribution of synapses upon basket and stellate cells of the mouse cerebellum: an electron microscopic study. *J Comp Neurol* 134, 73-112 (1968).

65 Rowland, N. C. & Jaeger, D. Coding of tactile response properties in the rat deep cerebellar nuclei. *J. Neurophysiol.* 94, 1236-1251 (2005).

66 Ito, M., Sakurai, M. & Tongroach, P. Climbing fibre induced depression of both mossy fibre responsiveness and glutamate sensitivity of cerebellar Purkinje cells. *J. Physiol.* 324, 113-134 (1982).

Project III

Dendritic organization of sensory input to cortical neurons *in vivo*

(Published in **Nature**, 2010, 464: 1307-12)

Vol 464 | 29 April 2010 | doi:10.1038/nature08947 nature

ARTICLES

Dendritic organization of sensory input to cortical neurons *in vivo*

Hongbo Jia[1]*, Nathalie L. Rochefort[1]*, Xiaowei Chen[1] & Arthur Konnerth[1]

In sensory cortex regions, neurons are tuned to specific stimulus features. For example, in the visual cortex, many neurons fire predominantly in response to moving objects of a preferred orientation. However, the characteristics of the synaptic input that cortical neurons receive to generate their output firing pattern remain unclear. Here we report a novel approach for the visualization and functional mapping of sensory inputs to the dendrites of cortical neurons *in vivo*. By combining high-speed two-photon imaging with electrophysiological recordings, we identify local subthreshold calcium signals that correspond to orientation-specific synaptic inputs. We find that even inputs that share the same orientation preference are widely distributed throughout the dendritic tree. At the same time, inputs of different orientation preference are interspersed, so that adjacent dendritic segments are tuned to distinct orientations. Thus, orientation-tuned neurons can compute their characteristic firing pattern by integrating spatially distributed synaptic inputs coding for multiple stimulus orientations.

A growing amount of evidence indicates that information processing in the brain involves the computation of electrical and chemical signals in neuronal dendrites (for a review, see ref. 1). One of the most effective ways for the analysis of these dendritic signals relies on the imaging of the dynamics of intracellular Ca^{2+} concentration (reviewed in ref. 2). Thus, synaptic input-related dendritic Ca^{2+} transients have been identified and studied in detail *in vitro*[3–6], while *in vivo* work has explored action-potential-related dendritic Ca^{2+} signals[7–9]. However, nothing is known about the nature of subthreshold sensory evoked input signals in the dendrites of mammalian cortical neurons. A detailed knowledge of sensory input signals would represent an important step forward in the understanding of dendritic computation[1,10–13]. An intriguing open question is whether sensory inputs with similar features are clustered on the same dendrite of a neuron or dispersed throughout the dendritic tree. Clustered inputs are capable of generating dendritic spikes (reviewed in ref. 11) and may form neuronal computational subunits *in vivo*, as they do under certain experimental conditions *in vitro*[14]. Alternatively, sensory inputs that are not clustered, but widely distributed, may underlie different rules of integration and formation of neuronal output signals—like, for example, the linear summation of excitatory inputs[15].

Visually evoked supra- and subthreshold activity

For the functional analysis of spiny dendrites *in vivo* by means of two-photon calcium imaging, we selected as an experimental model neurons in layer 2/3 of the mouse primary visual cortex (Fig. 1a–c). The somata of the neurons were located approximately between 140 and 200 μm below the cortical surface. Their dendritic trees had a characteristic pattern, consisting of numerous basal and oblique dendrites but no pronounced apical trunk[16–18] (Fig. 1a). As in many other mammalian species[19–21], layer 2/3 neurons of the mouse primary visual cortex respond selectively to drifting gratings or bars with action potential firing[22–24]. By performing whole-cell recordings involving the 'shadow-patching' approach[25], we found that stimulation with drifting gratings shifted the membrane potential to the 'up-state'[26] for the entire duration of the stimulus. An increased probability of up-states during drifting grating stimulation was previously observed in the cat visual cortex[27]. The neuron illustrated in Fig. 1d fired action potentials preferentially during the presentation of specifically oriented drifting gratings and was identified as a 'highly-tuned' neuron (Fig. 1e left) on the basis of its orientation selectivity index (OSI), which was higher than 0.5 (Methods). In our recordings, 6 out of 17 neurons were highly tuned for a preferred orientation (Fig. 1f left), 6/17 neurons were poorly tuned, while the rest of 5/17 neurons did not respond reliably to visual stimulation. For a better assessment of the stimulus-evoked subthreshold depolarization in highly tuned neurons, we hyperpolarized them to subthreshold membrane potentials. In the example shown in Fig. 1d, the neuron was hyperpolarized from its resting level of −64 mV to −70 mV. In contrast to the highly tuned action potential pattern (Fig. 1e left), the stimulus-evoked subthreshold depolarizing responses were broadly tuned in this (Fig. 1e right) as well as in all other highly tuned neurons (Fig. 1f right). Thus, in mouse visual cortex, as in cat visual cortex[28,29], the high tuning level of action potential firing, the neuronal output signal, contrasts with the low tuning level of the afferent subthreshold input signals.

These observations prompted us to combine whole-cell recordings with two-photon calcium imaging to search for dendritic signals associated with the afferent activity. We performed high-speed two-photon imaging at 30 full frames per second or 60 half frames per second using resonant galvo-scanners[30] and, initially, focused on the dendrites that were visible in the plane of focus containing the cell body (Fig. 1g). When stimulated with their preferred orientation, neurons responded with action potential firing that was associated with global dendritic calcium transients in all imaged dendrites. In the neuron illustrated in Fig. 1g, all five visible dendrites displayed calcium transients that were larger when the neuron fired four action potentials (Fig. 1h left) than when it fired two action potentials (Fig. 1h right). The dependence of the calcium transient amplitude on the number of action potentials and the observation that similar calcium transients were evoked by direct neuronal depolarization through the recording pipette (Supplementary Fig. 1a–c) indicate

---

[1] Institute of Neuroscience and Center for Integrated Protein Science, Technical University Munich, Biedersteinerstrasse 29, 80802 Munich, Germany.

*These authors contributed equally to this work.

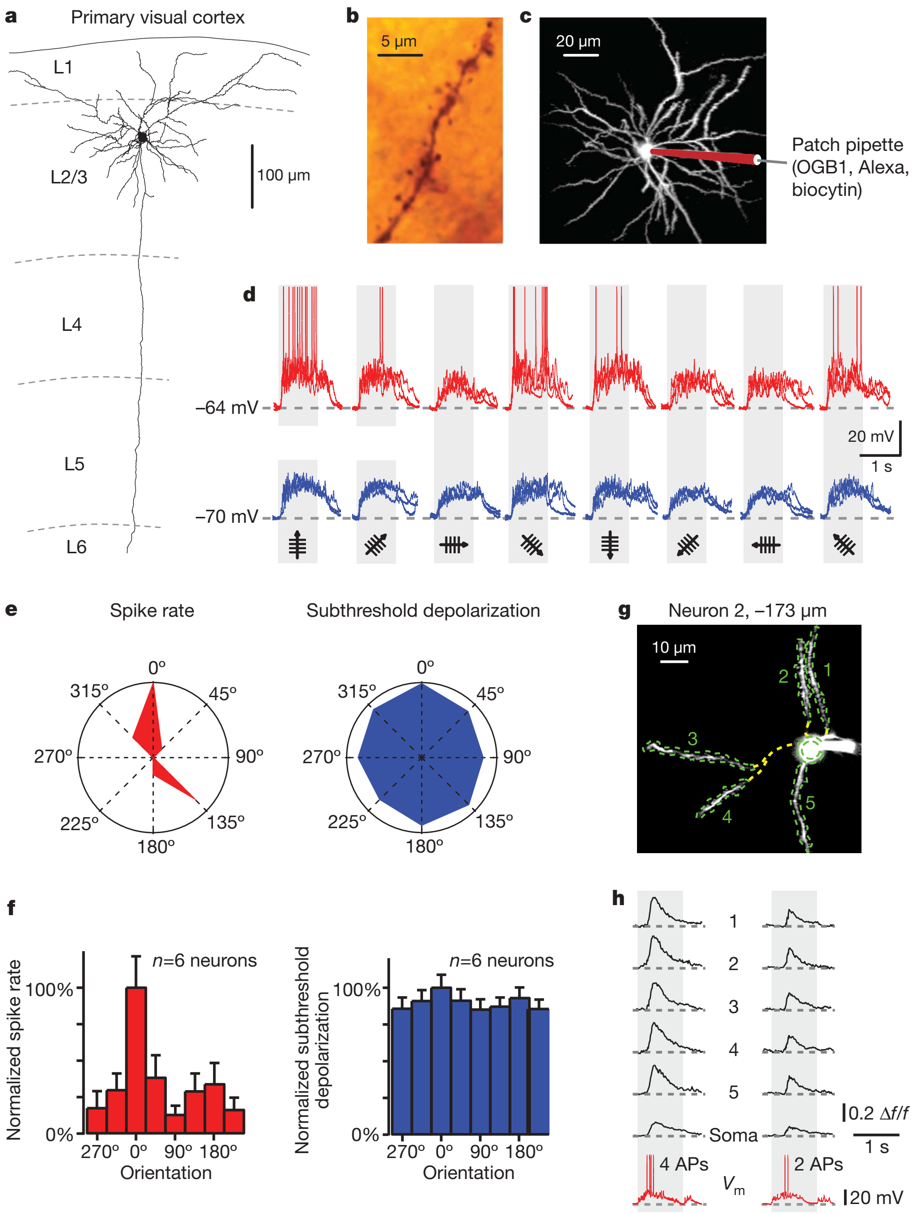

Figure 1 | Visually evoked action potentials, subthreshold depolarizations and global dendritic calcium signals. **a**, Reconstruction of a biocytin-filled layer 2/3 (L2/3) neuron in mouse primary visual cortex (projection along the antero-posterior axis). Data from the same neuron are presented in **b**–**e**. **b**, Microphotograph of a spiny basal dendrite. **c**, Projection along the dorso-ventral axis obtained *in vivo* from 469 sections (step size 0.5 µm) from Alexa fluorescence. **d**, Whole-cell current-clamp recordings of responses to drifting gratings of different orientations. Three trials were superimposed. Upper red traces, action potential responses at resting potential (indicated on the left); lower blue traces, subthreshold responses obtained after hyperpolarizing the neuron to −70 mV. **e**, Polar plots of visually evoked responses, average of eight trials. Red plot, spike rate; blue plot, amplitude of subthreshold depolarization. **f**, Tuning properties of spiking and subthreshold responses for six orientation-selective neurons, each normalized to their preferred orientation (noted as 0°). Error bars, +s.d. **g**, **h**, Two-photon imaging of dendritic calcium signals in basal and oblique dendrites of another layer 2/3 neuron during action potential firing (electrical recording lower red trace) evoked by drifting gratings. **g**, Average image of 100 frames recorded at 173 µm below the cortical surface. Yellow dashed lines indicate out-of-focus portions of the dendrites. Green dashed lines indicate the regions of interest (ROIs). **h**, Ca^{2+}-dependent fluorescence changes (black traces) recorded in the soma and in five dendrites (indicated by numbers in **g**) and the corresponding membrane potential (V_m, red traces) recordings, during two separate trials. Light grey bars indicate the stimulation period with oriented gratings. AP, action potential.

that such global dendritic signals are largely due to the activation of voltage-gated calcium channels by back-propagating action potentials; this has previously been shown for basal dendrites in *in vitro* recordings from layer 2/3 neurons[31,32]. The amplitude of the Ca^{2+} transients at different dendritic sites showed attenuation along a given dendrite (Supplementary Fig. 1d, e) and variations from trial to trial, but we were unable to obtain unambiguous evidence for signal peaks that would correspond to specific synaptic inputs, as found in tectal neurons of the tadpole[33]. Therefore, we decided to search for calcium signals associated with subthreshold synaptic calcium signalling in conditions in which we actively hyperpolarized the neurons.

Subthreshold calcium signals in dendritic hotspots

Figure 2 illustrates the results of an experiment in which a neuron was hyperpolarized to −70 mV to prevent action potential firing. In these conditions, a calcium transient was evoked in a subregion of 'dendrite 3' (Fig. 2a, b) by visual stimulation (drifting grating), but not detected in the other dendrites or in the soma. To assess the spatial dimensions of such local calcium transients, we analysed experiments

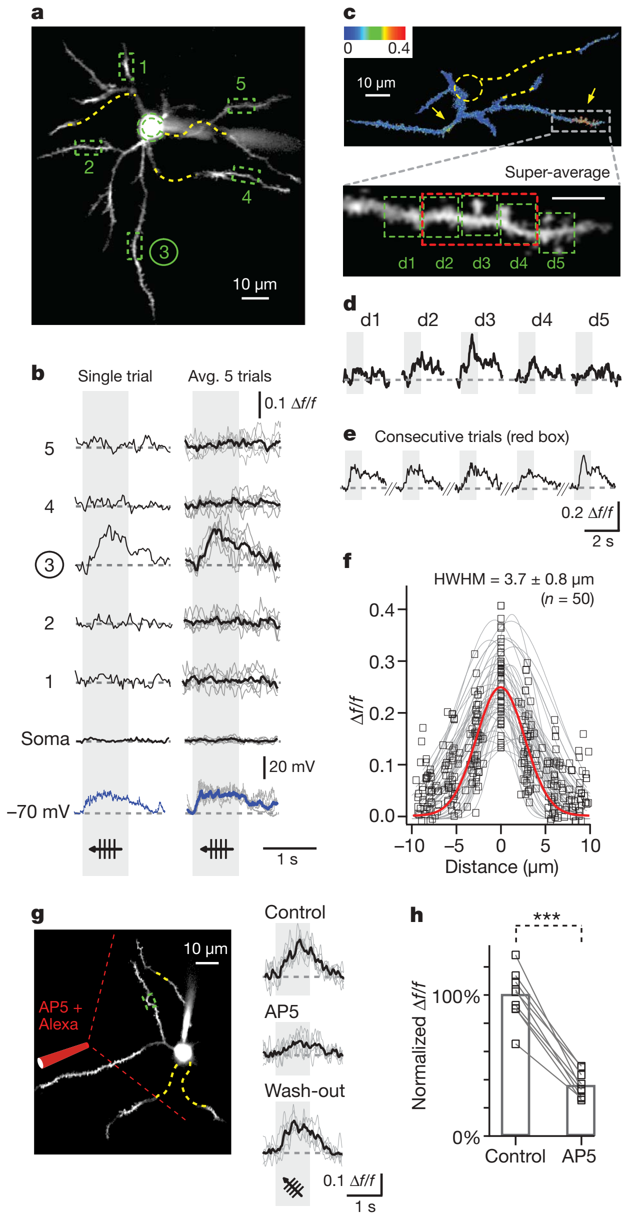

Figure 2 | Subthreshold local dendritic calcium signals evoked by drifting grating stimulation. **a**, Two-photon image used for calcium recordings in **b**. The image is an average of 100 frames. Five ROIs are indicated by green dashed rectangles. **b**, Subthreshold Ca^{2+} transients (black traces) and corresponding depolarization (blue traces) evoked by drifting grating stimulation. Note the prominent Ca^{2+} signal in dendrite 3. Left traces, single trials; right traces, average (black trace) of five individual trials (grey traces) from various dendritic sites and soma, as indicated. **c**, Upper panel, pseudo-colour image of local dendritic Ca^{2+} signals. Ratio of the averages of 30 frames before and 30 frames during stimulation. Yellow arrows indicate two sites of local dendritic calcium signals. Lower panel, enlarged view of the dashed box indicated in the upper image, 'super-average' obtained from 500 frames. **d**, Calcium recordings from five neighbouring dendritic regions of 3 μm length (d1–d5, ROIs shown in **c**), average of five trials. **e**, Calcium signals evoked during five consecutive trials within the ROI indicated by the red dashed line in **c**. **f**, Amplitude distribution of calcium signals within dendritic hotspots ($n = 50$ hotspots, 17 neurons). Grey dashed lines indicate the Gaussian fitting to the amplitude distribution of calcium signals within individual hotspots. Red line indicates the Gaussian fit to all points. Average half-width at half-maximum (HWHM) with standard deviation (±) is indicated. **g**, Left, two-photon image of a neuron (average $n = 100$ frames) and schematic representation of drug application pipette containing AP5 and Alexa-594. The red dashed lines indicate the approximate area of drug application. The green dashed box is the ROI for calcium monitoring. Right, Ca^{2+} recordings before, during and after the application of AP5. Average trace (black line) of five individual trials (grey lines). **h**, Amplitude of calcium signals before and during the application of AP5 obtained from $n = 9$ local calcium signals in four neurons. The amplitude of each Ca^{2+} signal was normalized to the mean amplitude of all signals in control condition. Paired *t*-test, $^{***}P < 0.0001$.

in which long portions of the same dendrite were discernible in the plane of focus of our recordings. In the neuron shown in Fig. 2c, we identified two dendritic hotspots of visually evoked local calcium transients. The systematic analysis of segments with a length of 3 μm along the dendrite showed that the calcium signal was present in three neighbouring segments with a clear peak in the middle segment (Fig. 2c, d). Repetitive visual stimulation reliably evoked local dendritic calcium signals (Fig. 2e; mean failure rate 22 ± 18%, 61 hotspots in 17 neurons). The spatial extent of these dendritic hotspots had an average half-width at half-maximum (HWHM) of 3.7 ± 0.8 μm ($n = 50$) (Fig. 2f).

What is the mechanism underlying these calcium signals? First, we noticed that the NMDA (*N*-methyl-D-aspartate) receptor antagonist D(−)-2-amino-5-phosphonovaleric acid (AP5) caused a major attenuation of the calcium transients, indicating their synaptic origin (Fig. 2g, h). Second, the dimensions of the hotspots were quite similar to the active dendritic shaft segments of pyramidal neurons *in vitro* displaying calcium transients as a result of the spread of calcium from single active spines[34,35]. In line with this possibility, we also identified spines at the hotspot region when constructing post hoc 'super-average' images (Fig. 2c bottom). Furthermore, previous recordings performed in basal dendrites of neocortical neurons *in vitro* demonstrated that focally evoked subthreshold excitatory postsynaptic potentials induce calcium transients in dendritic compartments of comparable dimensions[14]. In our recordings, the mean amplitude of hotspot calcium transients (Methods) was $\Delta f/f = 0.25 \pm 0.07$ ($n = 50$). This value is comparable to the amplitudes of back-propagating action-potentials-dependent dendritic calcium transients evoked by the preferred orientation ($\Delta f/f = 0.37 \pm 0.13$, mean number of action potentials 3.1 ± 1.1, $n = 50$; Supplementary Fig. 1c). Thus, the amplitude and the spatial extent of these visually evoked calcium transients resemble those generated by individual synaptic inputs, but not those evoked by dendritic NMDA spikes, which produce calcium transients that cover larger dendritic domains and have manifold larger amplitudes[31,36,37].

Mapping dendritic distribution of sensory inputs

To determine the spatial distribution of the dendritic hotspots reflecting sensory inputs, we performed experiments in which we attempted to image as many focal planes as possible in every neuron, requiring 1–2 h of whole-cell recording. In each focal plane, we determined the orientation preference of the local calcium signals by presenting drifting gratings (Methods). Figure 3a illustrates an experiment in which four focal planes were imaged at various depths under the cortical surface. A total of 13 hotspots were identified in this neuron. Figure 3b shows the response from three selected hotspots (numbered 4, 12 and 7 in Fig. 3a) obtained during presentation of eight directions of drifting gratings. From these averaged calcium transients ($n = 6$ trials), we constructed polar plots for each hotspot (Fig. 3c). A closer inspection of the polar plots revealed the presence of multiple orientation preferences in this and all other neurons. The dendritic distribution of the orientation preferences did not appear to follow any strict rule, but seemed to be randomly distributed throughout the dendritic tree. Another remarkable finding is that the calcium transients of most local dendritic hotspots displayed a pronounced orientation preference. In order to quantify the tuning level, we calculated the OSI for each hotspot and found that the majority of hotspots (72%, $n = 102$) were highly tuned for a particular orientation (OSI > 0.5). The average OSI value for all hotspots of the neuron shown in Fig. 3 was 0.63. Comparable results were obtained from 16 additional neurons (mean OSI = 0.59; $n = 102$

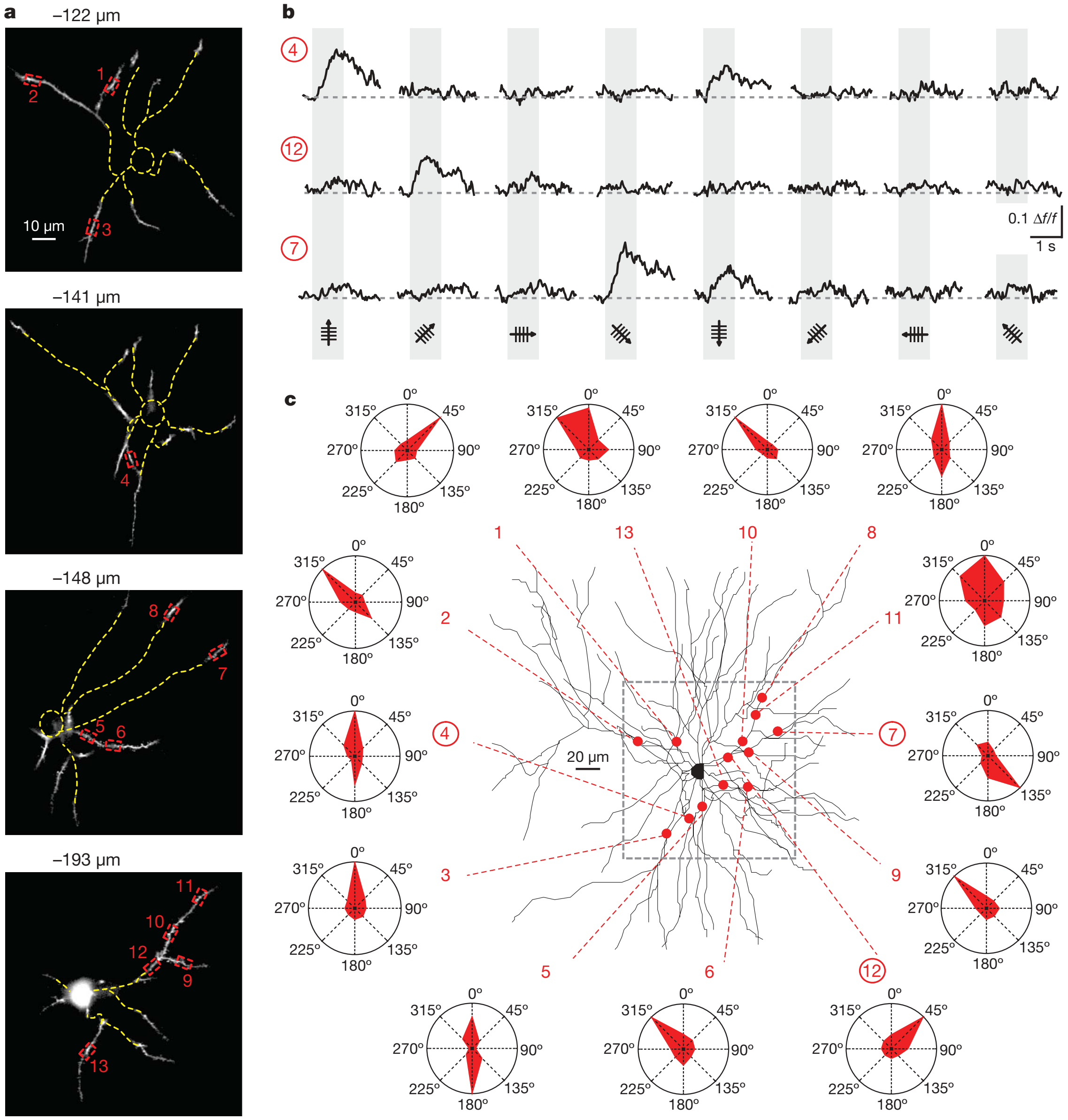

Figure 3 | Heterogeneity and distribution pattern of orientation-tuned dendritic hotspots. a, Four two-photon images (each an average of $n = 100$ frames) of a layer 2/3 neuron obtained at different depths under the cortical surface as indicated. Red dashed boxes indicate hotspots of local dendritic calcium signalling. **b**, Local dendritic calcium signals evoked by drifting gratings of different orientations (average of six trials) at three different dendritic sites indicated in **a**. **c**, Location of each hotspot indicated as a red dot on the *Z*-projection of the reconstructed dendritic tree. Red dashed lines point to the polar plot obtained for the corresponding local Ca^{2+} signals. The frame (grey dashed line) indicates the area of imaging. The output signal of the neuron was tuned for the vertical orientation.

hotspots). An important finding was that dendritic hotspots were found in each of the recorded neurons (17/17), regardless of the tuning level of action potential firing and even in the neurons that were not reliably firing in response to drifting gratings. This suggests that these hotspots represent a general and highly reliable feature of layer 2/3 neurons of the primary visual cortex.

Hotspots of the same orientation preference in a given neuron were found widely dispersed over various dendrites. For example, in the neuron shown in Fig. 4a left, we identified six hotspots for the stimulus orientation indicated in the figure and, remarkably, each hotspot was on a different dendritic branch. The analysis of a larger set of neurons ($n = 8$, Fig. 4a right) confirmed this widespread distribution and emphasized the absence of any clustering of inputs on single dendrites. Furthermore, hotspots coding for the same orientation were found throughout the entire three-dimensional space surrounding the cell body. A similar wide distribution was observed for all four orientations tested (Supplementary Fig. 2). The absence of input clustering became particularly obvious when we analysed the inputs to individual dendritic branches. Figure 4b shows three examples of dendritic branches with neighbouring hotspots that have different orientation preferences. In 9/10 dendritic branch segments, localized between two branching points, we encountered two or three hotspots tuned for different orientation preferences. In just one out of these 10 cases, neighbouring hotspots coded for the same orientation. The graph in Fig. 4c right summarizes these results. The left panel of Fig. 4c shows that all 'full dendrites', that is, individual dendrites together with all their higher order branches, received inputs for multiple orientations. Finally, we compared in 12 neurons the tuning levels of the firing pattern, representing the output signal, with the tuning levels of local dendritic calcium responses, representing the synaptic input signals. Experimentally, the orientation preference of spike firing in these neurons was determined during the initial 25–30 min of whole-cell recording during which the calcium indicator dye was allowed to equilibrate in the dendrites. Then, the neurons

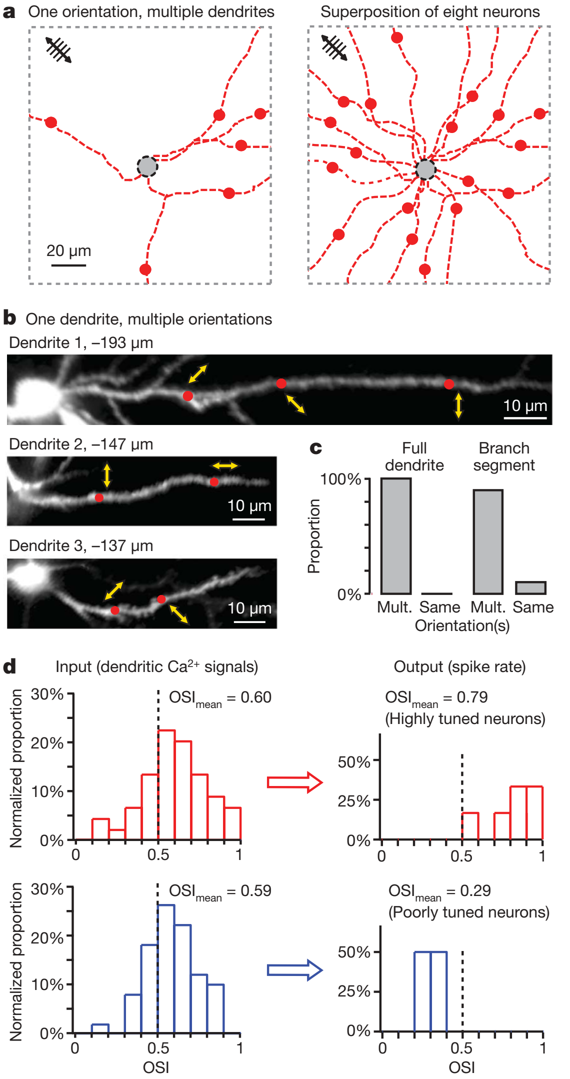

Figure 4 | Spatial arrangement of dendritic hotspots and input–output relation. **a**, Distribution of dendritic hotspots (red dots) tuned for the orientation preference indicated in the upper left corner, in the dendritic tree of a neuron (left panel). Right panel, summary of the results obtained for the same orientation in eight neurons. Cell bodies are indicated by the grey-filled dashed circles (black), dendrites are indicated by dashed red lines (*Z*-projections reconstructed from stacks). **b**, Three two-photon images of dendrites (each an average of $n = 100$ frames) at higher magnification with hotspots as indicated. Yellow arrows indicate the preferred orientation of local calcium signal in the corresponding hotspot. Note that the hotspots in dendrites 2 and 3 as well as the two distal hotspots in dendrite 1 were located in branch point-delimited segments. **c**, Summary graphs. Left panel, the proportion of full dendrites ($n = 12$) with hotspots coding for multiple orientations versus those with just one and the same orientation (≥ 3 hotspots per full dendrite). Right panel, the proportion of branch segments (between two branching points) with hotspots coding for multiple orientations versus those with the same orientation (≥ 2 hotspots per branch, $n = 10$). **d**, Input–output relations in highly tuned (upper) and poorly tuned (lower) neurons. The red and blue histograms show orientation selectivity indices (OSIs as indicated) for the input (Ca^{2+} signals in dendritic hotspots) and the output (spiking rate) of highly and poorly tuned neurons ($n = 6$ for each group), respectively.

were hyperpolarized and we determined the orientation preference of local dendritic calcium signals. We compared six highly tuned neurons (mean OSI = 0.79) with six broadly tuned ones (mean OSI = 0.29) (Fig. 4d right). Unexpectedly, the input signals had very similar tuning levels for the two neuronal groups, with mean OSI values of 0.60 and 0.59, for highly and broadly tuned firing patterns, respectively. This disparity between input and output signals, combined with the above-mentioned observation that all neurons had input signals coding for multiple orientations, indicates that the orientation preference of the output signal is the result of a computational process taking place on the level of individual neurons.

Conclusions

Our results reveal basic insights into the dendritic organization of sensory inputs to neurons of the visual cortex *in vivo*. First, we identified discrete dendritic hotspots as synaptic entry sites for specific sensory features. These hotspots represent novel dendritic calcium signals *in vivo* and were found in all layer 2/3 neurons, irrespective of their output firing pattern. Second, we showed that afferent sensory inputs with the same orientation preference are widely dispersed over the dendritic tree and do not converge on single dendrites, as repeatedly proposed in recent years (see review in ref. 11 and references therein). Third, we found that even neurons with a highly tuned output signal receive input signals that are heterogeneous and code for multiple orientations and/or directions. Thus, taken together, our results support a neuronal integration model involving summation of distributed inputs, rather than models that stress the role of convergent inputs to single dendrites[6,15]. However, it is certainly possible that other types of cortical neurons, especially those with pronounced apical tufts[38] or neurons in other species with a columnar organization of the visual cortex[17,19–21], have more clustered sensory inputs to the same dendrite, capable of generating large amplitude dendritic spikes[6,11]. The approach introduced in this study opens the way to a detailed analysis of various types of neurons followed by the construction of functional wiring diagrams of sensory pathways with single input resolution *in vivo*.

METHODS SUMMARY

C57BL/6 mice (postnatal day (P)28–P34) were prepared for *in vivo* two-photon calcium imaging and whole-cell recordings under isoflurane anaesthesia as described previously[39]. Whole-cell patch-clamp recordings of layer 2/3 neurons of primary visual cortex (monocular region) were performed by 'shadow-patching'[25]. Neurons were dialysed with a pipette solution containing the fluorescent Ca^{2+} indicator Oregon green BAPTA-1 hexapotassium (OGB-1; 100 μM), Alexa-594 (25 μM) and biocytin ($2\ mg\ ml^{-1}$). Basal and oblique dendrites that appeared on the same focal plane were imaged by high-speed two-photon microscopy involving a resonant galvo-scanner[30]. Membrane potential changes and Ca^{2+} signals were simultaneously recorded. The focal plane depth and the imaged area were chosen to contain as many dendrites as possible. At each focal plane, we imaged the activity evoked by drifting square wave gratings (0.03 cycles per degree, 1 Hz, eight directions, standing phase 2 s, drifting phase 1 s). Transient changes in Ca^{2+} fluorescence ($\Delta f/f$) were systematically examined by an adaptive algorithm, which involved small regions of interest (ROIs) of 3×4 μm, noise filtering and pattern matching. The NMDA receptor antagonist AP5 (together with Alexa-594) was locally applied by pressure ejection close to the imaged dendrites. The spread of the ejected solution was monitored by imaging Alexa fluorescence. The tuning level of local dendritic calcium signals with regard to the orientation of the drifting grating was quantified by an OSI[24].

Received 14 October 2009; accepted 24 February 2010.

1. London, M. & Häusser, M. Dendritic computation. *Annu. Rev. Neurosci.* **28,** 503–532 (2005).
2. Bloodgood, B. L. & Sabatini, B. L. Ca^{2+} signaling in dendritic spines. *Curr. Opin. Neurobiol.* **17,** 345–351 (2007).
3. Markram, H. & Sakmann, B. Calcium transients in dendrites of neocortical neurons evoked by single subthreshold excitatory postsynaptic potentials via low-voltage-activated calcium channels. *Proc. Natl Acad. Sci. USA* **91,** 5207–5211 (1994).
4. Nevian, T. & Sakmann, B. Spine Ca^{2+} signaling in spike-timing-dependent plasticity. *J. Neurosci.* **26,** 11001–11013 (2006).
5. Yuste, R. & Denk, W. Dendritic spines as basic functional units of neuronal integration. *Nature* **375,** 682–684 (1995).
6. Häusser, M. & Mel, B. Dendrites: bug or feature? *Curr. Opin. Neurobiol.* **13,** 372–383 (2003).
7. Helmchen, F., Svoboda, K., Denk, W. & Tank, D. W. *In vivo* dendritic calcium dynamics in deep-layer cortical pyramidal neurons. *Nature Neurosci.* **2,** 989–996 (1999).
8. Murayama, M. *et al.* Dendritic encoding of sensory stimuli controlled by deep cortical interneurons. *Nature* **457,** 1137–1141 (2009).

9. Svoboda, K., Denk, W., Kleinfeld, D. & Tank, D. W. *In vivo* dendritic calcium dynamics in neocortical pyramidal neurons. *Nature* **385**, 161–165 (1997).
10. Johnston, D. & Narayanan, R. Active dendrites: colorful wings of the mysterious butterflies. *Trends Neurosci.* **31**, 309–316 (2008).
11. Larkum, M. E. & Nevian, T. Synaptic clustering by dendritic signalling mechanisms. *Curr. Opin. Neurobiol.* **18**, 321–331 (2008).
12. Ohki, K. & Reid, R. C. Specificity and randomness in the visual cortex. *Curr. Opin. Neurobiol.* **17**, 401–407 (2007).
13. Magee, J. C. Dendritic integration of excitatory synaptic input. *Nature Rev. Neurosci.* **1**, 181–190 (2000).
14. Polsky, A., Mel, B. W. & Schiller, J. Computational subunits in thin dendrites of pyramidal cells. *Nature Neurosci.* **7**, 621–627 (2004).
15. Cash, S. & Yuste, R. Linear summation of excitatory inputs by CA1 pyramidal neurons. *Neuron* **22**, 383–394 (1999).
16. Bannister, A. P. Inter- and intra-laminar connections of pyramidal cells in the neocortex. *Neurosci. Res.* **53**, 95–103 (2005).
17. Hirsch, J. A. & Martinez, L. M. Laminar processing in the visual cortical column. *Curr. Opin. Neurobiol.* **16**, 377–384 (2006).
18. Svoboda, K., Helmchen, F., Denk, W. & Tank, D. W. Spread of dendritic excitation in layer 2/3 pyramidal neurons in rat barrel cortex *in vivo*. *Nature Neurosci.* **2**, 65–73 (1999).
19. Hubel, D. H. & Wiesel, T. N. Receptive fields, binocular interaction and functional architecture in the cat's visual cortex. *J. Physiol. (Lond.)* **160**, 106–154 (1962).
20. Hubel, D. H. & Wiesel, T. N. Receptive fields and functional architecture of monkey striate cortex. *J. Physiol. (Lond.)* **195**, 215–243 (1968).
21. White, L. E. & Fitzpatrick, D. Vision and cortical map development. *Neuron* **56**, 327–338 (2007).
22. Dräger, U. C. Receptive fields of single cells and topography in mouse visual cortex. *J. Comp. Neurol.* **160**, 269–290 (1975).
23. Métin, C., Godement, P. & Imbert, M. The primary visual cortex in the mouse: receptive field properties and functional organization. *Exp. Brain Res.* **69**, 594–612 (1988).
24. Niell, C. M. & Stryker, M. P. Highly selective receptive fields in mouse visual cortex. *J. Neurosci.* **28**, 7520–7536 (2008).
25. Kitamura, K., Judkewitz, B., Kano, M., Denk, W. & Häusser, M. Targeted patch-clamp recordings and single-cell electroporation of unlabeled neurons *in vivo*. *Nature Methods* **5**, 61–67 (2008).
26. Kerr, J. N., Greenberg, D. & Helmchen, F. Imaging input and output of neocortical networks *in vivo*. *Proc. Natl Acad. Sci. USA* **102**, 14063–14068 (2005).
27. Anderson, J., Lampl, I., Reichova, I., Carandini, M. & Ferster, D. Stimulus dependence of two-state fluctuations of membrane potential in cat visual cortex. *Nature Neurosci.* **3**, 617–621 (2000).
28. Carandini, M. & Ferster, D. Membrane potential and firing rate in cat primary visual cortex. *J. Neurosci.* **20**, 470–484 (2000).
29. Bringuier, V., Chavane, F., Glaeser, L. & Fregnac, Y. Horizontal propagation of visual activity in the synaptic integration field of area 17 neurons. *Science* **283**, 695–699 (1999).
30. Rochefort, N. L. *et al.* Sparsification of neuronal activity in the visual cortex at eye-opening. *Proc. Natl Acad. Sci. USA* **106**, 15049–15054 (2009).
31. Gordon, U., Polsky, A. & Schiller, J. Plasticity compartments in basal dendrites of neocortical pyramidal neurons. *J. Neurosci.* **26**, 12717–12726 (2006).
32. Koester, H. J. & Sakmann, B. Calcium dynamics associated with action potentials in single nerve terminals of pyramidal cells in layer 2/3 of the young rat neocortex. *J. Physiol. (Lond.)* **529**, 625–646 (2000).
33. Bollmann, J. H. & Engert, F. Subcellular topography of visually driven dendritic activity in the vertebrate visual system. *Neuron* **61**, 895–905 (2009).
34. Kovalchuk, Y., Eilers, J., Lisman, J. & Konnerth, A. NMDA receptor-mediated subthreshold Ca^{2+} signals in spines of hippocampal neurons. *J. Neurosci.* **20**, 1791–1799 (2000).
35. Noguchi, J., Matsuzaki, M., Ellis-Davies, G. C. & Kasai, H. Spine-neck geometry determines NMDA receptor-dependent Ca^{2+} signaling in dendrites. *Neuron* **46**, 609–622 (2005).
36. Holthoff, K., Kovalchuk, Y., Yuste, R. & Konnerth, A. Single-shock LTD by local dendritic spikes in pyramidal neurons of mouse visual cortex. *J. Physiol. (Lond.)* **560**, 27–36 (2004).
37. Major, G., Polsky, A., Denk, W., Schiller, J. & Tank, D. W. Spatiotemporally graded NMDA spike/plateau potentials in basal dendrites of neocortical pyramidal neurons. *J. Neurophysiol.* **99**, 2584–2601 (2008).
38. Larkum, M. E., Nevian, T., Sandler, M., Polsky, A. & Schiller, J. Synaptic integration in tuft dendrites of layer 5 pyramidal neurons: a new unifying principle. *Science* **325**, 756–760 (2009).
39. Stosiek, C., Garaschuk, O., Holthoff, K. & Konnerth, A. *In vivo* two-photon calcium imaging of neuronal networks. *Proc. Natl Acad. Sci. USA* **100**, 7319–7324 (2003).

Supplementary Information is linked to the online version of the paper at www.nature.com/nature.

Acknowledgements We are grateful to B. Sakmann for discussions and to Y. Kovalchuk for help in the initial experiments. This work was supported by grants from the DFG (to A.K.) and the Friedrich Schiedel Foundation. A.K. is a Carl von Linde Senior Fellow of the Institute for Advanced Study of the TUM. H.J., N.L.R. and X.C. were supported by the DFG (IRTG 1373).

Author Contributions H.J., N.L.R. and X.C. carried out the experiments. H.J., N.L.R. and A.K. performed the analysis. A.K. designed the study and wrote the manuscript with the help of all authors.

Author Information Reprints and permissions information is available at www.nature.com/reprints. The authors declare no competing financial interests. Correspondence and requests for materials should be addressed to A.K. (arthur.konnerth@lrz.tum.de).

Supplementary Methods

Animals and surgery

All experimental procedures were performed in accordance with institutional animal welfare guidelines and were approved by the government of Bavaria, Germany. A total of 18 BL/6 mice (P28-P34) were prepared for *in vivo* experiments, as described previously[39]. Briefly, the mice were placed onto a warming plate (38°C) and anaesthetized by inhalation of 1.5% isoflurane (Curamed, Karlsruhe, Germany) in pure O_2. After removing the skin, a custom-made recording chamber[40] was then glued to the skull with cyanoacrylic glue (UHU, Buhl-Baden, Germany). The mouse was then transferred into the set-up, placed onto a warming plate (38° C) and continuously supplied with 0.8% isoflurane in pure O_2 (breathing rate 110-130 breaths per minute). A small craniotomy (~0.8×0.6 mm) was performed above the monocular region of primary visual cortex using a thin (30G) injection needle. The exposed region was subsequently covered by 2% agar (~1 mm thick) to reduce vibrations of brain tissue. The recording chamber was perfused with warm (37° C) extracellular perfusion saline containing (in mM): 125 NaCl, 4.5 KCl, 26 $NaHCO_3$, 1.25 NaH_2PO_4, 2 $CaCl_2$, 1 $MgCl_2$, 20 glucose, pH 7.4, when bubbled with 95% O_2 and 5% CO_2. Eye cream (Bepanthen, Bayer, Germany) was applied on both eyes to prevent dehydration during surgery. After surgery, the anaesthesia level was decreased to 0.8% isoflurane for recordings (breathing rate 110-130 breaths per minute).

Electrophysiology and drug application

The position of the primary visual cortex was located according to brain atlas coordinates (Bregma -3.5 to -4.5 mm, 2 to 2.5 mm lateral to the midline[41]). In all experiments the correct location of the recorded neurons was confirmed *in vivo* by their responses to visual stimuli and post-hoc by imaging of the stained brain area. *In vivo* whole-cell patch-clamp of layer 2/3 neurons was performed by using ‘shadow patching’[25]. Borosilicate pipettes of 5 to 7 MΩ resistance were filled with a standard pipette solution (125 mM K-gluconate, 25 mM KCl, 12.5 mM HEPES, 5 mM Mg-ATP, 0.4 mM Na_2GTP, 12.5 mM Na-phosphocreatine) to which 100 μM Oregon Green BAPTA-1 Hexapotassium, 25 μM Alexa-594 and Biocytin (2 mg/ml; FLUKA), all dissolved in water, were added. Similar results were obtained in 3 experiments (3 neurons in 3 mice) when using a ‘low chloride’ pipette solution, containing 112 mM K-gluconate, 8 mM KCl, 10 mM HEPES, 4 mM Mg-ATP, 0.375 mM Na_2GTP, 10 mM Na-Phosphocreatine, 100 µM Oregon Green BAPTA-1 Hexapotassium, 25 µM Alexa-594 (see Supplementary Fig. 3). Current-clamp recordings were made with an EPC-9 amplifier. Signals were filtered at 3 kHz and digitized at 10 kHz by the Pulse software (both from *HEKA*, Germany). Series resistances ranged from 15 to 40 MΩ. The resting membrane potentials ranged from – 67 to -62 mV. For the recordings of subthreshold activities, the neurons were hyperpolarized to membrane potentials below -70 mV. In the pharmacology experiments (n=4), a pipette filled with 5 mM d-AP5 and 25 µM Alexa-594 in standard extracellular saline solution was placed close to the imaged dendrites. The drug was delivered by gentle pressure injection. The area of diffusion was monitored at the beginning of each recording trial by imaging Alexa fluorescence.

High-speed two-photon Ca^{2+} imaging

In vivo Ca^{2+} imaging was performed by using a custom-built two-photon microscope based on Ti:Sapphire pulsing laser (model: Chameleon, repetition rate: 80 MHz, pulse width: 140 fs; Coherent, USA) and resonant galvo-mirror (8 kHz; GSI) system[42].

The scanner was mounted on an upright microscope (BX51WI, Olympus, Tokyo, Japan) equipped with a water-immersion objective (40x/0.8 Nikon, Japan). Emitted photons were detected by two detection channels equipped with photomultiplier tubes (H7422-40; Hamamatsu), a ‘green’ channel for OGB-1 dependent calcium recordings (480-560 nm) and a ‘red’ channel for the Alexa-594 generated fluorescence (580-680 nm). Full-frame images at 480×400 pixel resolution were acquired at 30 Hz or at a resolution of 480x180 pixels at 60 Hz by custom-programmed software based on LabVIEW™ (version 8.2; National Instruments, USA). Approximately 30 minutes after forming the whole-cell configuration, the basal and oblique dendrites were well labeled by OGB1. The focal plane was chosen to contain as many dendrites as possible. At each focal plane, we imaged spontaneous activity (for at least 2 min) as well as visually-evoked activity (6 to 10 trials of visual stimulation). At the end of each experiment, a Z-stack of the fluorescently labeled neuron was acquired (0.5 µm step size).

Visual stimulation

Visual stimuli were generated by Matlab^{TM} (release 2007b; Mathworks Inc.) with the "Psychtoolbox" add-on package (http://psychtoolbox.org/wikka.php?wakka=HomePage). Visual stimuli were projected on a screen placed 30 cm from the contralateral eye, covering 80° x 67° of the visual field. Each trial of visual stimulation started with a gray screen (mean luminance) for 4 s, followed by a stationary square-wave grating for 2 s and the corresponding drifting phase for 1 s (0.03 cycle per degree, 1 Hz, 8 directions, contrast 80%, mean luminance 3.7 cd/m^2). At each focal plane, evoked activities were imaged during 6 to 10 trials.

Reconstruction of dendrites

For dendrite reconstructions, neurons were filled with Biocytin (2 mg/ml; FLUKA). At the end of the recordings, animals were transcardially perfused with phosphate buffer solution (0.1 M PBS) followed by 4 % paraformaldehyde (PFA) in 0.1 M PBS. Brains were kept in 4% PFA overnight and maintained in PBS thereafter. 100 µm-thin frontal sections were cut with a vibratome. Biocytin-labeled neurons were visualized using the avidin:biotinylated horseradish peroxidase complex (Vectastain ABC kit, Vector Laboratories, CA). Three neurons were completely reconstructed in 3D with the Neurolucida software (MicroBrightField, Colchester, VT, USA) using a up-right microscope (Zeiss, Germany) with an oil immersion x100/1.4 numerical aperture objective.

Data analysis

Electrophysiology and Ca^{2+} imaging data were analyzed off-line by using custom-written procedures in Igor^{TM} and LabVIEW^{TM}. The amplitude of stimulus-evoked subthreshold depolarizing responses was calculated by subtracting the mean amplitude before the onset of drifting grating stimulation (0.2 s) from the mean value during the drifting period (1 s). Calcium-dependent changes in relative fluorescence (Δf/f) represent the mean fluorescence of all pixels within specified region-of-interests (ROIs). Local dendritic calcium signals were determined by analyzing the dendrites with consecutive small ROIs (rectangles of 3x4 µm) (e.g. Fig. 2c). All Δf/f traces were processed with an exponentially-averaging IIR filter (time constant 200 ms), then split according to the onset of drifting phase for each direction, and averaged over trials. Calcium transients were automatically detected with a templatematching algorithm, taking into account the rise and decay times properties of the calcium signals. The amplitude of calcium transients was determined as the mean value in a time window around the peak response amplitude (1 frame before peak and 6 frames after). A calcium transient was accepted as a signal when its amplitude was greater than 3 times the standard deviation of the noise band. The tuning level of drifting grating-evoked responses was quantified by an orientation selectivity index (OSI)[24]. The OSI was defined as $(R_{\text{pref}} - R_{\text{ortho}})/(R_{\text{pref}} + R_{\text{ortho}})$, where R_{pref}, the response in the preferred orientation, was the response with the largest magnitude. For local dendritic calcium signals, R_{pref} was determined as the mean of the integral of the calcium transients for the two corresponding opposite directions. R_{ortho} was the similarly calculated response evoked by the orthogonal orientation. Highly and poorly tuned neurons were defined as neurons with an $\text{OSI}>0.5$ and $\text{OSI}\leq 0.5$ respectively. Polar plot representations of visually-evoked firing rates, of subthreshold depolarizations or of dendritic calcium transients were normalized with respect to the corresponding maximal responses.

References

40. Garaschuk, O., Milos, R. I. & Konnerth, A. Targeted bulk-loading of fluorescent indicators for two-photon brain imaging in vivo. *Nat Protoc.* **1**, 380-6 (2006).
41. Paxinos, G. & Franklin, K. B. J. The mouse brain in stereotaxic coordinates. Academic Press, San Diego, USA (2001).
42. Sanderson, M. J. & Parker, I. Video-rate confocal microscopy. *Methods Enzymol.* **360**, 447-81 (2003).

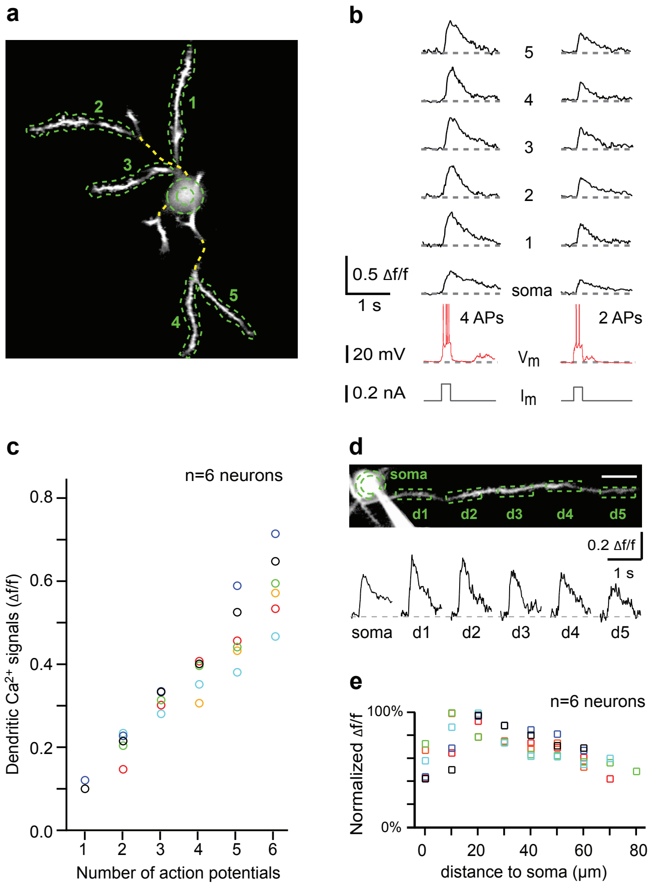

Supplementary Figure 1 | Global dendritic calcium signals are generated by back-propagating action potentials. a, Two-photon fluorescence image (average of 100 frames) of a layer 2/3 neuron in the mouse visual cortex. Yellow dotted lines indicate out-of-focus portions of dendrites. Green dotted lines indicate the region-of-interests (ROIs) for calcium recordings. **b**, Calcium transients (Δf/f) recorded in five dendrites and in the soma (indicated by numbers in panel a), during two trials in which 4 and 2 action potentials (APs) (V_m, lower red trace) were evoked by current injection (I_m, lowest gray trace). **c,** Amplitude of dendritic calcium transients versus the number of action potentials. Each color represents the mean value for a single neuron, recorded in dendritic ROIs of 50 μm length. **d-e,** Amplitudes of calcium transients plotted versus the distance from the soma. Recordings in panel d were obtained at the dendritic sites d1 through d5 and the soma, as indicated in the image (average of n=100 frames). The graph in panel e displays the amplitude of calcium transient at different dendritic distances for 6 neurons (marked in different colors). Each value represents the average amplitude obtained from 30 trials. For each trial, values were normalized with respect to the largest amplitude. Scale bar, 10 μm.

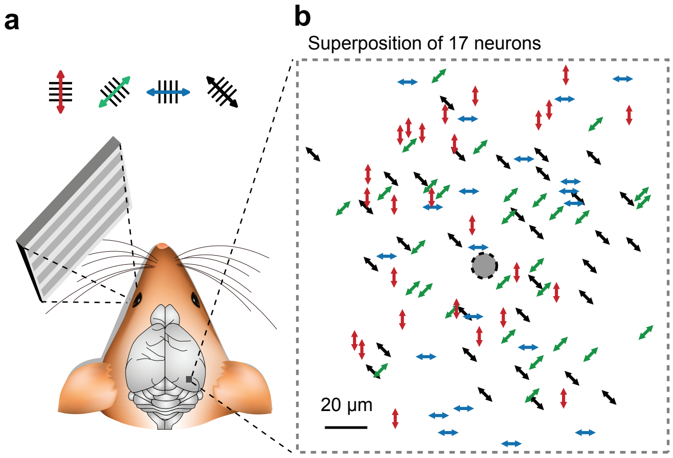

Supplementary Figure 2 │ Highly heterogeneous distribution of orientation-tuned hot spots throughout the dendritic tree. a, Schematic of the experimental arrangement for visual stimulation. **b,** Superposition of orientation-tuned hot spots (Z-projection of n=107 sites) obtained from 17 layer 2/3 neurons. Each of the four orientations tested is displayed in a different color. The neurons' somata (gray filled black dotted circle) were superimposed. Note the salt-and-pepper distribution of the orientation-tuned hot spots.

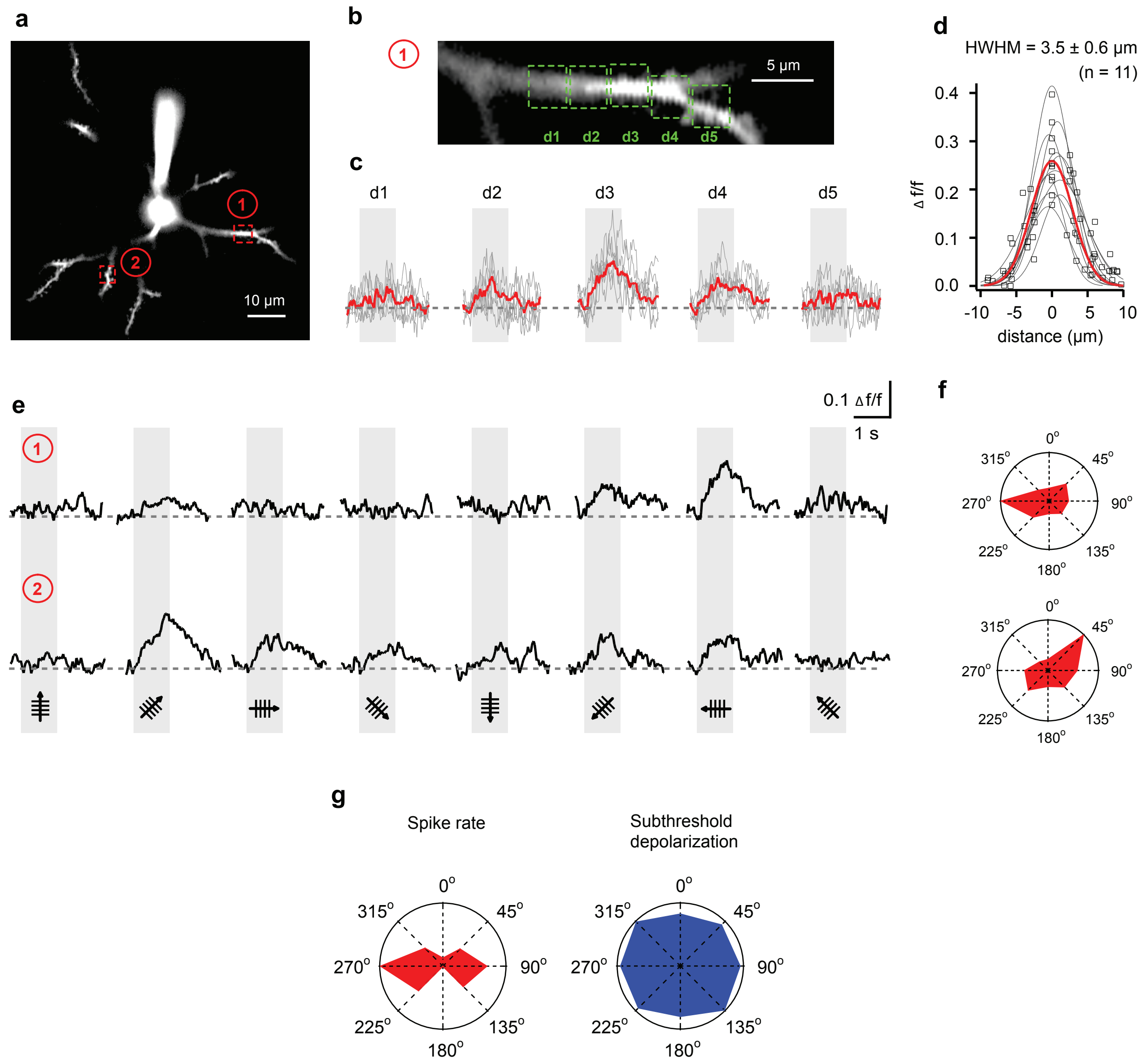

Supplementary Figure 3 │ Subthreshold local dendritic calcium signals and membrane potential responses obtained with the 'low chloride' pipette solution Recordings from 3 neurons with a total of 11 hot spots.

a, Two-photon image (average of 500 frames) of a layer 2/3 neuron of the visual cortex of a 32-day-old mouse used for *in vivo* calcium recordings in panels c and e. Two hot spots are indicated by red dashed boxes. **b,** Enlarged view of the area near hot spot 1 as marked in panel a. The green dashed boxes d1 to d5 (3 μm length) indicate the regions of interest used for analysis. **c,** Superimposed 6 individual trials (gray traces) and the average (red traces) of calcium transients in d1 through d5. **d,** Amplitude distribution of calcium transients (n=11 hot spots, 3 neurons). Gray lines indicate the Gaussian fitting to the amplitude of calcium signals in dendritic regions at different distances from the center of each hotspot. Red line indicates the Gaussian fit to the pool of all data points. Average half-width at half-maximum (HWHM) with standard deviation as indicated. This HWHM value is not significantly different from that obtained with standard pipette solution (Fig. 2f). **e,** Local dendritic calcium signals evoked by drifting gratings of different orientations (average of 6 trials) for the two dendritic sites (as indicated in panel a). **f,** Polar plots obtained for the local calcium signals shown in panel e. Note the similarity to the results shown in Fig. 3c. **g,** Polar plots of visually-evoked electrical responses obtained with whole-cell recordings. Red plot: spike rate, average of 9 trials. Blue plot: amplitude of subthreshold depolarization, average of 25 trials. Note the similarity to the results shown in Fig. 1e.

Project IV

In vivo two-photon imaging of sensory-evoked dendritic calcium signals in cortical neurons

(Published in **Nat Protoc**, 2011, 6: 28 - 35)

In vivo two-photon imaging of sensory-evoked dendritic calcium signals in cortical neurons

Hongbo Jia[1,2], Nathalie L Rochefort[1,2], Xiaowei Chen[1] & Arthur Konnerth[1]

[1]Institute of Neuroscience and Center for Integrated Protein Science, Technische Universität München, München, Germany. [2]These authors contributed equally to this work. Correspondence should be addressed to A.K. (arthur.konnerth@lrz.tum.de).

Neurons in cortical sensory regions receive modality-specific information through synapses that are located on their dendrites. Recently, the use of two-photon microscopy combined with whole-cell recordings has helped to identify visually evoked dendritic calcium signals in mouse visual cortical neurons *in vivo*. The calcium signals are restricted to small dendritic domains ('hotspots') and they represent visual synaptic inputs that are highly tuned for orientation and direction. This protocol describes the experimental procedures for the recording and the analysis of these visually evoked dendritic calcium signals. The key points of this method include delivery of fluorescent calcium indicators through the recording patch pipette, selection of an appropriate optical plane with many dendrites, hyperpolarization of the membrane potential and two-photon imaging. The whole protocol can be completed in 5–6 h, including 1–2 h of two-photon calcium imaging in combination with stable whole-cell recordings.

INTRODUCTION

Mammalian cortical neurons compute sensory information that arrives through numerous synaptic inputs located on their dendrites[1]. To achieve a better understanding of dendritic computation *in vivo*[2–4], it is important to identify and characterize the input signals in the living brain. A fruitful approach to study synaptically evoked dendritic signals is based on the use of fluorescent calcium indicators and on appropriate imaging techniques that allow the recording of the dynamics of intracellular Ca^{2+} concentration in dendrites (reviewed in ref. 5). This approach has been used extensively *in vitro* and has helped to identify synaptically evoked dendritic calcium transients in neurons of many brain regions[5–9]. *In vivo* studies have been restricted mostly to the recording of action potential–related dendritic Ca^{2+} signals[10–16]. However, until recently, the nature of sensory-evoked synaptic input signals in the dendrites of mammalian cortical neurons remained unexplored.

Combined two-photon imaging and whole-cell recordings *in vivo*

Here we describe a protocol for recording visually evoked local dendritic calcium signals in layer 2 and 3 (layer 2/3) neurons of mouse visual cortex *in vivo*[17]. For this purpose, we first established the whole-cell recording configuration with the 'shadow patch' approach[18], using patch pipettes containing the calcium indicator dye Oregon Green BAPTA-1 (OGB-1). We first noticed that action potential firing produced global dendritic calcium signals that were evoked by back-propagating action potentials[13,17,18]. Synaptically evoked dendritic calcium transients, as found in tectal neurons of the tadpole[19], could not be unambiguously identified at normal resting potential involving action potential firing. However, when we hyperpolarized the neuron to prevent action potential firing, we were able to reliably detect localized calcium transients in response to visual stimulation by drifting gratings. Our results indicate that these sensory-evoked dendritic calcium transients are mediated by *N*-methyl-D-aspartate receptor-dependent glutamatergic synapses[17]. Compared with earlier studies involving the loading of calcium indicator dyes though sharp microelectrodes (50–100 MΩ resistance)[10,11], the approach used here is based on the use of whole-cell recordings with low-resistance patch electrodes (6–7 MΩ). Our procedure allows the direct visualization of the targeted cell body before recording[18], a rapid equilibration of the calcium indicator dye within the cell and a reliable control of the membrane potential[20]. A crucial advantage of *in vivo* whole-cell recordings is that they enable stable and long-lasting two-photon imaging of synaptically induced dendritic calcium signals. An alternative approach for imaging dendritic activity, not requiring simultaneous electrical recordings, involves calcium indicator dye loading through electroporation[21,22]. However, this approach does not allow the active hyperpolarization of the neurons, thus making it difficult to isolate the synaptic input–related subthreshold events.

Applications

Our method can be used to perform recordings not only in the visual cortex but also in other brain regions. We have also obtained preliminary results with this method in the auditory, the barrel and the motor cortices, as well as in the cerebellar cortex (Z. Varga, H.J., X.C., N.L.R., A.K., unpublished data). We have applied this method only to mice, but we are confident that it can also be used successfully in other species. Our recordings were all obtained in layer 2/3 cortical pyramidal neurons. However, the method can be adapted easily to other types of neurons (e.g., interneurons).

Current constraints

At present, the method is largely restricted to neurons that are located near the surface (i.e., at a depth of 100–300 μm) of the cortex. Improvements in two-photon microscopy, such as the use of regenerative amplifiers[23], may help for the investigation of dendrites in deeper cortical layers, whereas improved methods of multiphoton endoscopy[24] may provide access to dendrites of neurons in subcortical brain regions. An important open question concerns the precise nature of the sensory inputs to cortical neurons; namely, whether sensory inputs represent individual synapses or rather small clusters of synapses on a dendrite. Finally, the wide application of the method will decisively benefit from the use of genetically encoded calcium indicators (GECIs)[25–29], although the presently available GECIs are not yet sufficiently sensitive[30] for the detection of calcium signals occurring in small dendritic domains. New GECIs with a higher affinity for calcium may be suitable for dendrite imaging *in vivo*.

MATERIALS

REAGENTS

- Experimental animals. So far, this protocol has been tested only in C57/BL6 mice at the age of postnatal days 28–35 **! CAUTION** All animal experiments must be performed in accordance with the guidelines and regulations of the relevant authorities.
- Isoflurane (Abbott) **! CAUTION** Use strictly in accordance with the specifications of the isoflurane apparatus and maintain proper room ventilation.
- Lidocaine hydrochloride (20 mg ml^{-1}; e.g., Xylocaine, AstraZeneca). Lidocaine HCl is a local anesthetic agent.
- Oregon Green 488 BAPTA-1 hexapotassium salt (OGB-1; Invitrogen, cat. no. O6806). It is a membrane impermeable, calcium sensitive fluorescent indicator.
- Alexa Fluor 594 (Invitrogen, cat. no. A10438). It is a membrane impermeable, inert fluorescent indicator.
- Chemicals for artificial cerebrospinal fluid (ACSF) and patch pipette solution (all from Sigma-Aldrich): NaCl, KCl, $NaHCO_3$, NaH_2PO_4, $CaCl_2$, $MgCl_2$, glucose, KOH, K-gluconate, HEPES, Mg-ATP, Na_2-ATP, Na-phosphocreatine and biocytin.
- Agarose powder (Invitrogen, cat. no. 16500500)
- Borosilicate capillaries (Hilgenberg, cat. no. 1807516)
- Eye protecting cream (Bepanthen, Bayer Vital)
- Cyanoacrylate glue (UHU, UHU)
- Distilled water
- Oxygen supply
- Carbon dioxide supply

EQUIPMENT

- Anesthesia-monitoring system (Powerlab, ADInstruments)
- Warming plate to keep the animal at normal body temperature (home-built; just a plastic plate with a heating wire powered by direct current)
- High-speed two-photon microscope (we use a home-built device. Similar systems are commercially available from several suppliers, including Leica, Nikon, Prairie Imaging and LaVision BioTec). See EQUIPMENT SETUP for details.
- Patch-clamp amplifier (EPC10, HEKA)
- Motorized micromanipulators ('Unit Junior', Luigs & Neumann)
- Pipette puller (PC-10, Narishige)
- Recording chamber with side-access opening: made from a standard tissue-culture dish (**Fig. 1a**)
- Video projector (LT-20, NEC)
- *Software for analysis*: We generated a program, DENDRITE-1, to define regions of interest (ROIs) and to extract calcium signals from these ROIs. This program is freely available on request. The program requires the run-time environment of LabVIEW 8.5 or higher versions. Similar programs may be generated by using other data analysis software packages such as, e.g., Matlab (release 2007b; Mathworks) or WCIF-ImageJ (open source, http://www.uhnresearch.ca/facilities/wcif/fdownload.html). Further statistical analyses are performed using IGOR software (WaveMetrics).
- Isoflurane vaporizer (Drägerwerk)
- Airflow meter (KOBOLD Messring)
- Titanium-sapphire pulsing laser (Chameleon, Coherent; pulse width 140 fs, repetition rate 80 MHz)
- Resonant scanner unit (8 KHz; CRS, Cambridge Technology)
- Commercial microscope chassis (BX51W1, Olympus)
- Photomultiplier tubes (H7422-40, Hamamatsu)
- Microscope objective (long working distance, water immersion, ×40/0.8, WD 3.5 mm; Nikon)

REAGENT SETUP

Artificial cerebrospinal fluid ACSF is composed of NaCl (125 mM), 4.5 mM KCl, 26 mM $NaHCO_3$, 1.25 mM NaH_2PO_4, 2 mM $CaCl_2$, 1 mM $MgCl_2$ and 20 mM glucose; bubble with carbogen (95% O_2 + 5% CO_2). All reagents are dissolved in distilled water, for a total volume of 1 liter. The solution without glucose can be stored for days at 4 °C. **▲ CRITICAL** Glucose is added just before the experiment.

Agarose solution Boil 20 mg of agarose powder in 1 ml of ACSF until it is fully dissolved. Cool the agarose solution to a temperature just below 38 °C before applying it to the cortex. **▲ CRITICAL** Freshly prepare agarose solution just before each experiment.

Patch pipette solution Patch pipette solution consists of K-gluconate (112 mM), 8 mM KCl, 10 mM HEPES, 4 mM Mg-ATP, 0.375 mM Na_2GTP, 10 mM Na-phosphocreatine, 100 µM OGB-1 and 25 µM Alexa-594; pH is adjusted to 7.4 by KOH. All the reagents are dissolved in distilled water. **▲ CRITICAL** Freshly prepare the patch pipette solution for each experiment and keep the solution on ice throughout the experiment.

EQUIPMENT SETUP

Isoflurane anesthetic unit It consists of a pure medical oxygen supply, an isoflurane vaporizer, an airflow meter, tubing and a respiration mask.

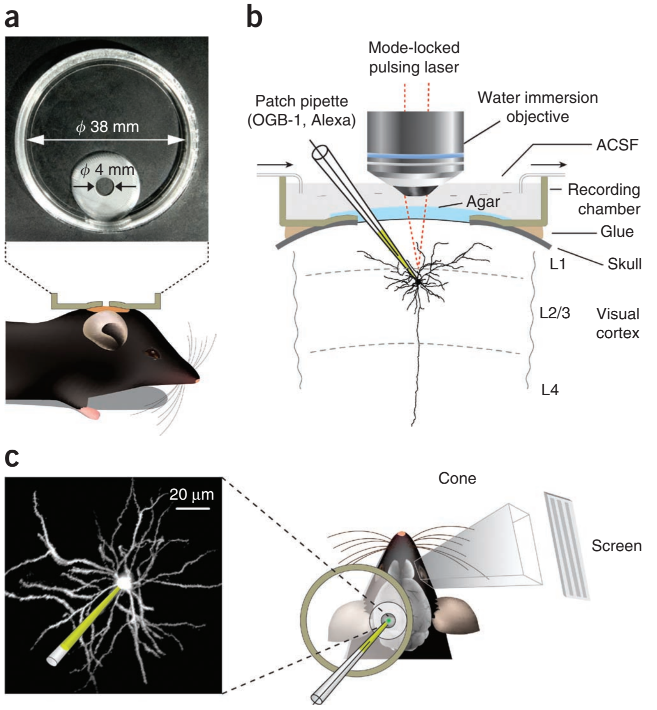

Figure 1 | Experimental arrangement for *in vivo* dendritic imaging in combination with whole-cell recordings. (**a**) Top view of the recording chamber (upper panel). The lower panel schematically shows the recording chamber (side view) fixed on the mouse skull. (**b**) Side view of the experimental arrangement. Note the positions of the dye-containing (OGB-1, Alexa) patch pipette, the water-immersion objective, the agar-covered exposed cortical surface and the recording chamber glued on the skull. Cortical layers 1, 2/3 and 4 are indicated as L1, L2/3 and L4. The arrows indicate the flow direction of the ACSF superfusing the cortical surface. (**c**) Left panel, *z*-projection (along the dorsoventral axis) of *in vivo* two-photon images (from Alexa Fluor 594 fluorescence) of a visual cortical layer 2/3 neuron. The tip of the patch pipette (green) is in contact with the cell body. Right panel, top view of the recording chamber mounted on the skull, the patch pipette and the screen displaying visual stimuli. A black paper cone to prevent stray light is placed between the eye and the screen.

High-speed two-photon laser scanning microscope setup We use a home-built setup that is derived from the designs of Parker/Sanderson (http://parkerlab.bio.uci.edu/microscopy_construction/build_your_own_twophoton_microscope.htm). Excitation light is provided by a titanium-sapphire pulsing laser at a wavelength of 800 nm. A resonant scanner unit is mounted on a commercial microscope chassis. Emitted photons are split into two channels and detected by photomultiplier tubes, i.e., into a 'green' channel for OGB-1 fluorescence (480–560 nm) and a 'red' channel for Alexa Fluor 594 fluorescence (580–680 nm). Standard scanning speed is 30 Hz for a pixel resolution of 480 × 400 or 60 Hz at a reduced frame of 480 × 180. This high scanning speed is beneficial, because it provides the information required for reducing heartbeat-related motion artifacts[16]. We use a long working distance, water immersion microscope objective. The starting trigger of image acquisition is synchronized with the patch-clamp recording and visual stimulation program. *Note*: Most two-photon microscopes equipped with standard galvanometric scanners can also be used for this protocol, because they allow, for smaller-sized frames, sampling rates that are similar to those used for our experiments. In addition, single line-scan imaging may be used, although scanning along the dendritic axis may pose alignment problems because of the unavoidable motions of the brain tissue under *in vivo* recording conditions.

Visual stimulation Visual stimuli are generated by a program written in Matlab with the 'Psychtoolbox' add-on package (http://psychtoolbox.org/wikka.php?wakka=HomePage). A video projector (pixel resolution 1,280 × 1,024; refresh rate 75 Hz) casts the stimuli onto a screen placed at 30 cm from the right eye, covering ~80° × 60° of the visual field. A black paper cone placed between the eye and the screen is used to prevent stray light. Each trial of visual stimulation sequence starts with a gray screen (mean luminance of black and white) for 4 s, followed by eight periods of square-wave grating stimulation, corresponding to eight directions with an angular interval of 45°. Each of these periods consists of a stationary pre-phase of 2 s followed by a drifting stimulation phase for 1 s (spatial frequency 0.03 cycles per degree, drifting speed 1 cycle per s, black/white contrast 80%, mean luminance 3.7 cd m^{-2}).

PROCEDURE

Surgery ● TIMING 60–80 min

1| Anesthetize the mouse with 1.5% isoflurane (vol/vol, in pure O_2).

2| Place the mouse onto a warming plate (38 °C).

3| Gently cover both eyes with eye protecting cream.

4| Inject ~50 µl of lidocaine hydrochloride s.c. above the skull.

5| Using fine scissors, remove the hair and skin above the skull from an area of ~1 cm in diameter above the visual cortex (left hemisphere).

6| Glue the recording chamber (see **Fig. 1**) onto the exposed skull with cyanoacrylate glue.

7| Perform a small rectangular craniotomy (~1 mm × 0.8 mm) above the monocular region of primary visual cortex (left hemisphere), centered at 2.2 mm lateral to the midline and 4 mm posterior to bregma. Be very careful not to damage the cortex.
▲ **CRITICAL STEP** Keep the dura as intact as possible. An intact dura helps to prevent motion artifacts.

8| Gently clean the exposed cortex with ACSF to remove blood. Usually, craniotomy-induced bleeding stops within 2–3 min.

9| Cover the exposed cortex with agar. First, remove the ACSF from the recording chamber and then put a drop of agarose solution (~38 °C) on top of the exposed cortex and the surrounding skull. Wait until the agarose solution solidifies and then fill the chamber with fresh ACSF.
▲ **CRITICAL STEP** The agar should form a compact sheet with a thickness of ~1 to 2 mm. For best results, avoid any cracks in the agar.

Preparation for recording ● TIMING 30–40 min

10| Transfer the animal to the recording setup on a warming plate.

11| Start perfusion of the recording chamber with warmed (37 °C) and gassed ACSF.

12| Reduce isoflurane concentration to 1.2% (vol/vol).

13| Remove the protecting cream from the right eye carefully.

14| Mount the black paper cone (for preventing stray light) between the eye and the screen (see EQUIPMENT SETUP and **Fig. 1**).
■ **PAUSE POINT** In practice, this is the only time point for the experimenter to take a break (~30 min; the subsequent steps (Steps 15–41) must be completed consecutively).

15| Prepare patch pipettes and pipette solution (see REAGENT SETUP for details). Pipette resistance should be 6–7 MΩ.

Shadow patching ● TIMING **10–15 min**

16| Move the patch pipette, under visual control, vertically through the agar until it reaches the dura in an area devoid of large blood vessels.

17| Switch to the two-photon imaging mode of visualization, and monitor the pipette in the 'red' channel for Alexa Fluor 594 fluorescence.
▲ CRITICAL STEP Until Step 38, use two-photon visualization only when needed. Keep laser power as low as possible to prevent photo-damage of the tissue.

18| Verify that the pipette is not occluded by regularly applying brief and gentle pressure pulses (20–80 mbar). Proceed to the next step if the pipette is free, as indicated by pressure-induced small clouds of fluorescence at the tip. Otherwise, use a new pipette and restart the procedure from Step 16.

19| Penetrate the dura by axially moving the pipette stepwise (~50 μm).

20| Test again for pipette occlusion; if the tip is free, proceed to the next step. Otherwise, retract the pipette back to the surface while applying larger pressure pulses (100–200 mbar), and then repeat Step 19.
▲ CRITICAL STEP Do not blow out too much of the pipette solution and keep the pressure pulse short (<1 s).
No more than four or five repetitions with a given pipette are recommended.
? TROUBLESHOOTING

21| Navigate through the cortex to layer 2/3: advance the pipette slowly with the guidance of two-photon imaging, and avoid hitting blood vessels and other cell bodies by small lateral movements until the desired depth is reached (150–200 μm).
▲ CRITICAL STEP During the intracortical navigation, periodically blow out small amounts of the fluorescent solution from the pipette just enough to see the shadows of cell bodies.
? TROUBLESHOOTING

22| Approach the soma of the closest layer 2/3 neuron from the side. Zoom in (two or three times) until the tip of the pipette and the edge of the cell body become clearly discernable.

23| Apply pressure (50–100 mbar) and advance the pipette tip into the center of cell body. If a 'pit' is seen on the cell body, proceed immediately to the next step; otherwise, retract the pipette and repeat from Step 22.

24| Apply constant negative pressure (−150 mbar) until the seal resistance goes up to >150 MΩ and then release the pressure. Wait until a GΩ seal contact is formed between the tip of the patch pipette and the somatic membrane.
▲ CRITICAL STEP In case of failure, slowly retract the pipette completely out of the brain and restart from Step 16. However, after five or six failures, the residual extracellular fluorescence becomes high and it is recommended to restart with a new cortical region.
? TROUBLESHOOTING

25| After the formation of the GΩ seal is complete, reposition the tip to its initial position on the side of cell body.

26| Compensate the pipette capacitance.

27| Establish whole-cell recording mode by applying brief negative pressure pulses in increasing order (from −20 mbar onward) until the patched membrane is ruptured.

28| Compensate the cell capacitance and the series resistance.

Dye loading and whole-cell recording ● TIMING **20–40 min**

29| Reduce isoflurane concentration to ~0.8% (vol/vol), the threshold value for anesthesia (respiration rate in the range of 100–130 b.p.m.).

30| Check that series resistance is <40 MΩ and leak current amplitude is <200 pA. If these criteria are not fulfilled, restart from Step 16.
? TROUBLESHOOTING

31| Keep the neuron at resting membrane potential (approximately −65 mV) and switch to the current clamp recording mode.

32| Start the sequence of visual stimuli and record changes in membrane potential.

33| Repeat Step 32 for at least ten trials.

34| Check the pipette position by two-photon visualization and, if necessary, correct for drifts.

35| Check dye loading by two-photon visualization. If, usually after 15–20 min, the contrast between dendrites and background is sufficient (>fivefold) in the 'green' channel, proceed to the next step.
▲ **CRITICAL STEP** It takes 20–40 min for the dye to reach full equilibrium in the dendrites of the cell, depending on the series resistance. If the imaging contrast is still not good enough after troubleshooting, restart from Step 16.
? TROUBLESHOOTING

Dendritic calcium imaging ● TIMING 40–120 min

36| Hyperpolarize the neuron below action potential threshold by holding a negative clamp current and continue as indicated in **Figure 2a**.
▲ **CRITICAL STEP** The required holding current may change over the course of recordings; therefore, adjust it such that the up-state membrane potential is just below action potential threshold (approximately −50 mV).

37| Search for a field of view with many dendrites (**Fig. 2b**).
▲ **CRITICAL STEP** The maximal time and the quality of imaging strongly depend on previous steps (Steps 7, 9, 20, 21 and 24). Within the time of whole-cell recording conditions, several focal planes can be imaged, depending on the purpose of the study. We recommend recording only one neuron per cortical region to avoid the overlap of dendrites belonging to different neurons.
? TROUBLESHOOTING

38| Trigger the visual stimuli presentation, whole-cell recording and two-photon calcium imaging simultaneously.
▲ **CRITICAL STEP** The laser power can be increased to optimize the optical signals.

39| Check and, if necessary, correct slow drifts of the focal plane, then repeat Step 38 for six to ten trials.

40| Move to another area (**Fig. 2c**) and repeat Steps 37–39.
▲ **CRITICAL STEP** Checking the pipette position regularly helps to maintain the quality of whole-cell recordings. Note that phototoxic damage is indicated by local swellings of the illuminated dendrites. We recommend stopping the loop of calcium imaging recordings after three or four cycles (Steps 37–40) and proceeding to the next step.

41| Acquire a *z*-stack of images of the entire neuron (**Fig. 2d**).
▲ **CRITICAL STEP** Do not retract the pipette before this step is completed, even if the whole-cell configuration is lost. Retraction of the pipette may damage the dendrite-containing tissue.

Analysis of dendritic calcium signals and identification of hotspots ● TIMING Hours to days

42| Create an image of ~500 consecutive frames (from OGB-1 'green' channel) and adjust the brightness and the contrast such that the dendrites can be clearly seen, as in **Figure 3a**.

43| Define ROIs that cover all dendrites in the focal plane. Note that **Figure 3b** only shows ROIs for a part of the dendrites.

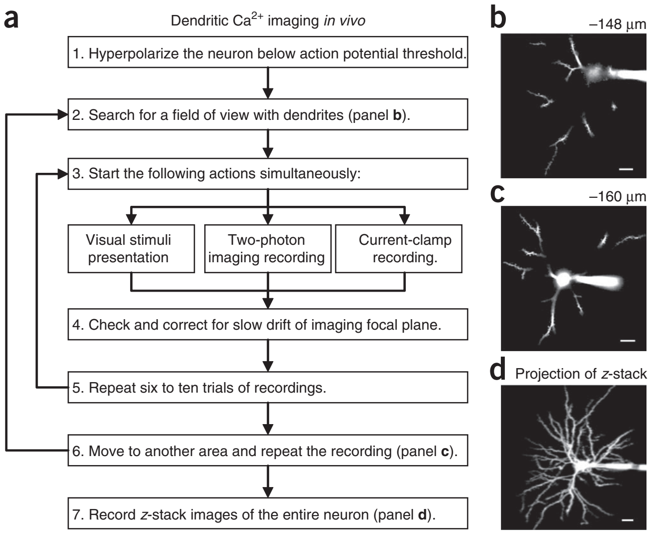

Figure 2 | *In vivo* two-photon imaging of visually evoked dendritic calcium signals. (**a**) Flow diagram showing the different steps of the procedure. (**b**,**c**) Two-photon images (each an average of 500 frames) of a layer 2/3 neuron obtained at different depths under the cortical surface, as indicated. Images were acquired in the 'green channel' for OGB-1 fluorescence. Note the patch pipette on the right side. (**d**) Projection of *z*-stack of two-photon images (Alexa Fluor 594 fluorescence) of the same neuron. Scale bars for **b**–**d**, 10 µm.

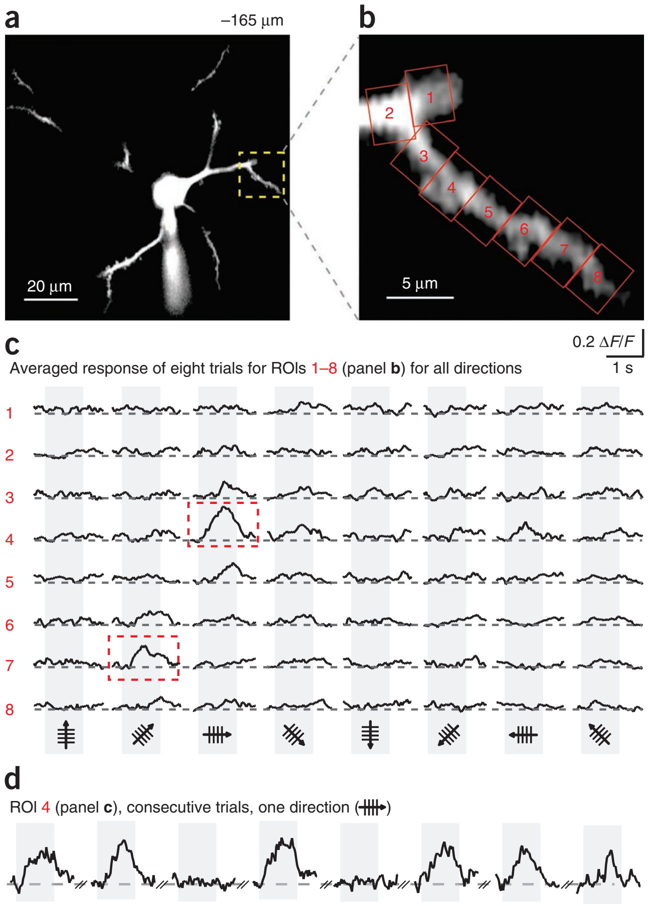

Figure 3 | Extraction of local dendritic calcium transients from two-photon images. (**a**) Image of a focal plane of layer 2/3 obtained at 165 μm below the cortical surface. The image (OGB-1 fluorescence, average of 500 frames) shows a two-photon section through the cell body and dendrites of a neuron, the recording patch pipette and a dashed frame containing a dendritic segment of interest. (**b**) Higher magnification image of the dendritic segment (indicated in panel **a**) covered by eight regions of interest (ROIs), each 3 × 4 μm, used to extract visually evoked local dendritic calcium transients. (**c**) Calcium transients (averages of eight consecutive trials) for all eight ROIs (marked in red) shown in **b**, recorded during the presentation of eight directions of drifting gratings. Two local dendritic calcium transients are highlighted by dashed red frames. The vertical gray bands indicate the time of visual stimulation by the directions schematically indicated at the bottom. (**d**) Consecutive single calcium transients (n = 8) evoked by one direction (as indicated) and recorded in ROI 4 (see **b** and **c**).

44| Calculate changes in fluorescence from each ROI. Refer to **Box 1** for a detailed algorithm.

45| Repeat Steps 42 and 44 for all trials recorded in a focal plane.

▲ **CRITICAL STEP** Use the same set of ROIs (as defined in Step 43) for all trials of a given imaged focal plane. In case of small intertrial image drifts, readjust the position of the ROIs. We recommend discarding trials with large image drifts (>1 μm).

46| Calculate the average calcium signal–corresponding changes in fluorescence from each ROI for each stimulus condition (each direction of drifting gratings) over all recorded trials. Averaged traces are shown in **Figure 3c**.

BOX 1 | CALCULATION OF CALCIUM SIGNALS ($\Delta F/F$) FROM A REGION OF INTEREST

1. Calculate the mean fluorescence $F(t)$ of a region of interest (ROI) for each time point t

$$F(t)=\frac{1}{N}\sum_{\mathrm{ROI}} f_i(t),$$ where N is the number of pixels in the ROI, $f_i(t)$ is the value of pixel i at time t.

2. Calculate the time-dependent baseline $F_0(t)$

For each time point t, taken as the minimum value of smoothed $F(t)$ during a time window before t.

$$F_0(t)=\{\min(\overline{F(x)})\mid (t-\tau_2)<x<t\}$$

where $$\overline{F(x)}=\frac{1}{\tau_1}\int_{x-\tau_1/2}^{x+\tau_1/2}F(\tau)\mathrm{d}\tau$$

3. Calculate the relative change of fluorescence signal $R(t)$ from $F(t)$ and $F_0(t)$

$$R(t)=\frac{F(t)-F_0(t)}{F_0(t)}$$

4. Apply noise filtering (exponentially weighted moving average) to get final result $\Delta F/F(t)$

$$\Delta F/F(t)=\frac{\int_0^t R(t-\tau)\cdot w(\tau)\mathrm{d}\tau}{\int_0^t w(\tau)\mathrm{d}\tau}$$

where

$$w(\tau)=\exp\left\{-\frac{|\tau|}{\tau_0}\right\}$$

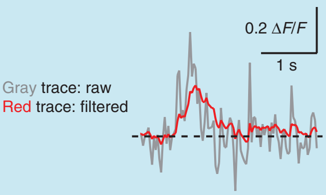

Notes:

1. Typically, effective filtering for 30 Hz imaging is achieved by the following parameters: τ_0 = 0.2 s, τ_1 = 0.75 s and τ_2 = 3 s.
2. This algorithm is robust against both the slow drifting of baseline signal and the fast oscillatory noise due to tissue pulsation, but it may alter the shape of calcium transient, depending largely on τ_0.

47| Identify the hotspots (outlined by red dashed boxes in **Fig. 3c**).
▲ CRITICAL STEP Hotspots need to be defined quantitatively (i.e., in terms of variation in signal amplitude) on the basis of the purpose of the study. We accepted a transient hotspot if its amplitude exceeded three times the standard deviation of the noise band.

48| Investigate detailed features of the hotspot signal. For example, determine the reliability of the response to visual stimuli (**Fig. 3d**) and the orientation and direction selectivity of the response[31].

49| Repeat Steps 42–48 for all the imaged focal planes.

? TROUBLESHOOTING

Troubleshooting advice can be found in **Table 1**.

TABLE 1 | Troubleshooting table.

Step	Problem	Possible reason	Solution
20	No spread of fluorescence	Pipette clogged	Retract the pipette from the dura and apply more pressure to the pipette or use a new pipette
21	Cannot see sharp shadows	A thick blood vessel is present above the imaged area	Navigate away from this area
		Too much dye is on the cortical surface (usually happens after many attempts)	Wait for ~30 min and start again from Step 16
24	Cannot achieve GΩ seal	Pipette tip is not clean	Use a new pipette. When navigating the pipette in the cortex, avoid large structures such as blood vessels or cell bodies
30, 35	Series resistance goes up (>40 MΩ)	Pipette tip is pushing too far into the cell body	First, correct the pipette position with two-photon imaging. If the resistance is still high, gently apply a transient negative pressure (10–50 mbar) in the pipette to open more of the patch membrane
	Whole-cell configuration lost after a short time (<1 h)	Movements of the cortical tissue, drift of the pipette	Restart from Step 16 to patch another cell
35	Background is too bright, dendrites cannot be clearly distinguished	Too much dye is spread out during the shadow-patching procedure (usually happens after many attempts)	Wait for a longer time before imaging. If the background is still not fading after ~30 min, start from Step 16 in another region
37	Motion artifacts, image is shaking too much	Proximity of big blood vessels, heartbeat pulsations	Choose dendrites that are far away from the blood vessels

● TIMING

Steps 1–9, Surgery: 60–80 min
Steps 10–15, Preparation for recording: 30–40 min
Steps 16–28, Shadow patching: 10–15 min
Steps 29–35, Dye loading and electrophysiology recording: 20–40 min
Steps 36–41, Dendritic calcium imaging: 40–120 min
Steps 42–49, Analysis: hours to days

ANTICIPATED RESULTS

Data analysis is required to reveal local dendritic calcium signals (‘hotspots’) evoked by drifting gratings. **Figure 3** illustrates the analysis procedure, as described in Steps 42–49 of the PROCEDURE.

The size and location of the ROIs can vary depending on the purpose of the study. Smaller ROIs give signals that have higher amplitude at the center of the hotspot and also greater noise. Here, we use 3 µm × 4 µm rectangular ROIs that were found to give the best signal-to-noise ratio in our recording conditions. The filtering algorithm (see **Box 1**) was used to reduce noise. Noise consists of normal Gaussian noise as well as a characteristic component at heartbeat frequency (~8 Hz).

The parameters for signal filtering (**Box 1**) were determined empirically to provide good signal preservation as well as effective noise suppression. However, if there is too much movement during imaging recordings (vibration amplitude > 1 µm), the motion artifacts will greatly interfere with the calcium signals and the filter will not help.

ACKNOWLEDGMENTS We are grateful to Y. Kovalchuk for his help in the initial experiments. This study was supported by grants from Deutsche Forschungsgemeinschaft (DFG) to A.K. and from the Friedrich Schiedel Foundation. A.K. is a Carl von Linde Senior Fellow of the Institute for Advanced Study of the Technische Universität München. H.J. and N.L.R. were supported by the DFG (IRTG 1373).

AUTHOR CONTRIBUTIONS H.J., N.L.R., X.C. and A.K. performed the experiments and the analysis. H.J. developed the program for data analysis. A.K. wrote the paper together with H.J., N.L.R. and X.C.

COMPETING FINANCIAL INTERESTS The authors declare no competing financial interests.

1. London, M. & Häusser, M. Dendritic computation. *Annu. Rev. Neurosci.* **28**, 503–532 (2005).
2. Johnston, D. & Narayanan, R. Active dendrites: colorful wings of the mysterious butterflies. *Trends. Neurosci.* **31**, 309–316 (2008).
3. Larkum, M.E. & Nevian, T. Synaptic clustering by dendritic signalling mechanisms. *Curr. Opin. Neurobiol.* **18**, 321–331 (2008).
4. Ohki, K. & Reid, R.C. Specificity and randomness in the visual cortex. *Curr. Opin. Neurobiol.* **17**, 401–407 (2007).
5. Bloodgood, B.L. & Sabatini, B.L. Ca^{2+} signaling in dendritic spines. *Curr. Opin. Neurobiol.* **17**, 345–351 (2007).
6. Yuste, R. & Denk, W. Dendritic spines as basic functional units of neuronal integration. *Nature* **375**, 682–684 (1995).
7. Müller, W. & Connor, J.A. Dendritic spines as individual neuronal compartments for synaptic Ca^{2+} responses. *Nature* **354**, 73–76 (1991).
8. Eilers, J., Augustine, G.J. & Konnerth, A. Subthreshold synaptic Ca^{2+} signalling in fine dendrites and spines of cerebellar Purkinje neurons. *Nature* **373**, 155–158 (1995).
9. Häusser, M. & Mel, B. Dendrites: bug or feature? *Curr. Opin. Neurobiol.* **13**, 372–383 (2003).
10. Svoboda, K., Denk, W., Kleinfeld, D. & Tank, D.W. *In vivo* dendritic calcium dynamics in neocortical pyramidal neurons. *Nature* **385**, 161–165 (1997).
11. Helmchen, F., Svoboda, K., Denk, W. & Tank, D.W. *In vivo* dendritic calcium dynamics in deep-layer cortical pyramidal neurons. *Nat. Neurosci.* **2**, 989–996 (1999).
12. Murayama, M. *et al.* Dendritic encoding of sensory stimuli controlled by deep cortical interneurons. *Nature* **457**, 1137–1141 (2009).
13. Waters, J., Larkum, M., Sakmann, B. & Helmchen, F. Supralinear Ca^{2+} influx into dendritic tufts of layer 2/3 neocortical pyramidal neurons *in vitro* and *in vivo*. *J. Neurosci.* **23**, 8558–8567 (2003).
14. Waters, J. & Helmchen, F. Boosting of action potential backpropagation by neocortical network activity *in vivo*. *J. Neurosci.* **24**, 11127–11136 (2004).
15. Svoboda, K., Helmchen, F., Denk, W. & Tank, D.W. Spread of dendritic excitation in layer 2/3 pyramidal neurons in rat barrel cortex *in vivo*. *Nat. Neurosci.* **2**, 65–73 (1999).
16. Helmchen, F. & Waters, J. Ca^{2+} imaging in the mammalian brain *in vivo*. *Eur. J. Pharmacol.* **447**, 119–129 (2002).
17. Jia, H., Rochefort, N.L., Chen, X. & Konnerth, A. Dendritic organization of sensory input to cortical neurons *in vivo*. *Nature* **464**, 1307–1312 (2010).
18. Kitamura, K., Judkewitz, B., Kano, M., Denk, W. & Häusser, M. Targeted patch-clamp recordings and single-cell electroporation of unlabeled neurons *in vivo*. *Nat. Methods* **5**, 61–67 (2008).
19. Bollmann, J.H. & Engert, F. Subcellular topography of visually driven dendritic activity in the vertebrate visual system. *Neuron* **61**, 895–905 (2009).
20. Margrie, T.W., Brecht, M. & Sakmann, B. *In vivo*, low-resistance, whole-cell recordings from neurons in the anaesthetized and awake mammalian brain. *Pflugers Arch.* **444**, 491–498 (2002).
21. Nevian, T. & Helmchen, F. Calcium indicator loading of neurons using single-cell electroporation. *Pflugers Arch.* **454**, 675–688 (2007).
22. Nagayama, S. *et al. In vivo* simultaneous tracing and Ca^{2+} imaging of local neuronal circuits. *Neuron* **53**, 789–803 (2007).
23. Theer, P., Hasan, M.T. & Denk, W. Two-photon imaging to a depth of 1000 microm in living brains by use of a Ti:Al2O3 regenerative amplifier. *Opt. Lett.* **28**, 1022–1024 (2003).
24. Jung, J.C. & Schnitzer, M.J. Multiphoton endoscopy. *Opt. Lett.* **28**, 902–904 (2003).
25. Mank, M. & Griesbeck, O. Genetically encoded calcium indicators. *Chem. Rev.* **108**, 1550–1564 (2008).
26. Hires, S.A., Tian, L. & Looger, L.L. Reporting neural activity with genetically encoded calcium indicators. *Brain Cell. Biol.* **36**, 69–86 (2008).
27. Miyawaki, A. Fluorescence imaging of physiological activity in complex systems using GFP-based probes. *Curr. Opin. Neurobiol.* **13**, 591–596 (2003).
28. Lutcke, H. *et al.* Optical recording of neuronal activity with a genetically-encoded calcium indicator in anesthetized and freely moving mice. *Front. Neural. Circuits* **4**, 9 (2010).
29. Tian, L. *et al.* Imaging neural activity in worms, flies and mice with improved GCaMP calcium indicators. *Nat. Methods* **6**, 875–881 (2009).
30. Rochefort, N.L. & Konnerth, A. Genetically encoded Ca^{2+} sensors come of age. *Nat. Methods* **5**, 761–762 (2008).
31. Niell, C.M. & Stryker, M.P. Highly selective receptive fields in mouse visual cortex. *J. Neurosci.* **28**, 7520–7536 (2008).

Project V

Functional mapping of single spines in cortical neurons *in vivo*

(Published in **Nature**, 2011, 475: 501-5) doi:10.1038/nature10193

Functional mapping of single spines in cortical neurons *in vivo*

Xiaowei Chen[1]*, Ulrich Leischner[1]*, Nathalie L. Rochefort[1], Israel Nelken[2] & Arthur Konnerth[1]

The individual functional properties and spatial arrangement of afferent synaptic inputs on dendrites have a critical role in the processing of information by neurons in the mammalian brain[1–4]. Although recent work has identified visually-evoked local dendritic calcium signals in the rodent visual cortex[5], sensory-evoked signalling on the level of dendritic spines, corresponding to individual afferent excitatory synapses, remains unexplored[6]. Here we used a new variant of high-resolution two-photon imaging[7] to detect sensory-evoked calcium transients in single dendritic spines of mouse cortical neurons *in vivo*. Calcium signals evoked by sound stimulation required the activation of NMDA (*N*-methyl-D-aspartate) receptors. Active spines are widely distributed on basal and apical dendrites and pure-tone stimulation at different frequencies revealed both narrowly and widely tuned spines. Notably, spines tuned for different frequencies were highly interspersed on the same dendrites: even neighbouring spines were mostly tuned to different frequencies. Thus, our results demonstrate that NMDA-receptor-dependent single-spine synaptic inputs to the same dendrite are highly heterogeneous. Furthermore, our study opens the way for *in vivo* mapping of functionally defined afferent sensory inputs with single-synapse resolution.

A newly developed high-speed two-photon microscopy device (see Methods and Supplementary Fig. 1), allowing image acquisition rates of more than 1,000 frames per second, was used to record sound-stimulus-evoked calcium transients in single spines of mouse auditory cortical neurons *in vivo*. This apparatus allowed the implementation of a very sensitive fluorescence recording procedure, which we refer to as low-power temporal oversampling (LOTOS). LOTOS-based imaging comprises the acquisition of images at high frame rates, short pixel dwell-times and low intensities of the exciting laser beam (see Supplementary Fig. 2). Offline, the sequences of images are down-sampled 10–12-fold, revealing robust calcium transients in dendritic spines (see for example Fig. 1 and Supplementary Movie 1). LOTOS is suited for the registration of multiple trials of stimulus-evoked single-spine calcium signals during recording periods of up to 300–350 s. We assume that LOTOS-based spine imaging benefits from a combination of fluorescence-gain, resulting from a reduction in triplet-state formation[8], and reduced phototoxic damage[9] when using high-frequency stimulation at low-power excitation.

To explore *in vivo* single-spine calcium signalling in layer 2/3 pyramidal neurons of the mouse auditory cortex (see identification of pyramidal neurons in Supplementary Fig. 3), we used the 'shadow patching' procedure[5,10] (Fig. 1a, b). Recordings of subthreshold sound-stimulation-evoked responses were obtained from neurons that were actively hyperpolarized to membrane potentials ranging from −70 mV to −77 mV (refs 5, 11), or from non-firing neurons with low resting membrane potentials (−71 mV to −76 mV) (see Methods and Supplementary Table 1). The somatically recorded, sound-evoked depolarizations had latencies in the range of 10–50 ms (27.7 ± 2.2 ms; $n = 16$ neurons) (Supplementary Figs 4 and 5), consistent with previous studies[12–14]. Figure 1c shows that a single 100-ms burst of broadband noise produced large calcium transients in a subset of 'active' spines (S1 and S3 in Fig. 1c) (mean success rate 58 ± 3%, 10 neurons, Fig. 1d), but that this noise produced no calcium transients or only very small ones in other spines that were functionally silent (S2 in Fig. 1c; see also Supplementary Fig. 6 and Supplementary Movie 1). Back-propagating action potentials, which occurred during short periods of membrane depolarization, invaded the dendrites in this type of neuron, as noticed previously[15], and were highly effective at producing calcium transients in all spines (Fig. 1c, right-most column). The calcium signals in spines had rapid rise times and slow decay times, similar to the synaptically evoked calcium transients that were previously recorded in spines of cortical or hippocampal neurons in brain slices[3,16–18]. A detailed inspection of calcium signalling in the dendritic shaft, involving a fine segmentation with a step size of 1 µm (Supplementary Fig. 6b), revealed the presence of active dendritic microregions (1–5 µm) in the immediate neighbourhood of the active spines (Fig. 1c and Supplementary Fig. 6d). The calcium transients in the active dendritic regions (labelled 'D' in Fig. 1) had much smaller amplitudes than those detected in the active spines (Fig. 1c, e). Furthermore, as previously reported for recordings that were made in brain slices[19], we found that a fraction of active spines (66 of 178 spines in 19 dendrites, 10 neurons) showed calcium signals that were entirely restricted to the spines, without an associated calcium signal in the adjacent dendritic shafts (see for example Supplementary Fig. 6e–g). The smaller amplitude or even absence of the dendritic-shaft calcium signals, their association with dendritic spines and their restricted spatial extent indicate that they are generated by calcium efflux from the active spines[17,19]. The synaptic origin of the calcium transients evoked by auditory stimulation was demonstrated by the intracellular application of MK-801, a drug that effectively blocks NMDA receptors in cortical neurons both extracellularly and intracellularly[20,21]. The calcium transients in spines may result from calcium entry through NMDA receptor channels (for example, ref. 17), with a possible contribution of other mechanisms such as the activation of voltage-gated calcium channels by synaptically mediated depolarization[22]. We found that MK-801 abolished sound-evoked calcium transients in both spines and dendritic shafts, but did not abolish calcium transients that were evoked by back-propagating action potentials (Fig. 1f, g).

The level of sound strongly modulates cortical responses to sounds[23–25]. To explore the spatial organization of synaptic inputs that are activated by sound stimuli of various intensities, we imaged the dendritic tree of layer 2/3 cortical neurons at different depths under the cortical surface. Figure 2a shows results obtained in five dendritic segments of such a neuron. Broadband noise stimuli delivered at a sound level of 40 dB attenuation (−40 dB) did not activate a single spine (Fig. 2a). At a higher level of sound intensity, −20 dB, two or three spines were activated in each of the dendritic segments. At the highest sound level, 0 dB, the density of active spines increased further, resulting in 3–6 active spines per recorded segment (Fig. 2a). Overall,

---

[1] Institute of Neuroscience and Center for Integrated Protein Science, Technical University Munich, Biedersteinerstrasse 29, 80802 Munich, Germany. [2] Department of Neurobiology, Silberman Institute of Life Sciences and the Edmond and Lily Safra Center for Brain Sciences, Hebrew University, Jerusalem 91904, Israel.

*These authors contributed equally to this work.

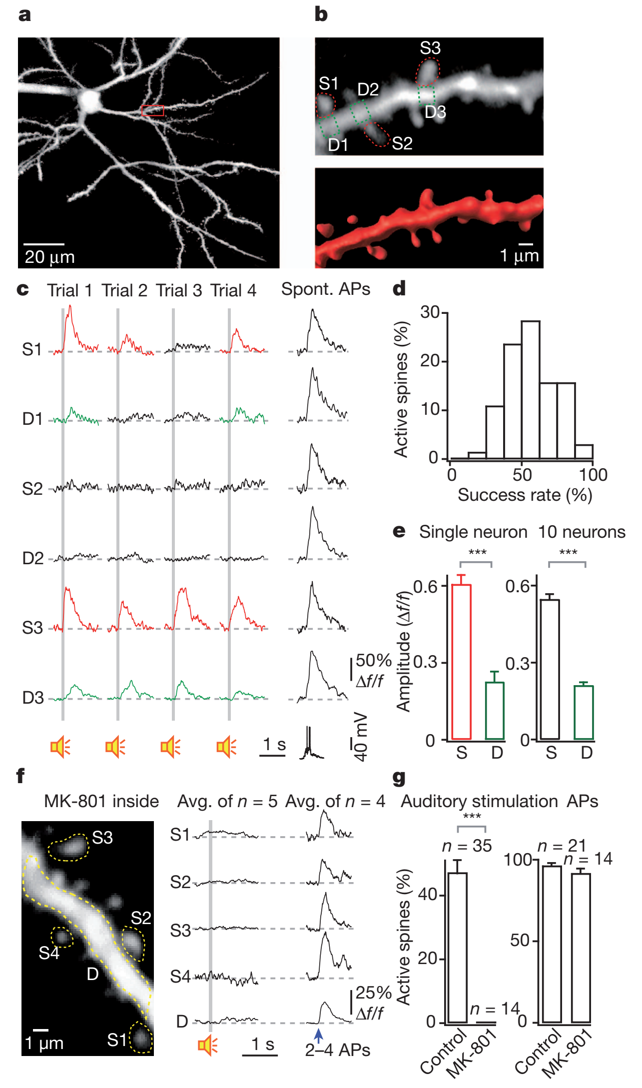

Figure 1 | Calcium signals in dendritic spines of cortical neurons *in vivo*. **a**, z-projection of a layer 2/3 neuron of the primary auditory cortex, labelled with OGB-1. The red rectangle indicates the area magnified in **b**. **b**, Upper panel: image at high magnification of the dendritic segment indicated in **a** (average of 6,250 frames). Three spines of interest (S1–S3) and the adjacent dendritic shaft regions (D1–D3) are indicated by dashed lines. Lower panel: three-dimensional image reconstruction of the dendritic segment. **c**, Subthreshold calcium transients evoked by auditory stimulation in spines (red) and corresponding dendritic shaft regions (green), as indicated in **b**. Four consecutive trials of auditory-stimulation-evoked subthreshold calcium transients, followed by an action-potential-evoked calcium transient (Spont. APs, spontaneous action potentials, are shown). The spontaneous action potentials occurred while the neuron was at resting membrane potential (see Supplementary Table 1). **d**, Reliability of auditory-evoked calcium responses in spines, calculated for each active spine during seven consecutive trials (broadband noise, 0 dB attenuation) ($n = 178$ spines, 10 neurons). **e**, Mean amplitude of auditory-evoked calcium responses in active spines (S) and active dendritic shafts (D). Left panel: data from the neuron shown in **a**–**c**. Right panel: data from ten neurons ($n = 178$ spines, $n = 142$ dendritic shafts). **f**, Left panel: image of a dendritic segment (average of 6,250 frames). Right panel: average (Avg.) calcium signals in the spines (S1–S4) and dendritic shaft (D) indicated in the left panel, in response to broadband noise and to action potentials (APs) in the presence of MK-801 (1 mM). Action potentials (2–4) were evoked by brief depolarizing pulses. **g**, Summary of MK-801 experiments. The fraction of active spines per dendrite was calculated by normalizing the number of active spines to the number of all spines. The number of dendrites for each condition is indicated on the top of each column. Unpaired t-tests, ***, $P < 0.001$. Error bars show s.e.m. Grey bars in **c** and **f** indicate sound stimulation (broadband noise, 100 ms duration, 0 dB attenuation).

at 0 dB attenuation we encountered 27 ± 3 active spines per 100-μm dendrite length ($n = 18$ dendrites from 10 neurons). In this neuron (Fig. 2a, b), as well as in all ten neurons tested (Fig. 2c), we found that both the number of active spines and the somatic depolarization increased with sound intensity (Fig. 2c). These results indicate that a gradual recruitment of spines that are widely distributed on apical and basal dendrites underlies the effects of sound intensity on the responses of layer 2/3 neurons[25].

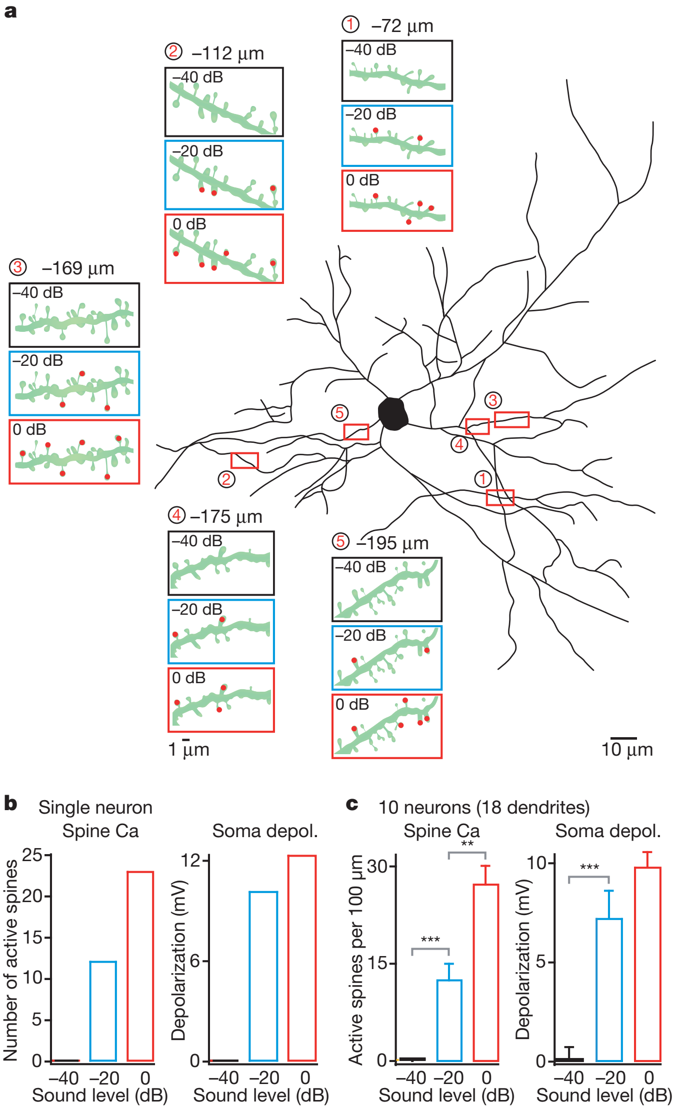

Figure 2 | Widespread dendritic distribution and sound-intensity-dependent recruitment of active spines. **a**, Reconstructed neuron with dendritic recording sites marked and numbered, surrounded by corresponding insets indicating spine activity. Insets illustrate the corresponding dendritic segments at high magnification (green), indicating with red dots the spines that were activated at the three sound intensities tested: −40 dB (black frame), −20 dB (blue) and 0 dB (red). The depth (under the cortical surface) of the imaged dendritic segments is indicated above each inset. The soma of the neuron was located −192 μm under the cortical surface. This is the same neuron as that shown in Fig. 1a–c. **b**, Left panel: total number of active spines (Spine Ca) in the five dendritic segments shown in panel **a** for the three sound intensities. Right panel: corresponding amplitude of somatically recorded depolarization (Soma depol.) in this neuron. **c**, Summary of the average density of active spines (number of active spines per dendritic length, left panel) and the corresponding somatically recorded depolarizations (right panel) from ten neurons (18 dendrites) for the three sound intensities. The length of each imaged dendritic segment was normalized to 100 μm. Unpaired t-tests, **, $P < 0.01$; ***, $P < 0.001$. Error bars show s.e.m.

On the basis of recent work in brain slices, it had been proposed that neighbouring synapses on a dendrite may transmit similar and related information to the postsynaptic cell[26]. For auditory cortical neurons, this may mean that synapses coding for similar frequencies are clustered on the same dendrite. To study the frequency-tuning properties of individual spines *in vivo*, we delivered pure tone pips over a wide range of frequencies at 0 dB attenuation (for details see Methods) in conditions of subthreshold membrane depolarization (Supplementary Fig. 7). Figure 3a shows an experiment in which two closely located spines on a dendrite had notably different tuning properties. Auditory stimulation produced calcium transients in spine S1 only at a frequency of 29.7 kHz (Fig. 3a, b, top), whereas spine S2 responded with marked calcium transients to stimuli delivered at five sequential frequencies, ranging from 4.9 kHz to 16.3 kHz (Fig. 3a, c, top). We defined spines as 'narrowly tuned' for frequency if they only responded to stimuli ranging within one octave. The bottom panels of Fig. 3b, c show the normalized tuning curves from narrowly and widely tuned spines, respectively. Overall, among all spines that responded to pure tones, 45% were narrowly tuned and 55% were widely tuned (Fig. 3d).

A notable feature of the spatial arrangement of spines on the same dendrite was their highly heterogeneous distribution. Figure 3e illustrates this heterogeneity by showing that neighbouring spines were mostly tuned to different frequencies (see also Supplementary Fig. 8). Overall, only 6% of the spines studied had a nearest neighbour with identical tuning properties ($n = 69$ neighbouring spines, 24 dendrites, 10 neurons). A less conservative way of quantifying the heterogeneity of distribution is to compare pairs of spines on the basis of their 'most effective frequency', namely the frequency that mediates, on average, the largest sound-evoked calcium transients in that spine. Even in this case, most spines (74%, $n = 69$ spines) had a nearest neighbour with a different most-effective frequency (Fig. 3f). Finally, we tested whether spines with the same most-effective frequency are spatially clustered, by plotting the dendritic distance against the frequency difference for pairs of neighbouring spines (Fig. 3g). We found that for all of the 1-octave ranges, the distances between pairs of spines were highly variable (Fig. 3g, rightmost columns), with no clear trend of clustering. Together, these results establish that there is a scattered distribution of spines with different frequency-tuning properties on the same dendrites.

Finally, we explored the dendritic arrangement of the synaptic inputs corresponding to the characteristic activation frequencies of neurons. We delivered auditory stimuli at different frequencies (ranging from 2 kHz to 40 kHz) and at different sound levels (−40 dB, −20 dB, −10 dB and 0 dB). A colour-coded map representation of such a recording is illustrated in Fig. 4a. We then extracted from these recordings the frequency depolarization response function for that neuron at different sound levels (Fig. 4b), to identify the 'best' frequency and an effective 'tail' frequency. Figure 4c–h shows the imaging results obtained. Stimulation with the best frequency (17.2 kHz in this case) reliably activated four spines (Fig. 4d), whereas tail-frequency stimulation caused the activation of two spines (Fig. 4e). With broadband noise stimulation (0–50 kHz), six additional spines were activated (Fig. 4f), leading to the dense pattern that we had observed in our initial recordings (Fig. 2). Figure 4h indicates that active spines generally

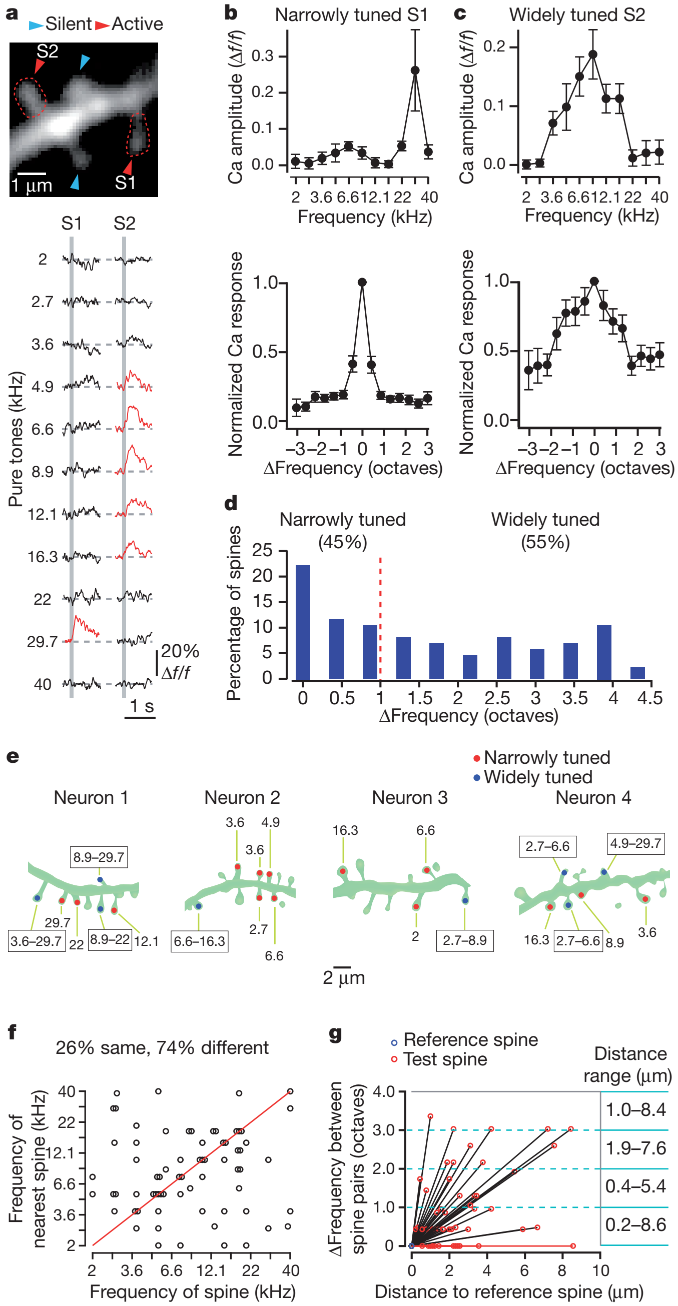

Figure 3 | Frequency tuning and heterogeneous distribution of individual active spines. **a**, Upper panel: two-photon image of a dendritic segment of a layer 2/3 neuron (average of 6,250 frames). Lower panel: calcium responses (average of five trials) from two spines (S) marked by red arrowheads in the upper panel, during 11 pure tones (from 2 kHz to 40 kHz at 0 dB attenuation). Two neighbouring spines indicated by blue arrowheads did not respond to any of the 11 pure tones. **b**, Upper panel: frequency tuning curve of the narrowly tuned spine S1 shown in **a**. Data points are the mean values of response amplitudes from five trials. Lower panel: average tuning curve normalized to the highest amplitude ($n = 38$ spines, 10 neurons). **c**, Upper panel: frequency tuning curve of the widely-tuned spine S2 shown in **a**. Lower panel: average tuning curve, normalized to the highest amplitude ($n = 46$ spines, 10 neurons). Error bars in **b** and **c** show s.e.m. **d**, Distribution of frequency tuning widths (ΔFrequency) of pure-tone-activated spines ($n = 84$ spines, 10 neurons). **e**, Heterogeneous distribution of pure-tone-activated spines along dendrites. Cartoons of dendritic segments from four neurons, with numbers indicating the effective frequencies for each active spine. Narrowly tuned and widely tuned spines are indicated by red and blue dots, respectively. The neurons correspond to, respectively, neuron 25, neuron 27, neuron 29 and neuron 30 in Supplementary Table 1. **f**, Plot of the most effective frequency of a given spine versus the most effective frequency of its nearest active spine (see Methods). Dots along the red line correspond to pairs of spines that had the same most-effective frequency ($n = 69$ pairs, 24 dendrites, 10 neurons). **g**, Plot of the distance between neighbouring active spines versus the difference between their respective most-effective frequencies. For each pair of spines, the reference spine (blue circle) was defined as the left spine and the test spine (red circle) was defined as the neighbouring active spine on the right. The measurements were performed sequentially from left to right in each dendrite ($n = 51$ pairs, 24 dendrites, 10 neurons). Dots along the red line correspond to spine pairs that had the same most-effective frequency. Numbers on the right indicate distance ranges between pairs of spines with a difference between their most effective frequencies of 0–1, 1–2, 2–3 and 3–4 octaves.

responded very reliably to the specific stimuli that activated them. In a minority of cases (see for example the spine at the bottom of Fig. 4f), individual spines produced calcium transients in response to tones of two different frequencies. Overall, 9 out of 166 spines responded to both the corresponding best and tail frequencies (Fig. 4i).

Our results represent, to our knowledge, the first demonstration of sensory-stimulation-evoked single-spine activity in mammalian cortical neurons *in vivo*. A recent study using conventional two-photon imaging in the mouse visual cortex[5] reported the existence of sensory-evoked local dendritic calcium hotspots. The question of whether sensory-evoked local calcium signalling occurred in single spines, dendritic shafts or small spino-dendritic compartments remained open[6]. Our two-photon imaging experiments involving the LOTOS procedure resolve this question and provide insights into the specific functional properties and spatial organization of auditory-stimulus-driven individual synaptic inputs to layer 2/3 cortical neurons. First, we found that the primary compartments of sensory-evoked signalling are dendritic spines, but not dendritic shafts. Second, we found that sound-stimulation-evoked calcium signalling in spines was entirely blocked by MK-801, indicating the involvement of NMDA receptors. These active spines were widely distributed throughout apical and basal dendrites. Although loud sound stimuli activated many spines on the same dendrite, bona fide calcium spikes (for example, refs 27–29) were not observed. Third, the results show a wide range of frequency tuning of individual spines, with a large proportion (45%) having a bandwidth of less than one octave, even at the relatively high sound level used here, in which the electrical tuning width of the neurons was a few octaves (Fig. 4 and Supplementary Fig. 7c). Notably, synaptic inputs to the same dendrite were found to be highly heterogeneous. This heterogeneity of synaptic inputs may be the underlying mechanism for the diversity of the response properties of single cortical neurons, even among nearby neurons, as was found recently[23,24] in experiments using two-photon calcium imaging of cortical networks[30].

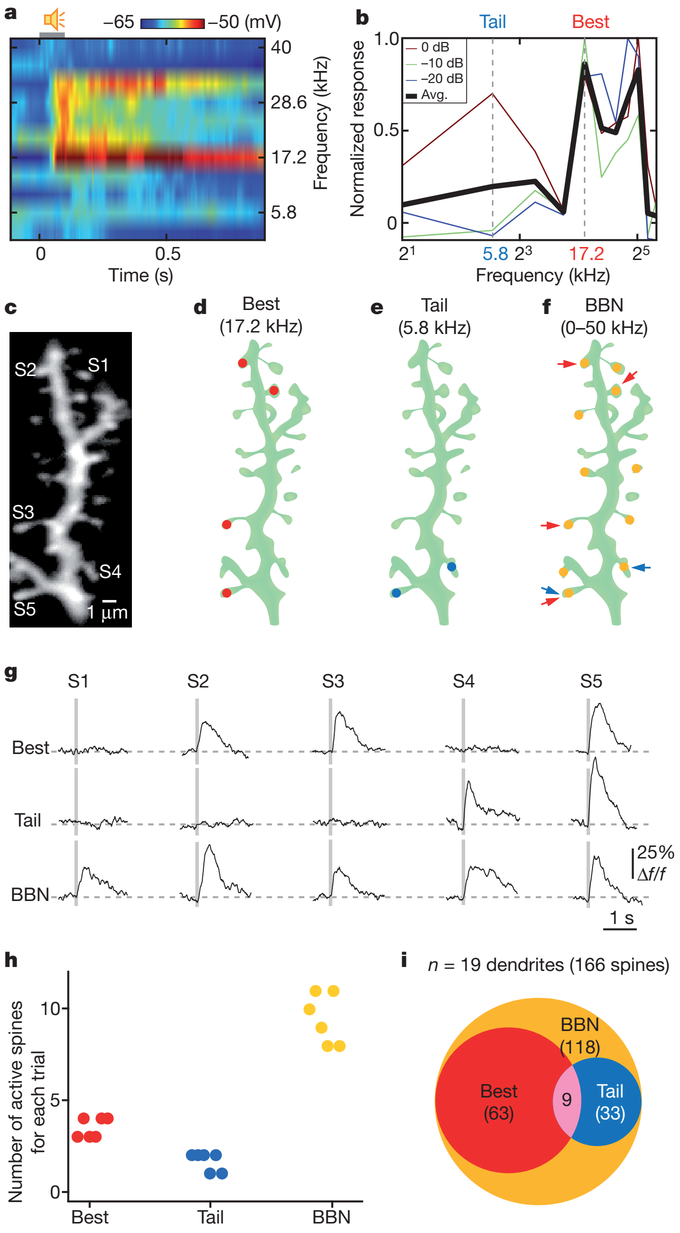

Figure 4 | Dendritic arrangement of spines activated by the best and tail frequencies of neurons. a, Colour map showing somatic electrical responses to pure tones at different frequencies (2 kHz to 40 kHz; 10 dB attenuation) in a layer 2/3 neuron. **b**, Summary of electrical responses to pure tones at different frequencies and at different sound levels (0–20 dB attenuations). Two dashed lines mark the tail frequency (light blue, 5.8 kHz) and best frequency (red, 17.2 kHz) used in the following panels. **c**, Two-photon image (average of 6,250 frames) of a dendrite from the same neuron as in panels **a** and **b**. **d**–**f**, Cartoons of the same dendrite as in **c**, showing the location of active spines during three different stimuli: best frequency (**d**, red), tail frequency (**e**, blue) and broadband noise (BBN, **f**, yellow). Red arrows and blue arrows point to spines tuned to the best frequency and the tail frequency, respectively. **g**, Examples of calcium transients in response to the best frequency, the tail frequency and broadband noise from five spines indicated in **c**. Each trace is an average of five individual trials. **h**, Plot of the number of active spines in the dendrite shown in **c**–**f** during six consecutive trials, in response to the best frequency, the tail frequency and broadband noise. **i**, Venn diagram summarizing the total number of active spines for each stimulus ($n = 19$ dendrites, 8 neurons, 166 visible spines). The number of active spines for each stimulus is indicated in each area. The pink area indicates the spines that responded to both best and tail frequencies.

METHODS SUMMARY

C57BL/6 mice were prepared for *in vivo* two-photon calcium imaging and whole-cell patch-clamp recordings under isoflurane anaesthesia, as described previously[5]. Layer 2/3 pyramidal neurons (Supplementary Fig. 3) of the primary auditory cortex were dialysed with a pipette solution containing the fluorescent calcium indicator Oregon green BAPTA-1 hexapotassium (OGB-1, 120 µM). Dendritic spines were imaged *in vivo* with a custom-built acousto-optic deflector (AOD)-based two-photon microscope (Supplementary Fig. 1). Auditory responses were evoked by 100-ms sound stimuli (10-ms rise/fall time) via an ES1 (Tucker-David Technologies) free-field speaker. For data analysis, the original image data that were acquired at a sampling rate of 1,000 frames s^{-1} were downsampled 10–12-fold (to 80–100 images s^{-1}). Calcium signals were expressed as relative fluorescence changes ($\Delta f/f$), corresponding to the mean fluorescence from all pixels within specified regions of interest. Regions of interest for imaging analyses of spine calcium signals were restricted to the clearly visible protrusions emanating laterally from the dendritic shaft (Supplementary Fig. 9). Because of the pulsation of the brain caused by the heartbeat, small fluctuations of fluorescent changes were observed (Supplementary Fig. 10). Therefore, we smoothed the traces with an exponentially averaging IIR filter (time constant, 80 ms) (Supplementary Fig. 4), as described previously[5,11]. Statistical analyses were performed using paired or unpaired Student's *t*-test as appropriate. $P < 0.05$ was considered significant.

Full Methods and any associated references are available in the online version of the paper at www.nature.com/nature.

Received 23 July 2010; accepted 11 May 2011.

1. London, M. & Häusser, M. Dendritic computation. *Annu. Rev. Neurosci.* **28,** 503–532 (2005).
2. Cash, S. & Yuste, R. Linear summation of excitatory inputs by CA1 pyramidal neurons. *Neuron* **22,** 383–394 (1999).
3. Sabatini, B. L., Maravall, M. & Svoboda, K. Ca^{2+} signaling in dendritic spines. *Curr. Opin. Neurobiol.* **11,** 349–356 (2001).
4. Yuste, R., Majewska, A. & Holthoff, K. From form to function: calcium compartmentalization in dendritic spines. *Nature Neurosci.* **3,** 653–659 (2000).

5. Jia, H., Rochefort, N. L., Chen, X. & Konnerth, A. Dendritic organization of sensory input to cortical neurons *in vivo. Nature* **464,** 1307–1312 (2010).
6. Branco, T. & Häusser, M. The single dendritic branch as a fundamental functional unit in the nervous system. *Curr. Opin. Neurobiol.* **20,** 494–502 (2010).
7. Denk, W., Strickler, J. H. & Webb, W. W. Two-photon laser scanning fluorescence microscopy. *Science* **248,** 73–76 (1990).
8. Donnert, G., Eggeling, C. & Hell, S. W. Major signal increase in fluorescence microscopy through dark-state relaxation. *Nature Methods* **4,** 81–86 (2007).
9. Ji, N., Magee, J. C. & Betzig, E. High-speed, low-photodamage nonlinear imaging using passive pulse splitters. *Nature Methods* **5,** 197–202 (2008).
10. Kitamura, K., Judkewitz, B., Kano, M., Denk, W. & Häusser, M. Targeted patch-clamp recordings and single-cell electroporation of unlabeled neurons *in vivo. Nature Methods* **5,** 61–67 (2008).
11. Jia, H., Rochefort, N. L., Chen, X. & Konnerth, A. *In vivo* two-photon imaging of sensory-evoked dendritic calcium signals in cortical neurons. *Nature Protocols* **6,** 28–35 (2011).
12. Chadderton, P., Agapiou, J. P., McAlpine, D. & Margrie, T. W. The synaptic representation of sound source location in auditory cortex. *J. Neurosci.* **29,** 14127–14135 (2009).
13. Linden, J. F., Liu, R. C., Sahani, M., Schreiner, C. E. & Merzenich, M. M. Spectrotemporal structure of receptive fields in areas AI and AAF of mouse auditory cortex. *J. Neurophysiol.* **90,** 2660–2675 (2003).
14. Scholl, B., Gao, X. & Wehr, M. Nonoverlapping sets of synapses drive on responses and off responses in auditory cortex. *Neuron* **65,** 412–421 (2010).
15. Waters, J., Larkum, M., Sakmann, B. & Helmchen, F. Supralinear Ca^{2+} influx into dendritic tufts of layer 2/3 neocortical pyramidal neurons *in vitro* and *in vivo. J. Neurosci.* **23,** 8558–8567 (2003).
16. Yuste, R. & Denk, W. Dendritic spines as basic functional units of neuronal integration. *Nature* **375,** 682–684 (1995).
17. Kovalchuk, Y., Eilers, J., Lisman, J. & Konnerth, A. NMDA receptor-mediated subthreshold Ca^{2+} signals in spines of hippocampal neurons. *J. Neurosci.* **20,** 1791–1799 (2000).
18. Mainen, Z. F., Malinow, R. & Svoboda, K. Synaptic calcium transients in single spines indicate that NMDA receptors are not saturated. *Nature* **399,** 151–155 (1999).
19. Noguchi, J., Matsuzaki, M., Ellis-Davies, G. C. & Kasai, H. Spine-neck geometry determines NMDA receptor-dependent Ca^{2+} signaling in dendrites. *Neuron* **46,** 609–622 (2005).
20. Berretta, N. & Jones, R. S. Tonic facilitation of glutamate release by presynaptic *N*-methyl-D-aspartate autoreceptors in the entorhinal cortex. *Neuroscience* **75,** 339–344 (1996).
21. Wong, E. H. *et al.* The anticonvulsant MK-801 is a potent *N*-methyl-D-aspartate antagonist. *Proc. Natl Acad. Sci. USA* **83,** 7104–7108 (1986).
22. Bloodgood, B. L., Giessel, A. J. & Sabatini, B. L. Biphasic synaptic Ca influx arising from compartmentalized electrical signals in dendritic spines. *PLoS Biol.* **7,** e1000190 (2009).
23. Bandyopadhyay, S., Shamma, S. A. & Kanold, P. O. Dichotomy of functional organization in the mouse auditory cortex. *Nature Neurosci.* **13,** 361–368 (2010).
24. Rothschild, G., Nelken, I. & Mizrahi, A. Functional organization and population dynamics in the mouse primary auditory cortex. *Nature Neurosci.* **13,** 353–360 (2010).
25. Wu, G. K., Li, P., Tao, H. W. & Zhang, L. I. Nonmonotonic synaptic excitation and imbalanced inhibition underlying cortical intensity tuning. *Neuron* **52,** 705–715 (2006).
26. Larkum, M. E. & Nevian, T. Synaptic clustering by dendritic signalling mechanisms. *Curr. Opin. Neurobiol.* **18,** 321–331 (2008).
27. Holthoff, K., Kovalchuk, Y., Yuste, R. & Konnerth, A. Single-shock LTD by local dendritic spikes in pyramidal neurons of mouse visual cortex. *J. Physiol.* **560,** 27–36 (2004).
28. Polsky, A., Mel, B. W. & Schiller, J. Computational subunits in thin dendrites of pyramidal cells. *Nature Neurosci.* **7,** 621–627 (2004).
29. Schiller, J., Major, G., Koester, H. J. & Schiller, Y. NMDA spikes in basal dendrites of cortical pyramidal neurons. *Nature* **404,** 285–289 (2000).
30. Stosiek, C., Garaschuk, O., Holthoff, K. & Konnerth, A. *In vivo* two-photon calcium imaging of neuronal networks. *Proc. Natl Acad. Sci. USA* **100,** 7319–7324 (2003).

Supplementary Information is linked to the online version of the paper at www.nature.com/nature.

Acknowledgements We thank J. Lou for technical assistance, D. Bayer, F. Bayer and W. Zeitz for building the scanning device, A. Fohr for software support and Y. Kovalchuk and H. Adelsberger for help during the initial experiments. This work was supported by the Schiedel Foundation, the German-Israeli Foundation (GIF grant 1002/2008 to I.N. and A.K.), the Deutsche Forschungsgemeinschaft (IRTG 1373) and the Bundesministerium für Bildung und Forschung (BMBF) in the frame of ERA-NET NEURON. A.K. is a Carl-von-Linde senior fellow of the Institute for Advanced Study of the Technische Universität München.

Author Contributions X.C., U.L., I.N., N.L.R. and A.K. carried out the experiments. U.L. and A.K. designed and constructed the imaging device. X.C., U.L., N.L.R., I.N. and A.K. performed the analysis. A.K. designed the study and wrote the manuscript with the help of all authors.

Author Information Reprints and permissions information is available at www.nature.com/reprints. The authors declare no competing financial interests. Readers are welcome to comment on the online version of this article at www.nature.com/nature. Correspondence and requests for materials should be addressed to A.K. (arthur.konnerth@lrz.tum.de).

METHODS

Animals and surgery. C57BL/6 mice (28–40 postnatal days) were used in these experiments. All experimental procedures were performed in accordance with institutional animal welfare guidelines and were approved by the state government of Bavaria, Germany. Surgery was carried out as described previously[5,30]. In brief, the mouse was placed onto a warming plate (37.5–38 °C) and anaesthetized by inhalation of 1–1.5% isoflurane (Curamed) in pure O_2. The depth of anaesthesia was assessed by monitoring the tail-pinch reflex and respiratory activity. The skin and muscles were removed under a dissecting microscope after locally applying an anaesthetic agent (xylocaine). A custom-made recording chamber was then glued to the skull with cyanoacrylic glue (UHU). A small craniotomy (~2 mm × 2.5 mm) was made using a high-speed drill with a small-tip steel burr (0.5 mm in diameter) to expose the left primary auditory cortex (centre of the craniotomy: Bregma −2.5 mm, 4.5 mm lateral to midline[23,24,31]). The dura was carefully removed and the craniotomy was filled with 1.5% low-melting-point agarose (~2 mm in thickness) to minimize brain pulsations. As compared to the previous study (~1 mm in thickness)[5], the agarose thickness was increased to improve mechanical stability for spine imaging. After surgery, the mouse was transferred into the recording apparatus and the level of anaesthesia was decreased to 0.8–1.2% isoflurane in pure O_2 (breathing rate 90–120 breaths per minute). The recording chamber was perfused with warm normal Ringer's solution containing 125 mM NaCl, 4.5 mM KCl, 26 mM $NaHCO_3$, 1.25 mM NaH_2PO_4, 2 mM $CaCl_2$, 1 mM $MgCl_2$ and 20 mM glucose (pH 7.4 when bubbled with 95% O_2 and 5% CO_2). The temperature of the mouse was maintained with a warming plate at between 36.5 °C and 37.5 °C.

***In vivo* electrophysiology.** Somatic whole-cell patch-clamp recordings of layer 2/3 neurons were obtained with an EPC10 amplifier (USB Quadro Amplifier, HEKA Elektronik) by using the 'shadow patching' procedure[10] under two-photon imaging guidance. Borosilicate glass pipettes with open-tip resistances of 5–7 MΩ were filled with a pipette solution containing 112 mM potassium gluconate, 8 mM KCl, 10 mM HEPES, 4 mM Mg-ATP, 0.375 mM Na_2GTP, 10 mM sodium phosphocreatine and 120 μM OGB-1, titrated to pH 7.20–7.25. In some recordings, the pipette solution also contained 0.2% biocytin for post-hoc morphological verification (Supplementary Fig. 3a). For pharmacological experiments, 1 mM MK-801 (a use-dependent, non-competitive NMDA receptor antagonist) was added to the pipette solution. At the somatic level, the electrical responses were reduced after blocking NMDA receptor channels by the use of MK-801 (Supplementary Fig. 11). The remaining response represents the non-NMDA-receptor-mediated component.

To minimize local brain damage, we performed no more than three attempts at whole-cell recordings at a given cortical location (more than 50% of neurons were recorded by the first electrode). After long recording sessions (1–2 h in our recordings), the pipette tip was sometimes backfilled with membrane debris (see for example the tip of patch pipette in Fig. 1a and Supplementary Fig. 10a). The series resistance of the pipette was continuously monitored and neurons were used for recording only if the resistance was <30 MΩ. Electrophysiological data were filtered at 10 kHz and sampled at 20 kHz using Patchmaster software (HEKA). During 15–20 min of the calcium dye loading period, we determined the frequency tuning properties of the somatic electrical responses. For this purpose, we applied pure tone stimuli at different frequencies (11 frequencies from 2 kHz to 40 kHz) and at different sound levels (from 50 dB to 0 dB attenuations).

During spine imaging, hyperpolarization was applied to prevent both spontaneous and sound-evoked action potentials. Because the action-potential activity of layer 2/3 neurons was sparse in our conditions, consistent with previous observations[12,23,24,32,33], some neurons did not need to be hyperpolarized to prevent action-potential firing. Across the population, 25% of the imaged neurons were not hyperpolarized ($n = 8$ of 32 neurons, see Supplementary Table 1). The resting membrane potentials of those neurons were in the range of −71 mV to −76 mV (−74 ± 1 mV) and they did not fire any action potential throughout the whole imaging period (except when they were actively depolarized by current injection). Pyramidal neurons with a similar range of resting potentials have previously been reported in layer 2/3 of the somatosensory cortex[34]. By comparison, the resting potentials of the neurons that required hyperpolarization were in the range of −61 mV to −69 mV (−65 ± 1 mV; $n = 24$ neurons). An appropriate amount of negative current injection (ranging from −50 pA to −200 pA) was used to hyperpolarize the firing neurons to a level (in the range of −70 mV to −77 mV; mean −73 ± 1 mV) corresponding to that of the non-firing ones (see details in Supplementary Table 1). Throughout the whole period of spine imaging of subthreshold calcium signals, no action potential was observed (see for example Supplementary Fig. 7). Spiking was only allowed for the purpose of comparing spike-evoked calcium responses (by actively depolarizing the neurons) and auditory-stimulation-evoked calcium responses.

Whole-cell recordings were targeted to the primary auditory cortex, identified on the basis of: (1) stereotaxic coordinates[23,24,31]; (2) the non-habituating excitatory postsynaptic potential (EPSP) responses to broadband noise and best-frequency tones; and (3) a reliable short-latency EPSP response to stimulation with broadband noise[12]. The latency of EPSP responses to the onset of stimulation (broadband noise, 0 dB attenuation) was in the range of 13.9 ms to 44.1 ms (mean ± s.e.m., 27.7 ± 2.2 ms; $n = 16$ neurons) (Supplementary Fig. 5), consistent with the responses in the core auditory pathway. A fourth criterion for identification of the primary auditory cortex was frequency-tuned responses (see example of the characteristic V-shaped receptive field in Supplementary Fig. 7c)[14].

High-speed two-photon calcium imaging of dendritic spines. *In vivo* calcium imaging was carried out using a custom-built two-photon microscope (see Supplementary Fig. 1). This scanning system consisted of a galvanic mirror (6215H, Cambridge Technology) for the slower *y*-scan, and the acousto-optic deflector 2 (AOD2) (Crystal Technology Inc. 4150) for the fast *x*-scan[35,36]. We compensated the chromatic dispersion with an AOD[37], namely AOD1 (also Crystal Technology Inc. 4150). When imaging at 1,000 frames s^{-1}, we used frames of about 28 μm × 9 μm size (250 × 80 pixels, 50-ns pixel dwell time). Because sweeping through the acoustic frequencies of the AOD in a short time results in a chirped optical grating, causing beam-distortions afterwards[38], we used chirped grating compensation optics (CGCO) consisting of lenses placed between AOD2 and the galvanic mirror. CGCO consist of a set of cylindrical lenses that are mounted into a rotating wheel. A given lens is used for a specific zoom factor and compensates for beam distortions related to the zoom-factor-dependent changes in the ratio of scan-angle to time interval through AOD2, ensuring accurate infinity correction. AOD2 and the galvanic mirror were controlled by signal generators (PXI 5412, National Instruments), synchronized by a high-speed data acquisition digitizer (PXIe 5122, National Instruments) running at 20 MHz. The data acquisition was controlled by custom-written software based on LabVIEW (LabVIEW 2009, National Instruments). The scanning system was mounted on a standard upright microscope (BX51WI, Olympus) equipped with a water-immersion objective (×40/0.8 NA/3.5 WD, Nikon). The excitation wavelength was 800 nm. The average power delivered to the brain was in the range of 4–18 mW. Such relatively low power levels have previously been used for calcium imaging of neuronal somata to minimize possible bleaching and phototoxicity[39,40].

Calcium imaging was started approximately 15–20 min after achieving whole-cell configuration, to allow diffusion of the calcium dye (or MK-801 for pharmacological experiments) into the dendrites. We selected regions of the dendrites with as many visible spines in one focal plane as possible, irrespective of the relative position from the soma. Therefore, the imaged dendritic segments were located throughout the dendritic tree of upper layer 2/3 neurons, ranging from the most apical dendrites, close to the pial surface, down to basal dendrites (up to 300-μm depth). For each neuron, 1–7 dendritic segments were imaged. Generally, 4–10 sweeps (each sweep had a recording period of 24–30 s) were recorded for each dendritic segment. At the end of the recordings, *z*-stacks of the dendritic segments (28 μm × 9 μm, 1,000 Hz; step size 0.25 μm) were acquired. In addition, for each recorded neuron, *z*-stacks (6–10 stacks, each stack 90 μm × 90 μm, 80 Hz; step size 0.5 μm) of the dendritic tree were acquired at different positions relative to the soma.

Auditory stimulation. Sounds were presented in free-field using an electrostatic speaker driver (ED1, Tucker Davis Technologies) with an ES1 free-field speaker (TDT) placed about 2 cm away from the contralateral ear of the mouse. Because the experiments were performed outside a sound-proof chamber, and because the two-photon setup is noisy, we measured the amount of background noise in the setup. The background noise was measured using a 1/4-in microphone (Microtech Gefell) connected to a B&K measuring amplifier (Type 2636), and then sampled at 240 kHz on a PCI 6731 sound card (National Instruments) for additional offline analyses. Background noise was dominated by low-frequency components, whereas the recorded neurons had much higher best frequencies. Therefore, we do not believe that the background sound markedly affected the neuronal responses we studied. Nevertheless, the two-photon imaging setup was switched on at least 5 min before each recording session to ensure habituation to the background noise.

We calibrated the sound levels by placing the microphone between the loudspeaker and the ear of the mouse, measuring the resulting sound levels. To avoid harmonic distortions, the gain of the ED1 driver was always set no higher than 9 dB attenuation. This level is used throughout this paper as the nominal 0 dB attenuation. Typically, this attenuation level corresponded to a sound level of 73 dB sound pressure level (SPL) for frequencies between 1 kHz and 10 kHz, and to a sound level of about 65 dB SPL for frequencies up to 40 kHz. Additional attenuation was achieved by reducing the gain of the ED1 driver. The resulting sound levels were verified by the B&K sound meter level; linearity was confirmed over a range of 30 dB. Bursts of broadband noise had a bandwidth of 0–50 kHz, and had the same overall energy as a tone at the same sound level. Thus, at 0 dB attenuation, the noise had a spectrum level of about 25 dB/$\sqrt{\text{Hz}}$.

For auditory stimulation, broadband noise and pure tones were generated with custom-written software based on LabVIEW (National Instruments), and transduced to analogue voltage through a PCI 6731 (National Instruments) sound card. For testing the tuning properties of single spines, 10 frequencies (2.0000, 2.7899, 3.8918, 5.4288, 7.5730, 10.5639, 14.7361, 20.5562, 28.6748 and 40.0000 kHz) ($n = 2$ neurons) or 11 frequencies (2.0000, 2.6986, 3.6411, 4.9129, 6.6289, 8.9443, 12.0684, 16.2836, 21.9712, 29.6454 and 40.0000 kHz) ($n = 8$ neurons), all in the range of 2–40 kHz, were applied. Each frequency or broadband noise stimulus was applied 6–8 times. The duration of each auditory stimulus was 100 ms (10-ms rise/fall time). The inter-stimulus interval was either 2 s (multiple-frequency experiments) or 4 s (broadband noise and 2-tone experiments).

Data analysis. All the analyses were restricted to pyramidal neurons that were identified according to the following two criteria. First, we assessed the presence of apical dendrites extending from a conical soma towards the pial surface[41] in both the post-hoc reconstructions of biocytin-filled neurons (Supplementary Fig. 3a) and the reconstructions of *in vivo* z-stacks of the recorded neurons (Supplementary Fig. 3b). Second, the spine density was measured from the three- dimensional reconstructions of dendrites. This density was comparable to that previously reported for pyramidal neurons[42] and markedly higher than that of non-pyramidal neurons (Supplementary Fig. 3c, d)[42].

The analyses of electrophysiological and calcium imaging data were done offline using Igor Pro (Wavemetrics), LabVIEW and Matlab (Mathworks). The imaging data that were acquired at 1,000 frames s^{-1} were downsampled 10–12-fold (temporally downsampled to 80–100 frames s^{-1}) (see Supplementary Fig. 4b, red trace in the upper panel). Calcium signals were expressed as relative fluorescence changes ($\Delta f/f$), corresponding to the mean fluorescence from all pixels within specified regions of interest. Regions of interest for spine calcium-imaging analyses were restricted to the clearly visible protrusions emanating laterally from the dendritic shaft[43]. Spines located just above or below the dendritic shaft were not visible during calcium recordings (two-dimensional imaging). In a few cases, signals from dendritic shafts might have been contaminated by the signals of active spines along the optical axis (for example, Supplementary Fig. 9), but such cases were not included in our analyses. Therefore, the number of active spines and the number of visible spines were underestimated.

To improve the visibility of calcium transients, the $\Delta f/f$ traces shown in all figures were smoothed with an exponentially averaging IIR filter (time constant 80 ms)[5,11] (see Supplementary Fig. 4b, black trace in the upper panel). A fluorescent change was accepted as a calcium signal when its amplitude (peak value) was three times larger than the standard deviation of the noise that was determined for a period of 100 ms just before auditory stimulation. Neurons in the auditory cortex can respond to both onset and offset of the auditory stimulus, driven by non-overlapping sets of synaptic inputs[14]. To include both sets of synapses, transients were identified as sound-evoked calcium responses when they occurred in a 200-ms time window after the stimulus onset. With a stimulus duration of 100 ms, it has recently been shown that the off response has a latency of about 100 ms after the stimulus offset[14]. The corresponding somatic responses (EPSPs) were also quantified by the average amplitude of depolarization during this 200-ms period (for example, Fig. 2b, c).

In each dendritic segment, spines that showed calcium signals were classified as active spines. The next step of analysis consisted of determination of the mean standard deviation of the baseline for all active spines in each dendritic segment. This value was then taken to decide whether the remaining spines were silent (with a baseline standard deviation lower than three times that of the active spines) or noisy (with a baseline standard deviation higher than three times that of the active spines). The noisy spines were thus defined by:

$$\mathrm{SD}_{\mathrm{noisy}} \geq \frac{3 \times \sum_i \mathrm{SD}_i}{n}$$

where $\mathrm{SD}_{\mathrm{noisy}}$ is the baseline standard deviation of the noisy spine, SD_i is the baseline standard deviation of active spines and n is the number of active spines in the same dendritic segment. The noisy spines corresponded to spines that were slightly out of the focal plane during the recordings and therefore had weak fluorescence signals (see examples in Supplementary Fig. 6a). In these spines, calcium signals evoked by auditory stimulation could not be assessed accurately because of a poor signal-to-noise ratio. Therefore, these noisy spines were not included in our analyses.

The frequency tuning curves were constructed by plotting the average values (and the s.e.m.) of the calcium signal amplitudes from single trials for each frequency tested (Fig. 3b, c, upper panels). The amplitude of a calcium signal was determined as the average value for a period of 200 ms around the peak of the calcium transient (2 data points before and 14 points after the peak, with a frame rate of 80 Hz). The baseline value was calculated for a period of 100 ms before the onset of the auditory stimulus. Pure-tone frequencies that induced response amplitudes higher than half of the maximal response were defined as effective frequencies. Spines were defined as narrowly tuned when their response band (the maximal difference between effective frequencies), was ≤ 1 octave. The average tuning curves of both narrowly and widely tuned spines (Fig. 3b, c, lower panels) were constructed using the following procedure: the tuning curves were normalized to the highest amplitude and aligned on the centre frequency of their response band. For each frequency tested, average values of the calcium response amplitude and the s.e.m. were calculated. The tuning width (ΔFrequency) was determined by the maximal difference between effective frequencies.

The distance between spines was estimated by measuring the distance between the projections of the spines to the dendritic axis (Fig. 3f, g). Therefore, the distance was, in some instances, shorter than that of the spatial resolution if two resolved spines were located on opposite sides of a dendrite (for example, the position of the leftmost spines in the image of Fig. 3a). The reconstructed z-projection images of recorded neurons were obtained using ImageJ (http://rsbweb.nih.gov/ij/). Three-dimensional reconstructions of dendrites were achieved using two programs: Huygens (Scientific Volume Imaging) for deconvolution and Amira (http://www.amiravis.com/) for reconstruction. Statistical analyses were performed with SPSS software (SPSS Inc), using paired or unpaired Student's t-test as appropriate. $P < 0.05$ was considered statistically significant.

31. Franklin, K. & Paxinos, G. *The Mouse Brain In Stereotaxic Coordinates.* (Academic, 2001).
32. Busche, M. A. *et al.* Clusters of hyperactive neurons near amyloid plaques in a mouse model of Alzheimer's disease. *Science* **321,** 1686–1689 (2008).
33. de Kock, C. P. & Sakmann, B. High frequency action potential bursts (≥100 Hz) in L2/3 and L5B thick tufted neurons in anaesthetized and awake rat primary somatosensory cortex. *J. Physiol.* **586,** 3353–3364 (2008).
34. Svoboda, K., Helmchen, F., Denk, W. & Tank, D. W. Spread of dendritic excitation in layer 2/3 pyramidal neurons in rat barrel cortex *in vivo*. *Nature Neurosci.* **2,** 65–73 (1999).
35. Lechleiter, J. D., Lin, D. T. & Sieneart, I. Multi-photon laser scanning microscopy using an acoustic optical deflector. *Biophys. J.* **83,** 2292–2299 (2002).
36. Roorda, R. D., Hohl, T. M., Toledo-Crow, R. & Miesenbock, G. Video-rate nonlinear microscopy of neuronal membrane dynamics with genetically encoded probes. *J. Neurophysiol.* **92,** 609–621 (2004).
37. Kremer, Y. *et al.* A spatio-temporally compensated acousto-optic scanner for two-photon microscopy providing large field of view. *Opt. Express* **16,** 10066–10076 (2008).
38. Gerig, J. S. & Montague, H. A simple optical filter for chirp radar. *Proc. IEEE* **52,** 1753 (1964).
39. Kerlin, A. M., Andermann, M. L., Berezovskii, V. K. & Reid, R. C. Broadly tuned response properties of diverse inhibitory neuron subtypes in mouse visual cortex. *Neuron* **67,** 858–871 (2010).
40. Sohya, K., Kameyama, K., Yanagawa, Y., Obata, K. & Tsumoto, T. GABAergic neurons are less selective to stimulus orientation than excitatory neurons in layer II/III of visual cortex, as revealed by in vivo functional Ca2$^+$ imaging in transgenic mice. *J. Neurosci.* **27,** 2145–2149 (2007).
41. Peters, A. & Jones, E. G. in *Cerebral Cortex: Cellular Components of the Cerebral Cortex* Vol. 1 (eds Peters, A. & Jones, E. G.) 107–121 (Plenum, 1984).
42. Kawaguchi, Y., Karube, F. & Kubota, Y. Dendritic branch typing and spine expression patterns in cortical nonpyramidal cells. *Cereb. Cortex* **16,** 696–711 (2006).
43. Holtmaat, A. J. *et al.* Transient and persistent dendritic spines in the neocortex *in vivo*. *Neuron* **45,** 279–291 (2005).

Supplementary Figure 1

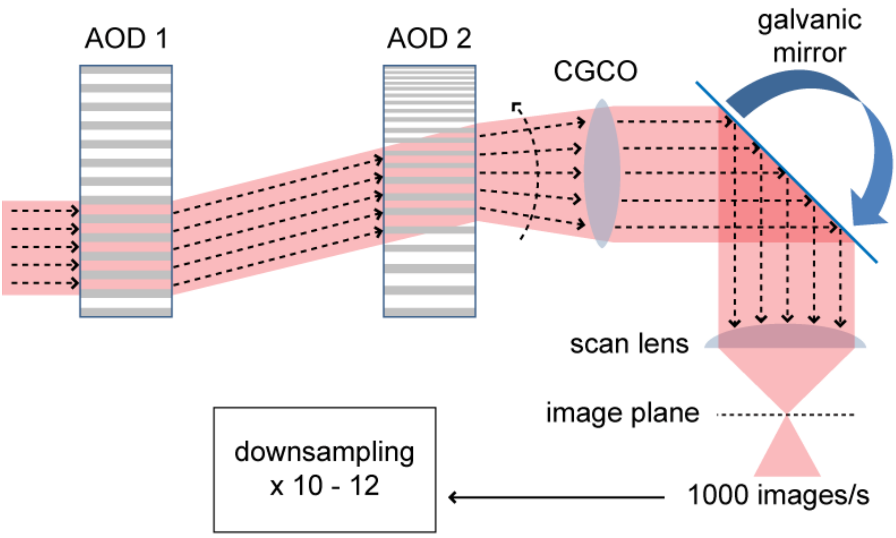

Sketch of the AOD-based two-photon microscope setup.

The basic unit of the high-speed scanning device consists of the acoustic-optic deflector2 (AOD2) that is combined with a galvanic mirror[1-3] and the addition of the AOD1 that compensates for spatio-temporal dispersion[4]. A key factor for obtaining images with a high spatial resolution was the implementation of scanning frequency-dependent chirped grating compensation optics (CGCO). For the offline analysis, the frame rate was downsampled 10-12 fold.

Supplementary Figure 2

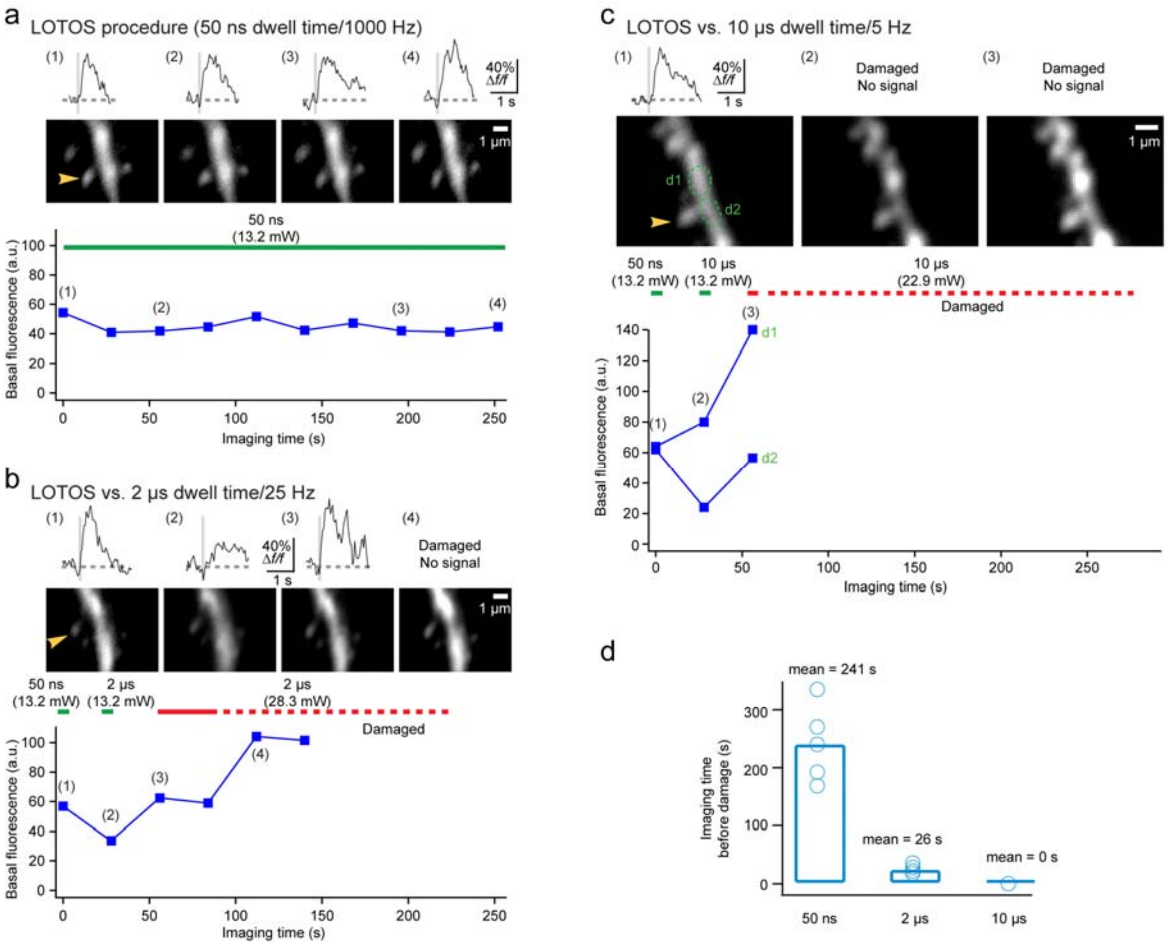

Comparison of the LOTOS procedure with standard imaging using different pixel dwell times.

a, Spine imaging using LOTOS (LOw power Temporal OverSampling) procedure. Upper panel, calcium responses to auditory stimulation (broadband noise at 0 dB attenuation) from a spine pointed out by the yellow arrowhead on the images of the recorded dendritic segment (average of 6250 frames from a 6.25 sec-recording period). Lower graph, time course of basal fluorescence from the entire dendritic segment. The pixel dwell time (50 ns) and the average power of the excitation light (13.2 mW) delivered to the brain are indicated on the top of the graph. The numbers in parenthesis indicate the time points at which the images and traces shown in the upper panel were taken. **b**, Comparison of LOTOS procedure with 2 µs pixel dwell time. The imaging of this dendritic segment was first done with the LOTOS procedure (50 ns pixel dwell time and 13.2 mW). The corresponding auditory-evoked spine calcium transient, the average image and the value of basal fluorescence are indicated by the number 1 in parenthesis. Increasing pixel dwell time (to 2 µs) at the same level of power (13.2 mW) dramatically reduced both the basal fluorescence and the amplitude of the calcium signal (number 2). Note the 1.8 times gain in basal fluorescence using the LOTOS procedure. By increasing the power to 28.3 mW (number 3), the basal fluorescence of the dendritic segment and the amplitude of the spine calcium signal increased to similar levels as those obtained with the LOTOS procedure. However, around 30 s later, the basal fluorescence increased 2 times more and no calcium response was detected anymore (number 4). This dramatic increase in the basal fluorescence indicates the occurrence of photodamage, as previously reported in slices[5]. **c**, Comparison of LOTOS procedure with 10 µs pixel dwell time. As in panel b, the LOTOS procedure was first performed (number 1). The auditory-evoked spine calcium signals and the images of the recorded dendritic segment are shown as in panel b. The basal fluorescence changes from 2 small dendritic regions (d1 and d2) indicated by green dashed lines on the images are shown in the lower graph. With 10 µs pixel dwell time and the same level of power (number 2), the basal fluorescence in d2 dropped to ~30% of its original value, whereas the basal fluorescence in d1 increased, indicating the start of local photodamage (blebbing). At this time point, no calcium signal from the spine indicated by the yellow arrowhead was detected. Increasing the power resulted in further photodamage (number 3, the basal fluorescence in d1 increased more than 2 times). **d**, Summary of the imaging time before photodamage (*n* = 5 dendritic segments for 50 ns pixel dwell time, 4 dendritic segments for 2 µs pixel dwell time, and 4 dendritic segments for 10 µs pixel dwell time). The dendritic segments were imaged from 3 neurons. For all these recordings, the auditory stimulation consisted in broadband noise at 0 dB attenuation applied for 100 ms duration with 4 s intervals between two stimulations.

Supplementary Figure 3

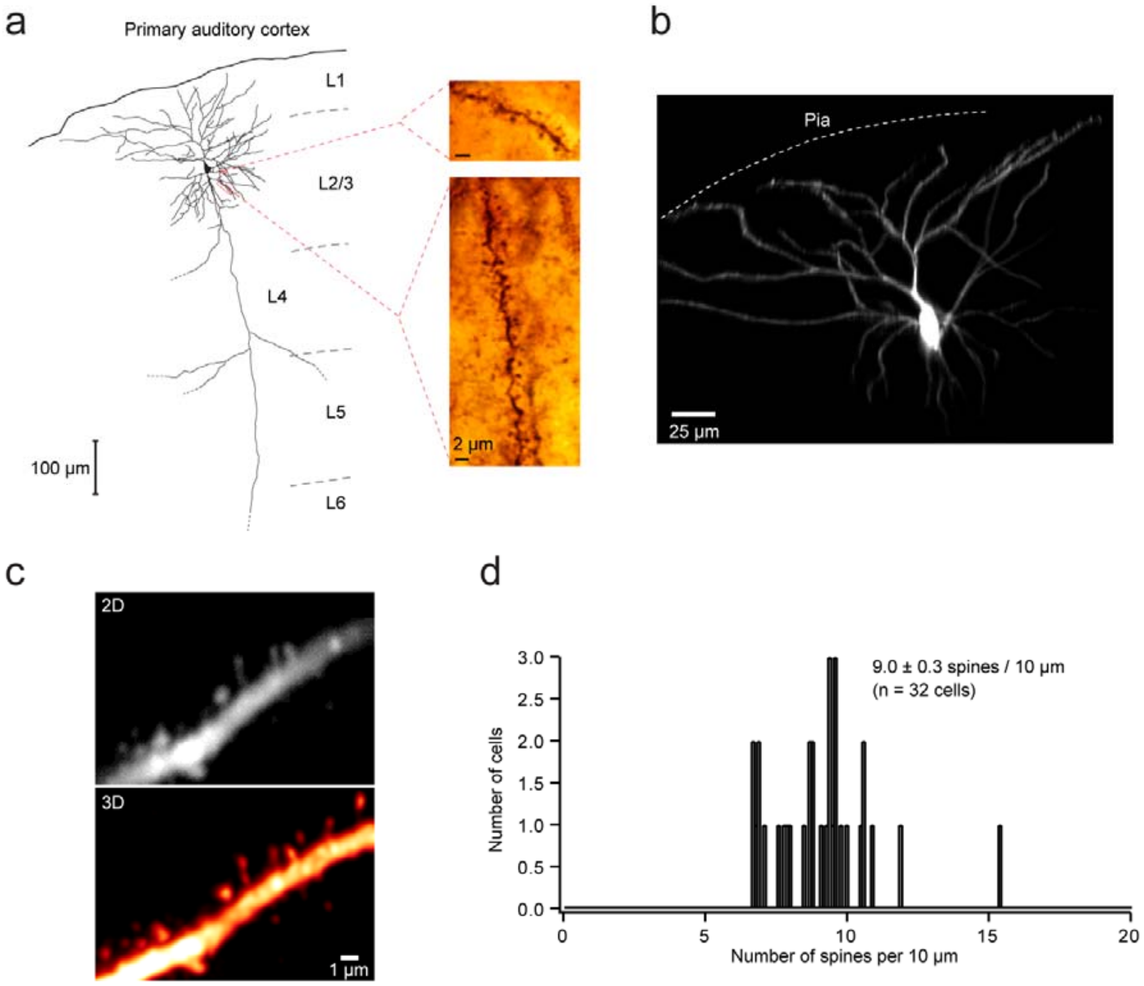

Identification of layer 2/3 pyramidal neurons in the mouse primary auditory cortex.

a, Left panel, post-hoc reconstruction of a biocytin-filled neuron (projection along the antero-posterior axis). Biocytin was delivered into the neuron through a whole-cell patch pipette during *in vivo* recordings of auditory-evoked responses. The cortical layers (L) are indicated on the right. Right panel, microphotographs of two dendritic segments showing the high density of dendritic spines. **b**, Projection image (along the antero-posterior axis) of a recorded neuron filled with OGB-1. Note the typical morphology of pyramidal neurons, characterized by apical dendrites extending from a conical soma toward the pial surface[6]. **c**, 2D (average of 6250 frames) and 3D images of one dendritic segment. Spine number counting was performed in 3D images. **d**, Distribution of the spine density (number of spines per 10 μm) in the recorded dendritic segments from all neurons used in this study. Note that these density values are strikingly higher than those reported in nonpyramidal neuronal subtypes, including Martinotti cells (mean = 2.91 spines/10 μm)[7].

Supplementary Figure 4

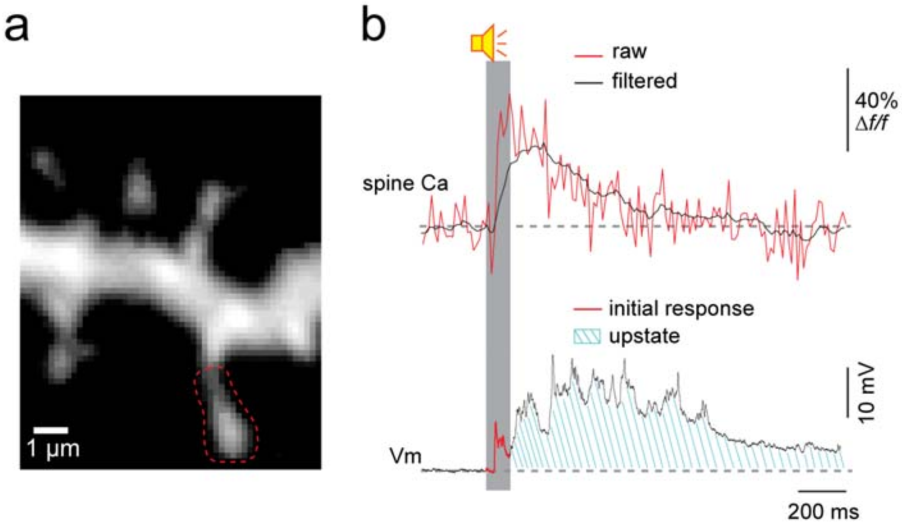

Auditory stimulation-evoked calcium signal in a single spine and the corresponding somatically recorded depolarization.

a, Image of one dendritic segment (average of 6250 frames). **b**, Calcium transient from a single spine (upper panel), indicated by a red dashed line in panel a, and the electrical response from the soma of the corresponding neuron (lower panel). The initial electrical response was usually accompanied by a longer lasting depolarization component, namely upstate. For the spine calcium response, the raw (80 Hz, downsampled from 1000 Hz) and filtered (with an exponentially-averaging IIR filter) traces are shown in red and black, respectively. Note that the spine calcium transient (upper trace) corresponds to the EPSP-like early depolarization (initial response, lower red trace). Grey bar indicates sound stimulation (BBN, 100 ms duration, 0 dB attenuation). V_{rest} = -66 mV; V_{AS} = -72 mV; I_{inject} = -100 pA.

Supplementary Figure 5

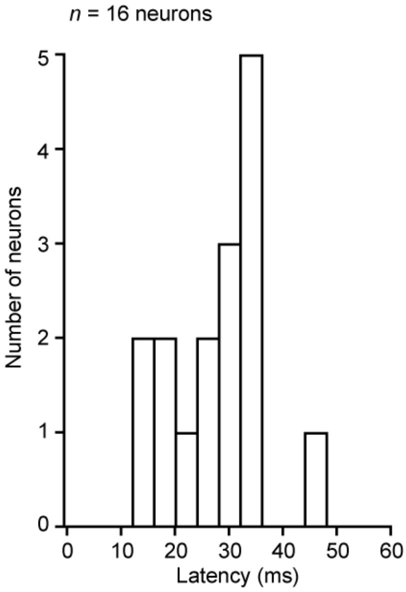

Latency of the onset of sound-evoked excitatory postsynaptic potentials (EPSPs). Distribution of the latencies of broadband noise-evoked EPSPs recorded in the whole-cell configuration from 16 neurons (10 neurons were also used for spine imaging, and 6 neurons were only used for electrical recording) in the mouse auditory cortex *in vivo*. Stimulus parameters: 0 dB attenuation, 100 ms duration.

Supplementary Figure 6

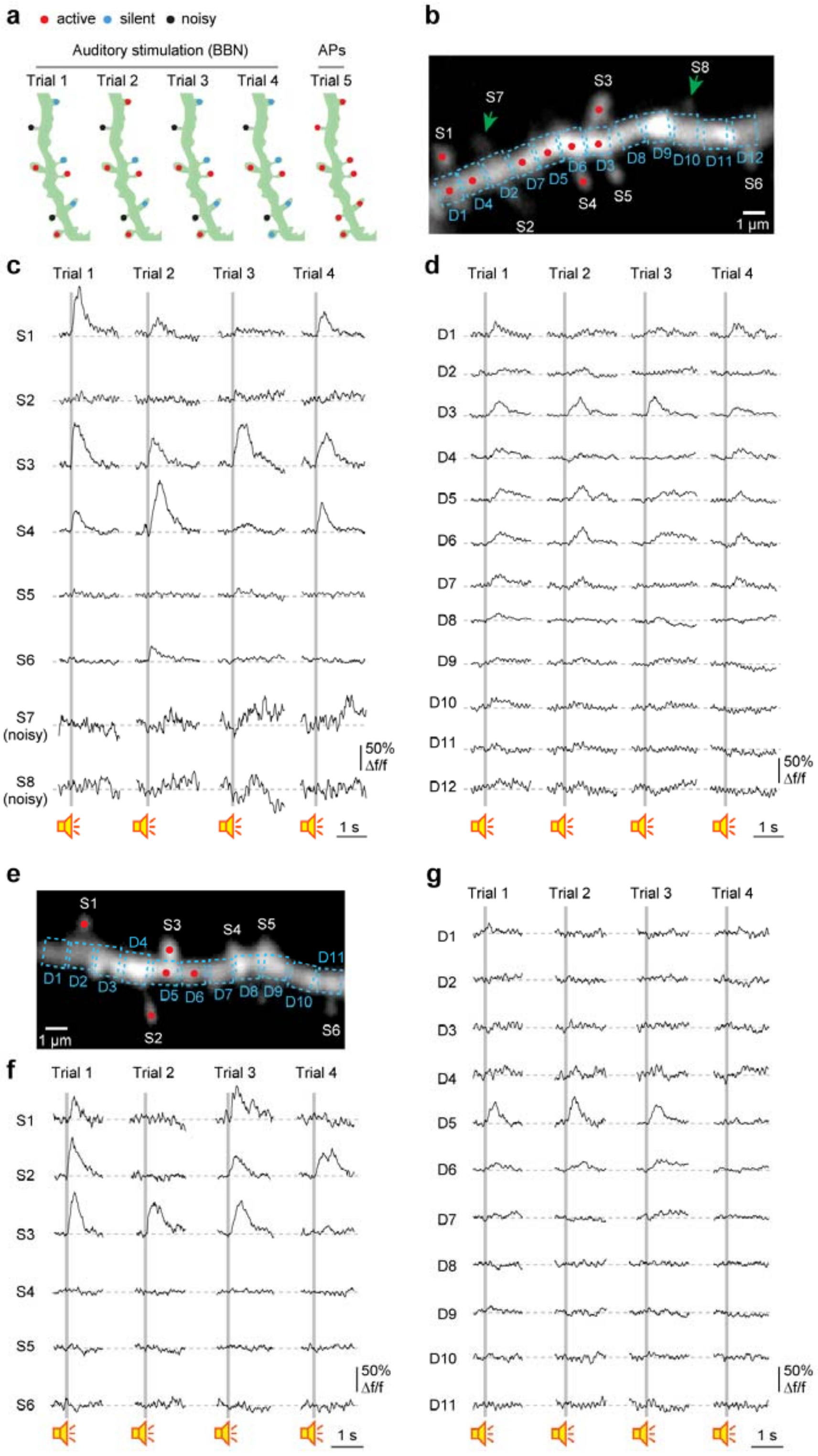

Auditory-evoked calcium signals in spines vs. dendrites.

a, Cartoons of the imaged dendritic segment shown in Figure 1a-c depicting the activity status of the spines during each trial of stimulation (auditory stimulation from trial 1 to 4 or somatic action potentials in trial 5). Active, silent and noisy spines are indicated by red, blue and black dots, respectively (see Supplementary Methods for the criteria defining these three groups). **b**, Two photon image of the rotated dendritic segment shown in panel a, with small regions of interest (1 µm length) along the dendritic shaft. Red dots indicate the regions in which auditory-evoked calcium signals were detected. **c**, Calcium signals recorded in the spines indicated in panel b (S1-S8), during individual trials of auditory stimulation (trials correspond to those illustrated in panel a). Note that two spines (S7 and S8, green arrows in panel b) are "noisy" spines. **d**, Calcium signals recorded in the small dendritic segments indicated in panel b (D1-D12) during the same individual trials of auditory stimulation as those shown in panels a and c. Note the smaller amplitude of dendritic shaft signals as compared to spine calcium signals. **e**-**g**, Calcium signal analysis (similar to that shown in panels b-d) of a dendritic segment from another layer 2/3 neuron (V_{rest} = -63 mV; V_{AS} = -73 mV; I_{inject} = -200 pA). Note the calcium signals in the active spines S1 and S2 and the absence of calcium signals in the adjacent dendritic shafts D2 and D4. Grey bars indicate sound stimulation (BBN: 100 ms duration, 0 dB attenuation).

Supplementary Figure 7

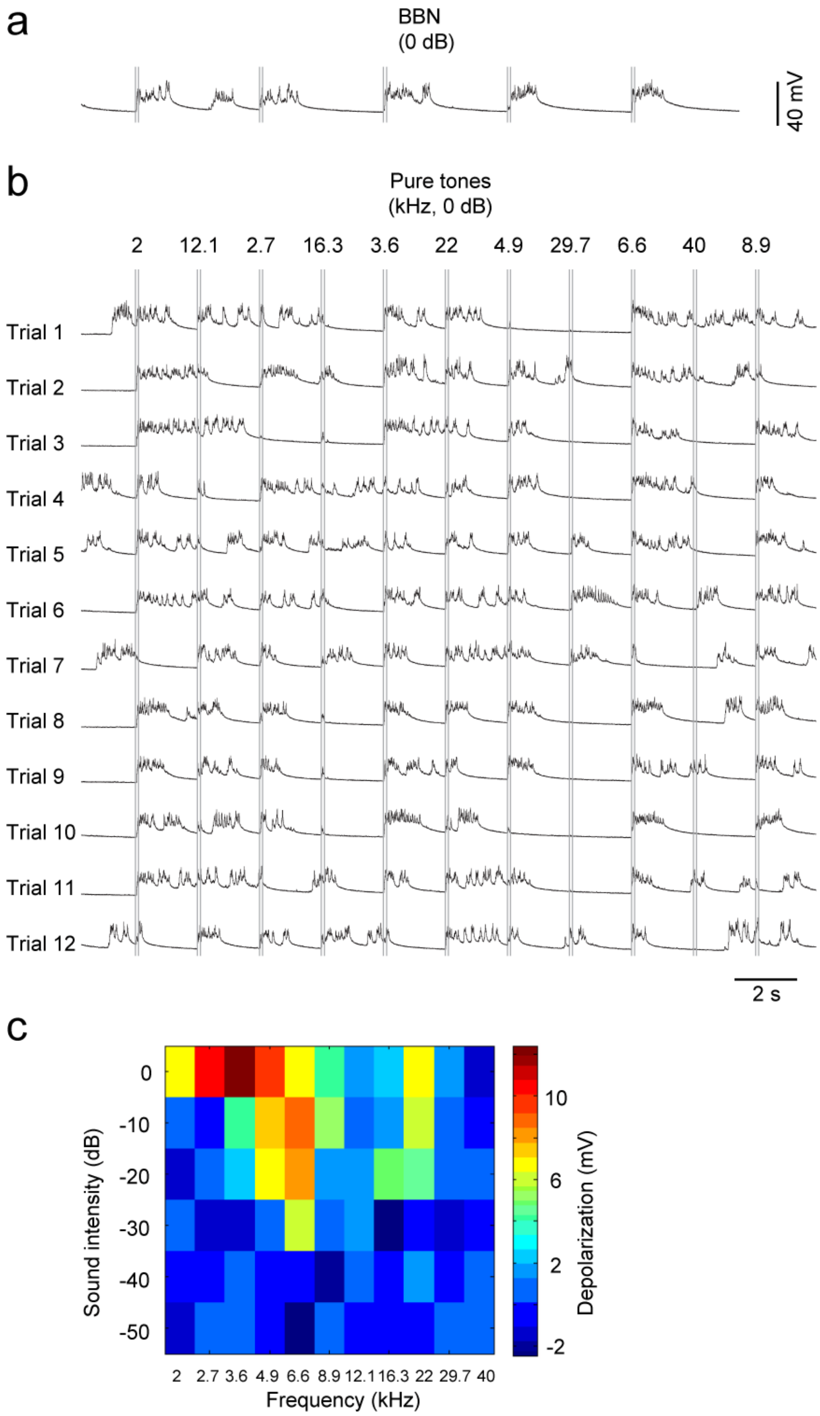

Subthreshold somatic depolarization during auditory stimulation.

a, Somatic electrical responses evoked by 5 consecutive broadband noise stimuli (BBN) (0 dB attenuation, 100 ms). Grey vertical bars indicate the period of auditory stimulation. **b,** Somatic electrical responses evoked by pure tones stimulation (0 dB attenuation) in 12 individual trials. Grey bars indicate the sound stimulation. **c,** Characteristic V-shaped receptive field[8,9], calculated from this neuron (the same neuron as shown in Fig. 3d, Neuron 2). V_{rest} = -63 mV; V_{AS} = -73 mV; I_{inject} = -200 pA.

Supplementary Figure 8

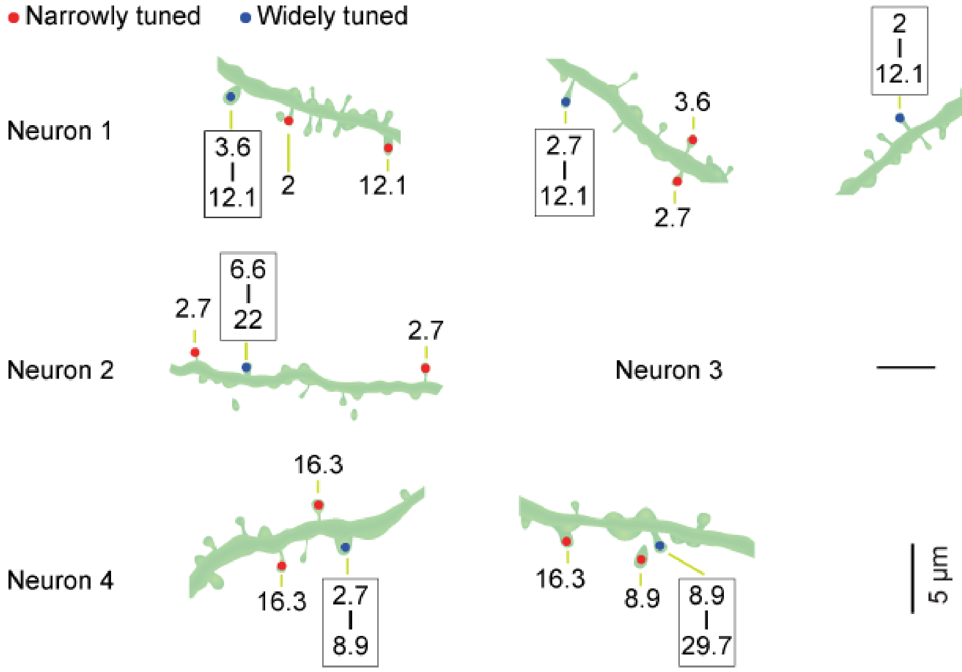

Heterogeneous distribution of pure tone-activated spines along dendrites.

Cartoons of all additional dendritic segments imaged in the 4 neurons shown in Figure 3e. The numbers indicate the effective frequencies that activate the corresponding spine. Narrowly tuned spines are marked by red dots and widely tuned spines are marked by blue dots.

Supplementary Figure 9

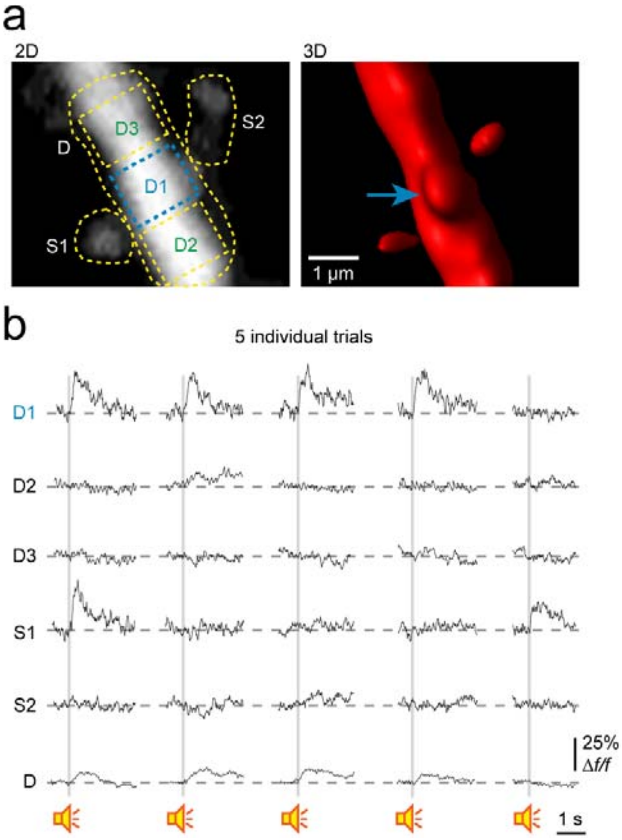

Calcium signals in a radial spine located on top of the dendritic shaft.

a, 2D (left) and 3D (right) images of a dendritic segment. Note that the spine above the dendritic shaft was not visible in the 2D image, but was seen in the 3D reconstruction (blue arrow). **b**, Calcium signals in response to 5 consecutive BBN stimuli from the spines S1 and S2 and the dendritic segments D, D1 – D3 indicated in panel a. Note the reliable responses in D1, the dendritic segment containing the spine. Grey bars indicate sound stimulation (BBN, 100 ms duration, 0 dB attenuation). V_{rest} = -67 mV; V_{AS} = -74 mV; I_{inject} = -120 pA.

Supplementary Figure 10

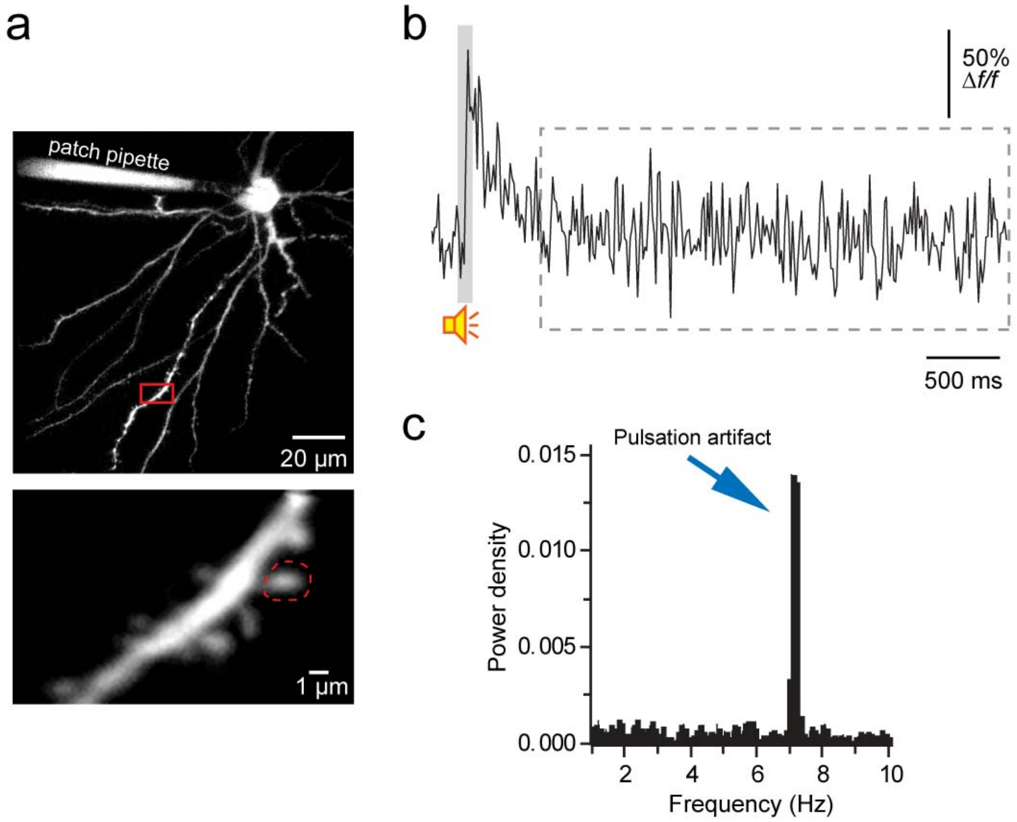

Heart beat pulsations during *in vivo* spine imaging.

a, Image of an *in vivo* recorded neuron (z-stack, upper panel) and of the dendritic segment indicated by the red rectangle (average of 6250 frames, lower panel). **b**, A raw trace (downsampled from 1000 Hz to 80 Hz) showing a clear auditory-evoked calcium response from the spine indicated by a red dashed line in panel a. Note that the amplitude and time course of the sound-evoked response is clearly different from those of the small regular and fast fluctuations. Grey bar indicates sound stimulation (BBN: 100 ms duration, 0 dB attenuation). **c**, Power spectrum of the portion of the calcium trace indicated by a grey dashed box in panel b. The major peak around 7-8 Hz is consistent with the heart beat rate of a mouse under isoflurane anesthesia (400-600 beats per minute)[10,11]. Note the absence of peak in the range of 1.5-2 Hz, corresponding to the respiratory rate's frequency (90-120 breaths per minute). V_{rest} = -62 mV; V_{AS} = -74 mV; I_{inject} = -50 pA.

Supplementary Figure 11

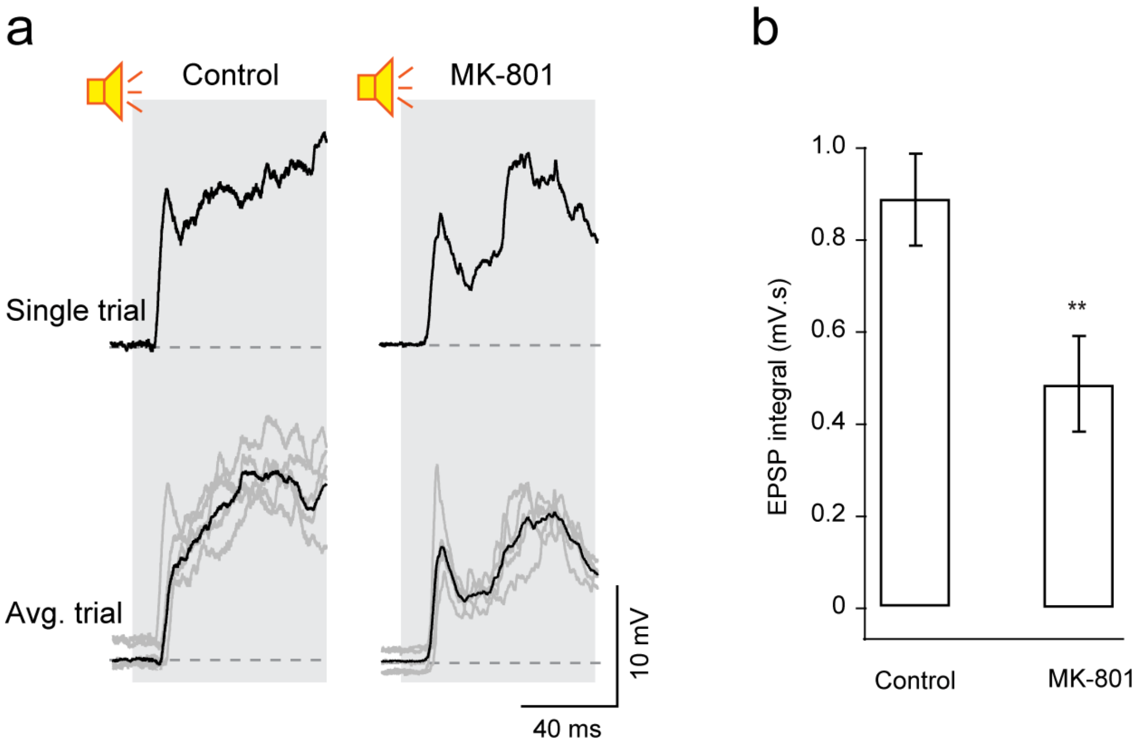

Effect of MK-801 on the somatic auditory stimulation-evoked depolarization.

a, Examples of somatic electrical responses evoked by sound stimulation (BBN, 0 db attenuation) without (left panels, control) or with intracellular application of MK-801 (right panels). Single trials are shown in the upper panels. Both single (grey traces) and averaged (black traces) trials are shown in the lower panels. Grey bars indicate sound stimulation (BBN, 100 ms duration, 0 dB attenuation). Control: V_{rest} = -65 mV, V_{AS} = -77 mV; MK-801: V_{rest} = -65 mV; V_{AS} = -75 mV. **b**, Comparison of the somatic electrical responses (EPSP) in control conditions (n = 10 neurons) and in the presence of intracellular MK-801 (n = 9 neurons; 5 neurons were also used for spine imaging, and 4 neurons were only tested for electrical recording). The integral of the EPSPs was calculated from the onset of the stimulus and for a 200 ms period. Unpaired t-tests, $^{**}P < 0.01$. Error bars, s.e.m.

Supplementary Table 1

	V_m[1] (mV)	V_{AS}[2] (mV)	I_{inject}[3] (pA)	Sites of data presentation
Neuron 1	-62	-72	-100	Fig. 1d,e,g and Fig. 2c; sFig.3d, 5, 11b
Neuron 2	-66	-76	-150	Fig. 1a-e,g and Fig. 2; sFig.3d, 5, 6,11b; sMovie 1
Neuron 3	-66	-72	-100	Fig. 1d,e, g, 2c, and 4a-i; sFig.3d, 4, 5,11b
Neuron 4	-67	-74	-120	Fig. 1d,e, g, 2c, and 4i; sFig.3d, 5, 9,11b
Neuron 5	-62	-74	-50	Fig. 1d,e, g, 2c, and 4i; sFig.3d, 5, 10,11b
Neuron 6	-62	-70	-80	Fig. 1d,e, g, 2c, and 4i; sFig.3d, 5,11b
Neuron 7	-65	-77	-100	Fig. 1d,e, g, 2c, and 4i; sFig.3d, 5,11a,b
Neuron 8	-68	-72	-100	Fig. 1d,e, g, 2c, and 4i; sFig.3d, 5,11b
Neuron 9	-73	-73	0	Fig. 1d,e, g, 2c, and 4i; sFig.3d, 5,11b
Neuron 10	-76	-76	0	Fig. 1d,e, g, 2c, and 4i; sFig.3d, 5,11b
Neuron 11	-61	-71	-80	Fig. 1g (control); sFig.3d
Neuron 12	-65	-75	-150	Fig. 1g (control); sFig.3d
Neuron 13	-67	-74	-80	Fig. 1g (control); sFig.3d
Neuron 14	-62	-71	-100	Fig. 1g (control); sFig.3d
Neuron 15	-75	-75	0	Fig. 1g (control); sFig.3d
Neuron 16	-72	-72	0	Fig. 1g (control); sFig.3d
Neuron 17	-74	-74	0	sFig.3d
Neuron 18	-65	-75	-100	Fig. 1f, g (MK-801); sFig.3d,11a,b
Neuron 19	-68	-71	-150	Fig. 1g (MK-801); sFig.3d,11b
Neuron 20	-67	-70	-50	Fig. 1g (MK-801); sFig.3d,11b
Neuron 21	-69	-72	-80	Fig. 1g (MK-801); sFig.3d,11b
Neuron 22	-71	-71	0	Fig. 1g (MK-801); sFig.3d,11b
Neuron 23	-63	-71	-80	Fig. 3b (bottom),c(bottom),d,f,g; sFig.3d
Neuron 24	-67	-74	-120	Fig. 3a-d,f,g; sFig.3d
Neuron 25	-66	-71	-60	Fig. 3b-g (e: neuron1); sFig.3d,8
Neuron 26	-67	-70	-120	Fig. 3d,f,g; sFig.3d
Neuron 27	-63	-73	-200	Fig. 3c-g(e: neuron2); sFig.3d, 6e-g, 7,8
Neuron 28	-69	-74	-80	Fig. 3b (bottom),c(bottom),d,f,g; sFig.3d
Neuron 29	-67	-75	-100	Fig. 3c-g(e: neuron3); sFig.3d,8
Neuron 30	-63	-71	-150	Fig. 3c-g(e: neuron4); sFig.3d,8
Neuron 31	-72	-72	0	Fig. 3d,f,g; sFig.3c, d
Neuron 32	-75	-75	0	Fig. 3b (bottom),c(bottom),d,f,g; sFig.3d

[1] V_m is the resting membrane potential and was determined during downstates, in the absence of current injection

[2] V_{AS} corresponds to the baseline membrane potential during auditory stimulation

[3] I_{inject} is the current injected to hyperpolarize neurons

List of all imaged neurons included in this study with the resting membrane potentials (V_m), the baseline membrane potentials during spine imaging (V_{AS}), the injected currents (I_{inject}) and the sites of data presentation. Note that Supplementary Figure was abbreviated as sFig.

Legend of Supplementary Movie 1

This video clip shows three consecutive trials of spine calcium responses (S1-S4) to pure tone stimulation (0 dB attenuation; 100 ms duration). The image data were downsampled from 1000 Hz to 80 Hz. S2 is a radial spine above the dendritic shaft. Note that no movement correction was applied for the movie. Also note that the sound pips are identical with those used during the experiment for auditory stimulation.

References

1 Grewe, B. F., Langer, D., Kasper, H., Kampa, B. M. & Helmchen, F. High-speed in vivo calcium imaging reveals neuronal network activity with near-millisecond precision. *Nat. Methods* **7**, 399-405 (2010).

2 Lechleiter, J. D., Lin, D. T. & Sieneart, I. Multi-photon laser scanning microscopy using an acoustic optical deflector. *Biophys. J.* **83**, 2292-2299 (2002).

3 Roorda, R. D., Hohl, T. M., Toledo-Crow, R. & Miesenbock, G. Video-rate nonlinear microscopy of neuronal membrane dynamics with genetically encoded probes. *J. Neurophysiol.* **92**, 609-621 (2004).

4 Kremer, Y. *et al.* A spatio-temporally compensated acousto-optic scanner for two-photon microscopy providing large field of view. *Opt. Express* **16**, 10066-10076 (2008).

5 Ji, N., Magee, J. C. & Betzig, E. High-speed, low-photodamage nonlinear imaging using passive pulse splitters. *Nat. Methods* **5**, 197-202 (2008).

6 Peters, A. & Jones, E. G. in *Cerebral Cortex: Cellular Components of the Cerebral Cortex.* Vol. 1 eds A. Perters & E. G. Jones) 107-121 (Plenum, 1984).

7 Kawaguchi, Y., Karube, F. & Kubota, Y. Dendritic branch typing and spine expression patterns in cortical nonpyramidal cells. *Cereb. Cortex* **16**, 696-711 (2006).

8 Rothschild, G., Nelken, I. & Mizrahi, A. Functional organization and population dynamics in the mouse primary auditory cortex. *Nat. Neurosci.* **13**, 353-360 (2010).

9 Scholl, B., Gao, X. & Wehr, M. Nonoverlapping sets of synapses drive on responses and off responses in auditory cortex. *Neuron* **65**, 412-421 (2010).

Summary

The sensory system responsible for receiving and processing sensory data allows animals to interact with the environment. How the central nervous system works for processing sensory information is a central question to neuroscientists. To the current knowledge, sensory cortical areas located in the mammalian brain receive, process, store, and compute the sensory inputs from sensory receptors via neural pathways. Until now, while much attention has been paid to understand how sensory information is processed in the cortex, the underlying cortical circuitry mechanisms and the synaptic rules for the organization of sensory inputs are just superficially touched. To gain some new insights into these questions, the overall research effort in my study was centered on two different brain regions, the cerebellar cortex and the primary auditory cortex. In both cases, several experimental techniques were used *in vivo*, such as two-photon imaging-based electrophysiological recording, calcium measurement, and local drug application, together with some conventional morphological and genetic methods. The use of these state-of-the-art physiological techniques allowed us to perform systematic studies *in vivo* at different levels in the wide range from long-distance neural circuits to single synapses with micron-size.

As presented above in each section, several projects have been completed: 1) Disruption of the olivo-cerebellar circuit by Purkinje neuron-specific ablation of BK channels; 2) Basket cell-mediated regulation of sensory-evoked signalling in the cerebellar cortical circuitry *in vivo*; 3) Dendritic organization of sensory input to cortical neurons in vivo and 4) the experimental protocol of this part. 5) Functional mapping of single spines in cortical neurons *in vivo*. In the projects 1, 2 and 5, I contributed to perform most of the experiments, data analyses, and manuscript preparations with the help of my supervisor and others (see below for detailed contributions).

1) Neural circuits in the cerebellum and their functions in sensory processing

Classically, the cerebellum of mammals was long believed as a motor organ [1]. The evidence for this was that lesion to the cerebellum cause impairments in motor behaviour or that the cerebellum is activated while moving [2,3]. Over the past decades, a growing body of evidence has suggested that cerebellum may also contribute to a large number of behaviours, such as emotion [4], cognitive and perceptual activities [5,6], autonomic responses [7], sensory acquisition, and sensory-motor integration [3,8]. Among these, the function in sensory acquisition and sensory-motor integration has been received much attention. For example, the cerebellum receives enormous inputs from different sensory modalities, including auditory, visual and tactile inputs [9,10]. Moreover, several lines of evidence also indicate the presence of sensory and motor integration in human cerebellum [3,8]. However, full understanding of the function of the cerebellum in sensory information processing requires the dissection of the underlying circuitry mechanisms.

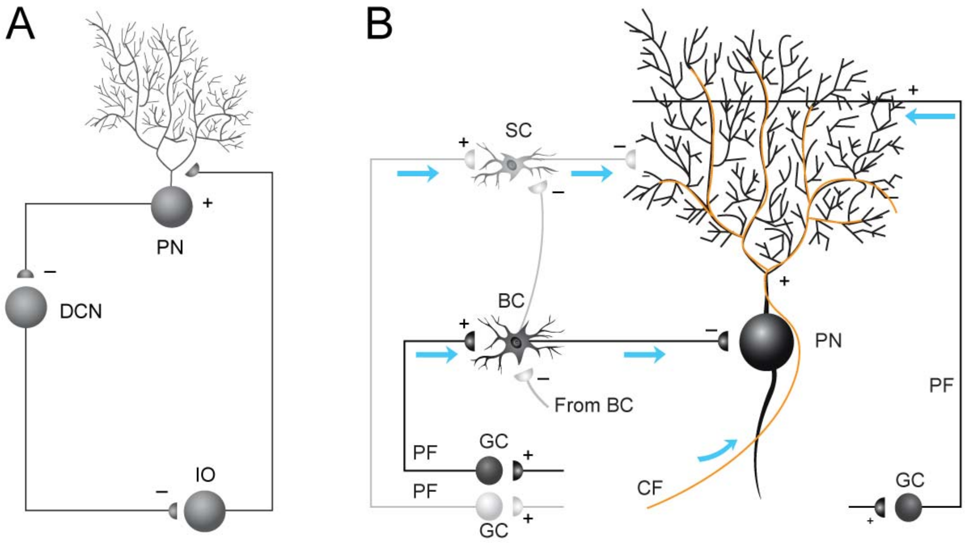

Summary_Figure 1. Two neuronal circuits in the cerebellum.

A, The olivo-cerebellar circuit. B, The cerebellar cortical circuit. PN, Purkinje neuron; DCN, deep cerebellar nuclei; IO, inferior olive; SC, stellate cell; BC, basket cell; PF, parallel fiber; GC, granule cell; CF, climbing fiber. Arrows indicate the direction of signal flow. +, excitatory action; -, inhibitory action.

Two neuronal circuits in the cerebellum are commonly studied: 1) the olivo-cerebellar circuit (Fig. 1A); 2) the cerebellar cortical microcircuit (Fig. 1B). The olivo-cerebellar circuit has been long suggested to be a closed loop that consists of the cerebellar cortex, the deep cerebellar nuclei, and the inferior olive [11,12]. The functional connection of this anatomical organization was recently confirmed by the result that increasing Purkinje neuron activity could increase the activity of climbing fibers [13]. In our study, by using a Purkinje neuron-specific BK channel knockout mice as experimental model, we provide clear evidence that the olivo-cerebellar connection is a functionally closed circuit. More importantly, the functional significance of this loop for normal behaviour is indicated by the severity of the motor deficits found in this mouse model. Although we have not done any direct experimental tests for the sensory function of this circuit, there is a possibility of the presence of sensory deficits in this mouse model. This is because ongoing sensory acquisition is required for guiding motor behaviour and for improving motor efficiency [3], and motor deficits in this mouse model may be accompanied by certain sensory impairments. Another reason could be that there are quite rich sensory inputs projecting to the cerebellar cortex. For example, whisker stimulation is the very common modality for the study of sensory integration, which is reliably represented in Crus I and Crus IIa of the cerebellar hemisphere [14-17]. In addition, the cerebellar cortex also consists of areas receiving the auditory and visual information, which was repetitively found in different species, such as cats, bats and rodents [9,18,19]. The BK mouse with abnormality of activity in both Purkinje neurons and the entire olivo-cerebellar circuit may suffer from some sensory deficit, which needs to be further investigated experimentally.

The microcircuitry of the cerebellar cortex is relatively simple: Purkinje neurons represent the sole output stage of this circuit. Parallel fibers from granule cells anatomically and physiological contact with both molecular layer interneurons and Purkinje neurons; in this way, a Purkinje neuron can be excited by parallel fibers and then inhibited by interneurons activated by the same set of parallel fibers, which is so-called feed-forward inhibition [20]. Although the extensive studies have been performed to resolve the activity of this circuit under the condition of processing, the relative roles of these neurons were not fully understood yet. In our study, we monitored the responses to whisker stimulation in all three types of cells, Purkinje neurons, basket cells and stellate cells, in the folium Crus IIa of the mouse cerebellar cortex. We found all of these cells are capable of responding to sensory stimulation. Due to the diversity of strength of feed-forward inhibition, the final outcome of each cell type is diverse: decrease in firing in Purkinje neurons, increase in basket cells, and no change in stellate cells. The feed-forward inhibition is decisively from basket cells. To our knowledge, this is a relative full picture of how all the elements in the cerebellar cortical circuit work during sensory processing.

2) Dendritic mapping of sensory inputs in cortical neurons

The neurons in the central nervous system capture and receive information from other neural cells by dendrites, the branched projections of neurons, and subsequently send the information to others by axonal terminals. From a morphological point of view, neurons were considered as ‘mysterious butterflies of the soul’ by Santiago Ramon Cajal, and recently the dendrites of neurons were referred as ‘wings of these butterflies’ by others [21].

From a functional aspect, a neuron can be just considered as an input-output device. Understanding of the working rules of the input part in this device, dendrite, is now one of the central challenges in neuroscience field. The first step is to clarify the dendritic organization of synaptic inputs during sensory processing.

Based on a number of experimental studies from in vitro preparations, several working models of how dendrites organize feature-specific synaptic inputs have been proposed: 1) All inputs of a neuron are specific for a single feature [22]; 2) Inputs with shared features are clustered on the same dendrite [23]; 3) Integration of synaptic inputs are distributed along individual dendrites [24,25]; 4) Integration of inputs are distributed throughout the dendritic tree [26]. The inconsistent models may be caused by non-physiological conditions of in vitro preparation (e.g. disconnected network, or temperature, or other factors), or due to the artificial synaptic stimulations used. What the truth in the real life is or how dendrites organize sensory inputs needs to be tested under in vivo conditions.

The second major part of my thesis work was to understand this question in the mouse visual and auditory cortex. In theory, two techniques can be probably used for detecting individual synaptic inputs in the dendrites: 1) dendritic electrophysiological recordings, patch clamp recording [27] or intracellular sharp electrode recordings [28]. The majority of experiments so far have been done in slice preparations or single cells. Although people have already started in vivo recording with electrode in such thin structure [16], the limited number of recording sites makes it impossible to map multiple inputs in a large area. 2) Instead, the alternative probability is to use calcium imaging with two-photon microscopy. The dendritic calcium imaging in the cortical neurons *in vivo* was done for the first time during sensory stimulation more than ten years ago [29]. Two-photon microscopy allows us to look into the brain through the highly scattering tissue. In addition, imaging method is able to provide large field of view for mapping multiple input sites in the dendritic tree. Therefore, dendritic calcium imaging by two-photon microscopy, together with somatic whole-cell patch-clamp recording, was suitable for us to study the spatial arrangement of sensory inputs in the dendrites in the living brain.

The experiments were first performed at dendritic levels in layer 2 and 3 neurons of the mouse visual cortex. The findings suggest that neurons in the visual cortex receive specifically tuned inputs over the entire dendritic tree, which argues against the all the previously proposed models observed *in vitro* by artificial stimulation.

The progress of development of two-photon microscopy technique eventually enabled us to deepen into the very fine structures, dendritic spines, which represent single synapses. By using AOD-based fast two-photon calcium imaging, we could reach single spine signals with impressive signal-to-noise ratio. Consistent with the results found in the visual cortex, we demonstrated salt-and-pepper like distribution of spines tuned for different sound frequency in the auditory cortex: even neighbouring spines on the same dendrite are mostly different. Besides, we have several other findings in this part: 1) single spines, but not dendritic shafts are the primary synaptic signaling units in vivo; 2) narrowly (45%) and widely (55%) tuned spines for sound frequency in cortical layer 2/3 neurons; 3) widespread distribution of sound level-sensitive spines in apical and basal dendrites. Overall, these findings serve as the first detailed characteristics of single spine activity during sensory stimulation. Our work also provides a possible mean of the study of synaptic plasticity associated with sensory experience and memory at single synapse level *in vivo*.

3) My contributions to the projects

In this last summary part, I have to specify my personal contributions in all the work during my PhD thesis study in a chronological manner. Before this, it should be emphasized that Prof. Arthur Konnerth, my supervisor, designed experiments and guided me step-by-step for all the projects.

a) Project I "Disruption of the olivo-cerebellar circuit by Purkinje neuron-specific ablation of BK channels"

This was in 2008 initiated by Dr. Yury Kovalchuk, who was my first teacher for using the two-photon microscope based on resonant scanner system and for preparing the mouse cerebellar cortex. Together with him, I carried out around 75 % of the published experiments and most of the data analyses, and assisted Prof. Arthur Konnerth to prepare the manuscript. Prof. Helmuth Adelsberger did all the behaviour tests, and Dr. Horst A. Henning and Dr. Georg Wietzorrek (Molecular and Clinical Pharmacology, Innsbruck Medical University) performed the immunohistology, and Dr. Matthias Sausbier, Georg Wietzorrek, Prof. Peter Ruth (Department of Pharmacology and Toxicology, University of Tübingen) provided all BK knockout mice. Prof. Yosef Yarom (Department of Neurobiology, Hebrew University) provided critical and important suggestions over the entire period.

b) Project II "Basket cell-mediated regulation of sensory-evoked signalling in the cerebellar cortical circuitry *in vivo*"

I performed most of the experiments and data analysis, with the help of Zsuzsanna Varga for some cell-attached patch-clamp recordings in Purkinje neurons and Dr. Horst A. Henning for histology of intereneurons. The draft of manuscript has been largely done and is waiting for submission.

c) Project III "Dendritic organization of sensory input to cortical neurons *in vivo*"

I contributed to establish whole-cell patch-clamp recording in the visual cortex *in vivo*, and then trained others for acquiring this technique. A number of recorded neurons in the published paper [30] by whole-cell patch-clamp recordings were done with my help.

d) Project IV "*In vivo* two-photon imaging of sensory-evoked dendritic calcium signals in cortical neurons"

As mentioned in Part III, I contributed to the development of whole-cell patch-clamp recording in the visual cortex *in vivo*.

e) Project V "Functional mapping of single spines in cortical neurons *in vivo*"

I performed all the whole-cell patch-clamp recordings and two-photon calcium imaging with the AOD-based setup built by Dr. Ulrich Leischner. I performed most of data analyses with the program in LabVIEW written by Hongbo Jia, which was published recently in details [31,32]. Dr. Nathalie L. Rochefort participated in the discussion during the process of manuscript preparation and did reconstruction of biocytin-labeld neurons. Prof. Israel Nelken (Department of Neurobiology, Hebrew University) provided the basic knowledge in the auditory field, showed me the position of the auditory cortex, arranged all entire auditory devices, helped for the analysis of frequency-tuned curves, and discussed for the preparation of manuscript. At the very early phase of this study, Prof. Helmuth Adelsberger and Christine Grienberger also discussed with me on how to find the primary auditory cortex in mouse.

References

1 Ito, M. *The cerebellum and neural control*. (Raven Press, 1984).

2 Fox, P. T., Raichle, M. E. & Thach, W. T. Functional mapping of the human cerebellum with positron emission tomography. *Proc Natl Acad Sci U S A* **82**, 7462-7466 (1985).

3 Gao, J. H. *et al.* Cerebellum implicated in sensory acquisition and discrimination rather than motor control. *Science* **272**, 545-547 (1996).

4 Sacchetti, B., Scelfo, B. & Strata, P. Cerebellum and emotional behavior. *Neuroscience* **162**, 756-762 (2009).

5 Chafetz, M. D., Friedman, A. L., Kevorkian, C. G. & Levy, J. K. The cerebellum and cognitive function: implications for rehabilitation. *Arch Phys Med Rehabil* **77**, 1303-1308 (1996).

6 Parsons, L. M. & Fox, P. T. Sensory and cognitive functions. *Int Rev Neurobiol* **41**, 255-271 (1997).

7 Sacchetti, B., Scelfo, B. & Strata, P. The cerebellum: synaptic changes and fear conditioning. *Neuroscientist* **11**, 217-227 (2005).

8 Wiestler, T., McGonigle, D. J. & Diedrichsen, J. Integration of sensory and motor representations of single fingers in the human cerebellum. *J Neurophysiol* **105**, 3042-3053 (2011).

9 Snider, R. S. & Stowell, A. Receiving areas of the tactile, auditory and visual systems in the cerebellum. *J. Neurophysiol.* **7**, 331-357 (1944).

10 Apps, R. & Garwicz, M. Anatomical and physiological foundations of cerebellar information processing. *Nat Rev Neurosci* **6**, 297-311 (2005).

11 Fredette, B. J. & Mugnaini, E. The GABAergic cerebello-olivary projection in the rat. *Anat Embryol (Berl)* **184**, 225-243 (1991).

12 Jacobson, G. A., Rokni, D. & Yarom, Y. A model of the olivo-cerebellar system as a temporal pattern generator. *Trends Neurosci.* **31**, 617-625 (2008).

13 Marshall, S. P. & Lang, E. J. Local changes in the excitability of the cerebellar cortex produce spatially restricted changes in complex spike synchrony. *J Neurosci* **29**, 14352-14362 (2009).

14 Brown, I. E. & Bower, J. M. Congruence of mossy fiber and climbing fiber tactile projections in the lateral hemispheres of the rat cerebellum. *J. Comp. Neurol.* **429**, 59-70 (2001).

15 Chadderton, P., Margrie, T. W. & Häusser, M. Integration of quanta in cerebellar granule cells during sensory processing. *Nature* **428**, 856-860 (2004).

16 Loewenstein, Y. *et al.* Bistability of cerebellar Purkinje cells modulated by sensory stimulation. *Nat Neurosci* **8**, 202-211 (2005).

17 Rancz, E. A. *et al.* High-fidelity transmission of sensory information by single cerebellar mossy fibre boutons. *Nature* **450**, 1245-1248 (2007).

18 Jen, P. H., Vater, M., Harnischfeger, G. & Rubsamen, R. Mapping of the auditory area in the cerebellar vermis and hemispheres of the little brown bats, Myotis lucifugus. *Brain Res* **219**, 156-161 (1981).

19 Huang, C. M., Liu, G. L., Yang, B. Y., Mu, H. & Hsiao, C. F. Auditory receptive area in the cerebellar hemisphere is surrounded by somatosensory areas. *Brain Res* **541**, 252-256 (1991).

20 Mittmann, W., Koch, U. & Hausser, M. Feed-forward inhibition shapes the spike output of cerebellar Purkinje cells. *J Physiol* **563**, 369-378 (2005).

21 Johnston, D. & Narayanan, R. Active dendrites: colorful wings of the mysterious butterflies. *Trends Neurosci* **31**, 309-316 (2008).

22 Yoshimura, Y., Dantzker, J. L. & Callaway, E. M. Excitatory cortical neurons form fine-scale functional networks. *Nature* **433**, 868-873 (2005).

23 Larkum, M. E. & Nevian, T. Synaptic clustering by dendritic signalling mechanisms. *Curr. Opin. Neurobiol.* **18**, 321-331 (2008).

24 Branco, T. & Hausser, M. Synaptic integration gradients in single cortical pyramidal cell dendrites. *Neuron* **69**, 885-892 (2011).

25 Branco, T. & Häusser, M. The single dendritic branch as a fundamental functional unit in the nervous system. *Curr. Opin. Neurobiol.* **20**, 494-502 (2010).

26 Cash, S. & Yuste, R. Linear summation of excitatory inputs by CA1 pyramidal neurons. *Neuron* **22**, 383-394 (1999).

27 Davie, J. T. *et al.* Dendritic patch-clamp recording. *Nat Protoc* **1**, 1235-1247 (2006).

28 Llinas, R. & Nicholson, C. Electrophysiological properties of dendrites and somata in alligator Purkinje cells. *J Neurophysiol* **34**, 532-551 (1971).

29 Svoboda, K., Denk, W., Kleinfeld, D. & Tank, D. W. In vivo dendritic calcium dynamics in neocortical pyramidal neurons. *Nature* **385**, 161-165 (1997).

30 Chen, X. *et al.* Disruption of the olivo-cerebellar circuit by Purkinje neuron-specific ablation of BK channels. *Proc Natl Acad Sci U S A* **107**, 12323-12328 (2010).

31 Jia, H., Rochefort, N. L., Chen, X. & Konnerth, A. In vivo two-photon imaging of sensory-evoked dendritic calcium signals in cortical neurons. *Nat Protoc* **6**, 28-35 (2011).

32 Jia, H., Rochefort, N. L., Chen, X. & Konnerth, A. Dendritic organization of sensory input to cortical neurons in vivo. *Nature* **464**, 1307-1312 (2010).

Publications

Published:

(1) **Chen XW**, Leischner U, Rochefort NL, Nelken I, Konnerth A. (2011) Functional mapping of single spines in cortical neurons in vivo. ***Nature*** 475:501-5.

(2) Jia HB, Rochefort NL, **Chen XW**, Konnerth A. (2011) In vivo two-photon imaging of sensory-evoked dendritic calcium signals in cortical neurons. ***Nat Protoc*** 6:28-35.

(3) **Chen XW**, Kovalchuk Y, Adelsberger H, Henning HA, Sausbier M, Wietzorrek G, Ruth P, Yarom Y, Konnerth A. (2010) Disruption of the olivo-cerebellar circuit by Purkinje neuron-specific ablation of BK channels. ***Proc Natl Acad Sci USA*** 107: 12323-8.

(4) Jia HB, Rochefort NL, **Chen XW**, Konnerth A. (2010) Dendritic organization of sensory input to cortical neurons in vivo. ***Nature*** 464:1307-12.

Submitted:

(1) Busche MA, **Chen X**, Henning HA, Reichwald J, Staufenbiel M, Konnerth A. Acute repair of early defects in hippocampal activity in a mouse model of Alzheimer´s disease.

In preparation:

(1) **Chen XW**, Varga Z, Henning HA, Konnerth A. Basket cell-mediated regulation of sensory-evoked signaling in the cerebellar cortical circuitry in vivo.

(2) **Chen XW**, Leischner U, Konnerth A. In vivo functional imaging of single synapses during cortical Up-states.

(3) **Chen XW**, Adelsberger H, Ruehlmann C, Stroh A, Konnerth A. Essential role for cerebellar rebound potentiation in habituation of the acoustic startle response.

(4) **Chen XW**, Adelsberger H, Ruehlmann C, Stroh A, Hartmann J, Konnerth A. Cerebellar αCaMKII is required for habituation of the acoustic startle response.

(5) **Chen XW**, Hartmann J, Adelsberger H, Konnerth A. Sensory stimulation drives slow excitation and output firing through TRPC3 channels.

Acknowledgements

When I was in the kindergarten, I always answered my teacher that I had a dream in future of being a great scientist like Albert Einstein. At that time, I just simply and blindly adored Einstein since I had no sense of what the science was. After the last ten years study of medicine and biology, particularly after my PhD study in neuroscience occurred here in Munich, where my idol Einstein spent his early life for 14 years, I gained a deeper insight into understanding what the science is, how wonderful and beautiful the science is, and I extremely became fascinated with the question of how the brain works. I just feel like fish freely swimming in the ocean as I am studying in such nice place with an excellent scientific atmosphere. It would be possible to finish my thesis work because of not only my hard work but also, more importantly, an absolutely fantastic team around me. In this special occasion, I would like to express thanks to a number of people, for which gave me help and support through the work.

First of all, I would like to thank my supervisor, Prof. Dr. Arthur Konnerth for everything, including his enthusiasm and inspiration, his scientific guidance with patience for every step during the progress of work. He is always there when I need him. Without such kind mentor, my thesis work would not be possible.

I also thank many other colleagues, Dr. Ulrich Leischner, Prof. Dr. Helmuth Adelsberger, Dr. Yury Kovalchuk, Hongbo Jia, Dr. Nathalie L. Rochefort, Dr. Horst A. Henning, Zsuzsanna Varga, Christine Grienberger for their specific contributions and helps in all the studies.

I am grateful to Prof. Yosef Yarom and Prof. Prof. Israel Nelken (Department of Neurobiology, Hebrew University) for the collaborations for the cerebellum and auditory projects, respectively, and to Dr. Jana Hartmann for suggestions on the cerebellum projects. It has been a great pleasure to work with them and learn from them.

In addition, I wish to thank these people for technical assistance: Dietmar Beyer, Felix Beyer, Werner Zeitz, Andreas Fohr, and Christine Karrer.

Finally, special thanks to my family, and particularly my wife, Jia Lou, who helps me for improving the illustration, and gives me all kinds of encouragement and support. Nothing I can say can express how important I feel about our family in my life.